UNIVERSITY OF CALIFORNIA, SAN DIEGO

# Dilute Nitride GaNP Wide Bandgap Solar Cells Grown by Gas-Source Molecular Beam Epitaxy

A dissertation submitted in partial satisfaction of the
requirements for the degree
Doctor of Philosophy

in

Material Science and Engineering

by

Supanee Sukrittanon

Committee in charge:

Professor Charles W. Tu, Chair
Professor Shadi A. Dayeh, Co-Chair
Professor Prabhakar R. Bandaru
Professor RenKun Chen
Professor Jie Xiang

2015

The dissertation of Supanee Sukrittanon is approved, and it is acceptable in quality and form for publication on microfilm and electronically:

_____

_____

_____

_____
Co-Chair

_____
Chair

University of California, San Diego

2015

DEDICATION

To my family and Allister!

EPIGRAPH

*In order to succeed,*

*we must first believe that we can*

—Nikos Kazantzakis

TABLE OF CONTENTS


Signature Page . . . . . iii

Dedication . . . . . iv

Epigraph . . . . . v

Table of Contents . . . . . vi

List of Figures . . . . . ix

List of Tables . . . . . xiii

Acknowledgements . . . . . xiv

Vita . . . . . xvii

Abstract of the Dissertation . . . . . xix

Chapter 1 Introduction . . . . . 1
1.1 Motivation . . . . . 1
1.2 Background and proposed approach . . . . . 3
1.3 Dilute nitride GaNP . . . . . 5
1.4 Scope of dissertation . . . . . 9

Chapter 2 Design of the Solar Cell . . . . . 12
2.1 Performance characteristics . . . . . 14
2.2 Short circuit current . . . . . 17
2.3 Open circuit voltage . . . . . 20
2.4 Our GaNP solar cell design . . . . . 21
2.4.1 The maximum $J_{sc}$ and $\eta$ under one sun . . . . . 21
2.4.2 The effect of the i-layer width . . . . . 23
2.4.3 The effect of the emitter width . . . . . 23
2.4.4 The effect of recombination velocity at the front surface 28
2.4.5 The effect of carrier lifetime in the i-layer . . . . . 28

Chapter 3 Experiment Procedures . . . . . 30
3.1 Overview . . . . . 30
3.2 Growth . . . . . 30
3.2.1 Gas-source molecular beam epitaxy . . . . . 31
3.2.2 N plasma source . . . . . 32
3.2.3 Reflection high-energy electron diffraction . . . . . 35
3.3 Characterization . . . . . 37

3.3.1 Photoluminescence . . . . . 38
3.3.2 Current-voltage characteristic . . . . . 39
3.3.3 External quantum efficiency . . . . . 39
3.4 Solar cell fabrication . . . . . 41
3.4.1 Rapid thermal annealing . . . . . 41
3.4.2 Mesa etch . . . . . 42
3.4.3 Metallization . . . . . 43

Chapter 4 GaNP Thin Film Solar Cells . . . . . 46
4.1 Overview . . . . . 46
4.2 Device structures . . . . . 47
4.3 Growth . . . . . 49
4.4 Structural characterization . . . . . 50
4.5 Electrical results and discussion . . . . . 52
4.6 Optical results and discussion . . . . . 57
4.7 Comparison to other solar cells . . . . . 58
4.8 Conclusions . . . . . 61
4.9 Acknowledgments . . . . . 62

Chapter 5 GaP/GaNP Microwire Solar Cells . . . . . 63
5.1 Overview . . . . . 63
5.2 Device structure . . . . . 65
5.3 The effect of array period and microwire length . . . . . 67
5.4 The effect of sidewall morphology . . . . . 73
5.5 Effect of anti-reflection coating . . . . . 77
5.6 Conclusions . . . . . 78
5.7 Acknowledgements . . . . . 80

Chapter 6 The Fabrication of GaP/GaNP Core/Shell Microwire . . . . . 81
6.1 Step 1: Fabrication of etch mask . . . . . 82
6.2 Step 2: Top-down dry etch process . . . . . 84
6.3 Step 3: Wet etch . . . . . 89
6.4 Step 4: Shell growth . . . . . 90

Chapter 7 The Growth and Characterization of GaNP/GaNP core/shell Nanowire 94
7.1 Overview . . . . . 94
7.2 GaP nanowires . . . . . 95
7.2.1 Growth . . . . . 95
7.2.2 Structural properties and discussion . . . . . 97
7.3 GaNP nanowires . . . . . 102
7.3.1 Growth . . . . . 102
7.3.2 Structural properties and discussion . . . . . 102
7.4 GaNP/GaNP core/shell nanowires . . . . . 105

7.4.1 Growth . . . . . 105
7.4.2 Structural properties and discussion . . . . . 106
7.4.3 Optical properties and discussion . . . . . 106
7.5 Conclusions . . . . . 109
7.6 Acknowledgments . . . . . 109

Chapter 8 Future work . . . . . 111
8.1 Thin film solar cells . . . . . 111
8.2 Microwire solar cells . . . . . 112

Appendix A MATLAB scripts for a p-i-n GaP/GaNP solar cell . . . . . 114
A.1 The effect of the i-GaNP layer . . . . . 114
A.2 The effect of carrier lifetime in the i-GaNP layer . . . . . 124

Bibliography . . . . . 127

LIST OF FIGURES


Figure 1.1: Best Research solar cell efficiency. . . . . 2
Figure 1.2: Theoretical efficiency contour of top and bottom cells under AM 1.5G. 3
Figure 1.3: (a) Bright-field and (b) dark-field cross-sectional transmission electron microscope (TEM) of GaP on Si substrate. The only defects observed are dislocations due to the lattice mismatch between GaP and Si. . . . . 4
Figure 1.4: Two sub-bands of GaNP as a function of N concentration. The splitting of the conduction band results from the strong interaction of the N localized states and the GaP host extended states. . . . . 6
Figure 1.5: Theoretical bandgap energy calculated from BAC model as a function of N concentration. Inset shows the E-k diagram of both GaP and GaNP. . . . . 7
Figure 1.6: Absorption coefficient of common semiconductors including GaP and GaNP. . . . . 8

Figure 2.1: Equivalent circuit of a solar cell including parasitic resistances. . . 13
Figure 2.2: The effect of (a) series resistance ($R_s$) and (b) shunt resistance ($R_{sh}$) on J-V characteristics of solar cells. . . . . 15
Figure 2.3: J-V and P-V characteristics of a GaNP thin film solar cell. . . . . 16
Figure 2.4: The theoretical and experimental data of bandgap to voltage offset as a function of bandgap. . . . . 17
Figure 2.5: Schematic p-i-n solar cell showing emitter region, i-region, and base region. . . . . 18
Figure 2.6: Calcuated maximum short circuit current density and maximum efficiency as a function of bandgap. . . . . 21
Figure 2.7: Calculated EQE from p-i-n solar cell utilizing (a) GaP, and (b) GaNP as an i-layer, of which thickness is varied. . . . . 24
Figure 2.8: The corresponding short circuit current density as a function of i-layer thickness. . . . . 25
Figure 2.9: EQE and corresponding short circuit current density as the effect of emitter thickness. . . . . 26
Figure 2.10: EQE and corresponding short circuit current density as the effect of recombination velocity at the surface. . . . . 27
Figure 2.11: Open circuit voltage and corresponding efficiency as a function of carrier lifetime. . . . . 28

Figure 3.1: Schematics of the modified Varian Gen-II gas-source molecular beam epitaxy. . . . . 33
Figure 3.2: Schematic of the N plasma source and N species produced by plasma discharge. . . . . 35

Figure 3.3: the experimental dependence of the plasma intensity as a function of the $N_2$ flux at a given applied RF power. . . . . 36
Figure 3.4: Ga and $P_2$ induced RHEED oscillation . . . . . 37
Figure 3.5: Schematic of our PL measurement setup. . . . . 38
Figure 3.6: Schematic of our EQE measurement setup. . . . . 40
Figure 3.7: PL performance after RTA for GaNP samples. . . . . 42
Figure 3.8: Our p-i-n GaNP solar cell under optical microscope. . . . . 43
Figure 3.9: I-V characteristics of Pd/Si contact on n-type GaP. . . . . 44
Figure 3.10: I-V characteristics of Au/Zn/Au contact on p-type GaP. . . . . 45

Figure 4.1: Cross-section schematic of the solar cells presented in this work. Insets are the measured XRD spectra. The XRD spectra of the GaNP samples confirm proper incorporation of N. . . . . 47
Figure 4.2: The band diagram of GaP-800 and GaNP-800. . . . . 48
Figure 4.3: RHEED reconstruction patterns of device layers. . . . . 49
Figure 4.4: (a) XRD spectra showing two $\{115\}$ asymmetric peaks, labled as (115A) and (115B), peformed on GaNP-800. (b) (004) symmetric XRD. . . . . 51
Figure 4.5: TEM images along the [001] zone axis with a g=[020] beam condition of GaP-800, GaNP-800, and GaNP-2000. . . . . 53
Figure 4.6: TEM images of a typical misfit dislocation. . . . . 54
Figure 4.7: J-V characteristics of GaP-800, GaNP-800, and GaNP-2000 under (a) dark condition and (b) AM 1.5G condition with and without AR coating. . . . . 55
Figure 4.8: The calculated reflectance of GaP with/without the double layer AR coating , which consists of $Si_3N_4$ (40 nm) and $SiO_2$ (20 nm), as a function of wavelength. . . . . 56
Figure 4.9: EQE measurements of GaP-800, GaNP-800, and GaNP-2000. . . . 59
Figure 4.10: Comparison of EQE measurements between our best GaNP solar cells and InGaP and GaAsP solar cells, which have similar direct bandgap. . . . . 60

Figure 5.1: (a) Schematic of GaP/GaNP core/shell microwire solar cells in this work (b)-(d) SEM showing top-view of microwires with different array period: 4 $\mu$m, 6 $\mu$m, and 8 $\mu$m, respectively. . . . . 65
Figure 5.2: The fabrication process schematic of GaP/GaNP core/shell microwire solar cell. . . . . 66
Figure 5.3: SEM images showing microwire arrays with length of 6 $\mu$m swept across array periods of (a) 4 $\mu$m, (b) 6 $\mu$m, and (c) 8 $\mu$m. . . . . 67
Figure 5.4: (a) J-V characteristics and (b) EQE of 6-$\mu$m-long microwire solar cells with different period arrays. . . . . 68

Figure 5.5: J-V characteristics and EQE of microwire solar cells with different period arrays for (a),(b) 8-$\mu$m-long microwire solar cells, and (c),(d) 10-$\mu$m-long microwire solar cells. . . . . 71
Figure 5.6: TEM image along the [110] zone axis with a g = [-11-1] beam condition 72
Figure 5.7: SEM showing 6-$\mu$m-long microwires (P = 6 $\mu$m) with (a) rough sidewalls, and (b) smooth sidewalls. . . . . 73
Figure 5.8: J-V characteristics of textured and smooth 6-$\mu$m-long microwires (P = 6 $\mu$m) under dark condition. . . . . 74
Figure 5.9: Comparison of (a) J-V characteristics and (b) EQE of 6-$\mu$m-long microwire (P = 6 $\mu$m) solar cells between the textured and the smooth microwire solar cells. . . . . 75
Figure 5.10: TEM image along the [110] zone axis with a g = [1-11] beam condition showing (a) bright field image of the smooth microwire with L = 6 $\mu$m and P = 6 $\mu$m, and (b) HRTEM image of the shell (red square. 77
Figure 5.11: The calculated reflectance as a function of wavelength of GaP with-/without the AR coating, which consists of $TiO_2$ (33 nm), $Si_3N_4$ (52 nm), and $SiO_2$ (88 nm). . . . . 78
Figure 5.12: (a) J-V characteristics showing the improvement of $J_{sc}$ on the microwire solar cell (L = 6 $\mu$m and P = 6 $\mu$m) after AR coating and (b) their corresponding EQE. . . . . 79

Figure 6.1: The fabrication steps of microwires. . . . . 83
Figure 6.2: The opical microscope images showing (a),(c) the patterned photoresist deployed by photolithography, and (b),(d) the Ni dot array used as an etch mask after lift-off process. . . . . 84
Figure 6.3: Optimization process of RIE with various ratios of $Cl_2$ to $BCl_3$ under a constant pressure and power of 36.5 mtorr and 200 W, respectively. All RIE is performed for 15 minutes. . . . . 85
Figure 6.4: The 45 $^\circ$ SEM images of the etch profile and their morphology of the etched samples under the $Cl_2/BCl_3$ of 0.03 for (a) 15 minutes, (b) 30 minutes, (c) 35 minutes, and (d) 40 minutes. . . . . 87
Figure 6.5: Comparison of the microwires using (a) 200 W and (b) 300 watt for 30 minutes under the identical pressure and the $Cl_2/BCl_3$ of 36.5 mTorr and 0.03, respectively. . . . . 88
Figure 6.6: The 45$^\circ$ SEM images of microwire after wet etch process for (a) 0 min, (c) 15 min, and (e) 25 min. Their corresponding morphology of shell layer are depicted in (b), (d), and (f), respectively. . . . . 91
Figure 6.7: The optical images of our final device illustrating a top contact (blue) and a microwire array (black). . . . . 92

Figure 7.1: Ga droplets as catalysts on Si (111). . . . . 96
Figure 7.2: The schematic showing the VLS growth of Ga(N)P/GaNP core/shell nanowires. . . . . 97

Figure 7.3: SEM images of GaP nanowires on Si (111): (a) GaP-585, (b) GaP-600, and (c) GaP-615. . . . . 98
Figure 7.4: SEM images showing the GaP nanowires grown outside the growth temperature window: (a) GaP-515, and (b) GaP-630. . . . . 100
Figure 7.5: TEM image of GaP-615 showing the twinning planes along [111] nanowire growth direction. . . . . 101
Figure 7.6: SEM images of GaNP nanowires on Si (111): (a) GaNP-585, (b) GaNP-600, and (c) GaNP-615. . . . . 103
Figure 7.7: TEM images of GaNP nanowires (GaNP-615). . . . . 105
Figure 7.8: SEM images showing (a) GaNP-615 (the cores of S-GaNP/GaNP) and (b) S-GaNP/GaNP. . . . . 106
Figure 7.9: PL emission from arrays of GaNP-615 and S-GaNP/GaNP performed at 300 K. . . . . 107
Figure 7.10: PL emissions from an ensemble (blue) and a single (red) S-GaP/GaNP. 108

LIST OF TABLES

Table 2.1: The parameters used in our calculations . . . . . 22

Table 4.1: Performance parameters of GaP-800, GaNP-800, and GaNP-2000 with and without AR coating.) . . . . . 56

Table 5.1: The solar cell parameters from microwire solar cells with different lengths and array periods . . . . . 69

Table 5.2: The solar cell parameters from microwire solar cells (L = 6 $\mu$m and P = 6 $\mu$m) with different sidewall morphology, after AR coating and also the parameters from the thin film solar cell in the same growth run 76

Table 7.1: The average diameters and lengths of nanowires grown at different temperatures . . . . . 99

Table 7.2: The average diameters and lengths of GaNP nanowires grown at different temperatures . . . . . 104

ACKNOWLEDGEMENTS

Foremost, I would like to express my sincere gratitude to my advisor Prof. Charles W. Tu for the continuous support of my Ph. D. study, his valuable guidance, and his patience. I deeply appreciate the freedom he provided me to explore and learn to solve problems on my own. At the same time, his guidance and experience have always helped me to overcome the many difficult problems I faced throughout my Ph. D. study. I also would like to thank Prof. Shadi A. Dayeh for serving as my co-advisor in the last year of my Ph. D. I am deeply grateful to him for his abundant advice and fruitful discussion that greatly aided in developing my ideas and improving my research. The motivation and encouragement he steadfastly provided are really appreciated. I am undoubtedly fortunate to have had these two advisors. Although the Ph.D. program is very challenging, my advisors made it interesting and exciting.

In addition to my advisors, I greatly appreciate the kind support of the members of my thesis committee: Prof. Prabhakar Bandaru, Prof. Renkun Chen, and Prof. Jie Xiang. I am grateful for their valuable input and suggestions on the completion of this thesis.

My sincere thanks also goes to Dr. Janet Pan for her abundant advice about both molecular beam epitaxy (MBE) thin film growth and fabrication processes. The experience and enthusiasm she shared are priceless. I also would like to thank Prof. Deli Wang, a member of my Ph.D qualifying exam committee, for his valuable advice on nanowires. I also appreciate Prof. S. S. Lau for his input, especially his suggestions regarding metal contacts.

I would like to thank my fellow colleagues at UCSD. I am heavily indebted to Dr. Hua Li and Dr. Yanjin Kuang for having trained and taught me all about MBE and troubleshooting skills. In particular, I would like to express my thanks to Dr. Yanjin Kuang for his insightful suggestions, mentoring, and for his great company in the lab

over the past 4 years. I would like to thank Jimmy Chuang and Michael C. Breeden for assisting with my nano/microwire solar cell optimization and fabrication processes. I also greatly appreciate the help provided by Casey Sanchez and Rui La in taking care of lab safety and MBE maintenance. They are great labmates and also great friends. My thanks also goes to Ren Liu, Yun Goo Ro, and Ben Holladay for the help with transmission electron microscopy (TEM), solar cell fabrication techniques, and X-ray diffraction measurements (XRD), respectively. Many thanks to other colleagues with whom I have collaborated and assisted throughout my time at UCSD: Renjie Chen, Siarhei Vishniakou, Atsunori Tanaka, Alireza Kargar, Ahmed Youssef and other lab members.

A big thanks to the staff at Nano3: Bernd Fruhberger, Larry Grissom, Sean Parks, Ivan Harris, Xuekun Lu, and Ryan Anderson. They were always there to provide technical support in the clean room whenever needed.

Last, I would like to thank the people I love the most in the world: my family and my husband, Allister. Many thanks to my family for their love, care, and support across the ocean. Without them, this dissertation could not have been possible. A very big thanks to my loving husband for always being there for me throughout the ups and downs of my Ph. D. I really appreciate the support, encouragement, motivation, patience, understanding, and everything else that he has always provided. In addition, I would like to thank him very much for the time he spent editing this dissertation as well as his fresh perspective and in-depth discussion.

Chapter 4 of this dissertation was partially published in **S. Sukrittanon***, R. Liu*, Y. G. Ro, J. L. Pan, K. L. Jungjohann, C. W. Tu, S. A. Dayeh, "Enhanced conversion efficiency in wide-bandgap GaNP solar cells", *Appl. Phys. Lett.*, 100, 053108 (2015). *Equal contribution. The work was supported by the National Science Foundation under grant no. DMR-1106369. TEM work was performed at the Center for Integrated Nanotechnologies (CINT), U.S. Department of Energy, Office of Basic Energy Sciences

User Facility at Los Alamos National Laboratory (contract DE-AC52-06NA25396) and Sandia National Laboratories (contract DE-AC04-94AL85000).

Chapter 5 of this dissertation was partially used in a yet to be published work. The work was supported by the National Science Foundation under grant no. DMR-1106369, no. DMR-1503595, and no. ECCS-1351980. TEM work was performed at the Center for CINT, U.S. Department of Energy, Office of Basic Energy Sciences User Facility at Los Alamos National Laboratory (contract DE-AC52-06NA25396) and Sandia National Laboratories (contract DE-AC04-94AL85000).

Chapter 7 of this dissertation was partially published in **S. Sukrittanon**, Y. J. Kuang, C. W. Tu, "Growth and characterization of GaP/GaNP core/shell nanowires", *J. Vac. Sci, Technol. B*, 31, 03C110 (2013) and **S. Sukrittanon**, Y. J. Kuang, A. Dobrovolsky, W. M. Kang, J. S. Jang, B. J. Kim, W. M. Chen, I. A. Buyanova, C. W. Tu, "Growth and characterization of dilute nitride $GaN_xP_{1-x}$ nanowires and $GaN_xP_{1-x}$/$GaN_yP_{1-y}$ core/shell nanowires on Si (111) by gas source molecular beam epitaxy", *Appl. Phys. Lett.*, 105, 072107 (2014). Financial support for the work was provided by the National Science Foundation under grant nos. DMR-0907652, DMR-1106369 and the Royal Government of Thailand Scholarship (DPST). The photoluminescence experiments were supported by the Swedish Research Council (grant no. 621-2010-3815). TEM experiments were supported by the National Science Foundation of Korea (NRF) and the Korea government (2013R1A1A1007978), and the Ministry of Trade, Industry and Energy (MTIE) through the industrial infrastructure program under grant no. 10033630.

## VITA

| | |
|---|---|
| 2009 | B. S. in Physics *cum laude*, Chulalongkorn University |
| 2011 | M. S. in Material Science and Engineering, University of California, San Diego |
| 2015 | Ph. D. in Material Science and Engineering, University of California, San Diego |

## PUBLICATIONS

**S. Sukrittanon**, R. Liu, M. C. Breeden, J. L. Pan, K. L. Jungjohann, C. W. Tu, S. A. Dayeh, "Radial direct bandgap p-i-n GaNP microwire solar cells with enhanced short circuit current", in preparation.

**S. Sukrittanon***, R. Liu*, Y. G. Ro, J. L. Pan, K. L. Jungjohann, C. W. Tu, S. A. Dayeh, "Enhanced conversion efficiency in wide-bandgap GaNP solar cells", *Appl. Phys. Lett.*, 100, 053108 (2015). *Equal contribution.

**S. Sukrittanon**, Y. J. Kuang, A. Dobrovolsky, W. M. Kang, J. S. Jang, B. J. Kim, W. M. Chen, I. A. Buyanova, C. W. Tu, "Growth and characterization of dilute nitride $GaN_xP_{1-x}$ nanowires and $GaN_xP_{1-x}$/$GaN_yP_{1-y}$ core/shell nanowires on Si (111) by gas source molecular beam epitaxy", *Appl. Phys. Lett.*, 105, 072107 (2014).

**S. Sukrittanon**, Y. J. Kuang, C. W. Tu, "Growth and characterization of GaP/GaNP core/shell nanowires", *J. Vac. Sci, Technol. B*, 31, 03C110 (2013).

S. Filippov, **S. Sukrittanon**, Y. J. Kuang, C. W. Tu, P. O. Å. Persson, W. M. Chen, I. A. Buyanova, "Origin of strong photoluminescence polarization in GaNP nanowires", *Nano Lett.*, 14, 5264 (2014).

A. Dobrovolsky, **S. Sukrittanon**, Y. J. Kuang, C. W. Tu, W. M. Chen, I. A. Buyanova, "Energy upconversion in GaP/GaNP core/shell nanowires for enhanced near-infrared light harvesting", *Small*, 10, 4430 (2014).

A. Dobrovolsky, **S. Sukrittanon**, Y. J. Kuang, C. W. Tu, W. M. Chen, I. A. Buyanova, "Raman spectroscopy of GaP/GaNP core/shell nanowires", *Appl. Phys. Lett.*, 105, 193102 (2014).

Y. J. Kuang, **S. Sukrittanon**, H. Li, C. W. Tu, "Growth and photoluminescence of self-catalyzed GaP/GaNP core/shell nanowires on Si(111) by gas source molecular beam epitaxy", *Appl. Phys. Lett.*, 100, 053108 (2012).

J. E. Stehr, A. Dobrovolsky, **S. Sukrittanon**, Y. J. Kuang, C. W. Tu, W. M. Chen, I. A. Buyanova, "Optimizing GaNP Coaxial Nanowires for Efficient Light Emission by controlling formation of surface and Interfacial defects", *Nano Lett.*, 15, 242 (2015).

A. Dobrovolsky, P. O. *Å*. Persson, **S. Sukrittanon**, Y. J. Kuang, C. W. Tu, W. M. Chen, I. A. Buyanova, "Effects of polytypism on optical properties and band structure of individual Ga(N)P nanowires from correlative spatially resolved structural and optical studies", *Nano Lett.*, 15, 4052 (2015).

Y. J. Kuang, K. Sun, **S. Sukrittanon**, K. Takabayashi, I. Kamiya, N. S. Lewis, C. W. Tu, "Enhancement of the performance of GaP solar cells by embedded In(N)P quantum dots", *Nano Energy*, 15, 782 (2015).

A. Dobrovolsky, J. E. Stehr, **S. Sukrittanon**, Y. J. Kuang, C. W. Tu, W. M. Chen, I. A. Buyanova, "FabryPerot microcavity modes in single GaP/GaNP core/shell nanowires", *Small*, (2015).

Y. J. Kuang, K. Takabayashi, **S. Sukrittanon**, J. L. Pan, I. Kamiya, C. W. Tu, "Dilute nitride InNP quantum dots: growth and photoluminescence mechanism", *Appl. Phys. Lett.*, 105, 173112 (2014).

A. Dobrovolsky, S. Chen, Y. J. Kuang, **S. Sukrittanon**, C. W. Tu, W. M. Chen, I. A. Buyanova, "Optical properties of GaP/GaNP core/shell nanowires: a temperature-dependent study", *Nanoscale Res. Lett.*, 8, 239 (2013).

A. Dobrovolsky, J. E. Stehr, S. L. Chen, Y. J. Kuang, **S. Sukrittanon**, C. W. Tu, W. M. Chen, I. A. Buyanova, "Mechanism for radiative recombination and defect properties of GaP/GaNP core/shell nanowires", *Appl. Phys. Lett.*, 101, 163106 (2012).

ABSTRACT OF THE DISSERTATION

**Dilute Nitride GaNP Wide Bandgap Solar Cells Grown by Gas-Source Molecular Beam Epitaxy**

by

Supanee Sukrittanon

Doctor of Philosophy in Material Science and Engineering

University of California, San Diego, 2015

Professor Charles W. Tu, Chair
Professor Shadi A. Dayeh, Co-Chair

Integration of III-V semiconductors and Si is a very attractive means to achieve low-cost high-efficiency solar cells. A promising configuration is to utilize a dual-junction solar cell, in which Si is employed as the bottom junction and a wide-bandgap III-V semiconductor as the top junction. The use of a III-V semiconductor as a top junction offers the potential to achieve higher efficiencies than today's best Si solar cell. Dilute nitride GaNP is a promising candidate for the top cell in dual-junction solar cells because it possesses several extremely important attributes: a direct-bandgap that is also tunable

as well as easily-attained lattice-match with Si. As a first step towards integration of GaNP solar cells onto Si, the goal of this dissertation is to optimize and demonstrate GaNP solar cells grown by gas-source molecular beam epitaxy (GSMBE) on GaP (001) substrate.

The dissertation is divided into three major parts. In the first part, we demonstrate $\sim$2.05 eV ([N]$\sim$1.8%) dilute nitride GaNP thin film solar cells, in which the GaNP is closely lattice-matched to Si, on GaP substrates. From transmission electron microscopy (TEM), the device exhibits defects only at the GaNP/GaP interface, and no threading dislocations in the active layer are observed. Our best GaNP solar cell achieved an efficiency of 7.9% with anti-reflection (AR) coating and no window layer. This GaNP solar cell's efficiency is higher than the most efficient GaP solar cell to date and higher than other solar cells with similar direct bandgap (InGaP, GaAsP). Through a systematic study of the structural, electrical, and optical properties of the device, efficient broadband optical absorption and enhanced solar cell performance using GaNP are demonstrated.

In the second part, we demonstrate the successful fabrication of GaP/GaNP core/shell microwires utilizing a novel technique: top-down reactive-ion etching (RIE) to create the cores and MBE to create the shells. Systematic studies have been performed over a series of microwire lengths, array periods, and microwire sidewall morphology. For a fixed length, short circuit current ($J_{sc}$) increases as physical fill factor (PFF) of microwires increases, while, for a fixed array period, $J_{sc}$ increases as microwire length increases. Our studies show that the open circuit voltage ($V_{oc}$) is degraded primarily due to defects at the GaP/GaNP interface and in the shells, not surface recombination. The best efficiency we achieved using our microwire solar cell is 3.2% using an AR coating. Compared to thin film solar cells in the same growth run, the microwire solar cells exhibit greater $J_{sc}$ but poorer $V_{oc}$. This results from greater light absorption and a greater number of defects in the microwire structure, respectively.

In the final part, vertical self-catalyzed GaP, GaNP, and GaNP/GaNP core/shell nanowires are demonstrated. The growth window of GaP nanowires is comparable to the growth window of GaNP nanowires. The diameter of nanowires (cores) can be controlled by adjusting substrate temperature ($T_{sub}$). The shells can be grown by decreasing $T_{sub}$ and increasing the V/III incorporation ratio to reduce adatom mobility. The crystal structures of GaP and GaNP nanowires are mixtures of cubic zincblend phase and hexagonal wurtzite phase along the [111] growth direction. According to photoluminescence measurements, the broad spectrum of nanowire arrays do not result from the variation of N composition among nanowires, but from the mechanism of light emission of GaNP.

# Chapter 1

# Introduction

## 1.1 Motivation

Si-based solar cell technology dominates the global market with over 90% market share according to a report in 2015.[2] The primary driver behind the success of Si-based solar cells is their combination of satisfactory efficiency and low cost. With solar cells becoming more mainstream, the need for smaller (i.e., more efficient) and lighter (i.e., made from less material) devices is increasing. Unfortunately, the efficiency of Si-based solar cells has remained for the past 15 years around 25% under 1 sun, close to but under the theoretical limit of 30%. Figure 1.1 shows that, between 1999 and 2015, the efficiency of Si-based solar cells has only increased 0.6%.[3,4] On the contrary, III-V solar cell technology has seen continuous advancements over an initially sluggish performance and currently provides a world record efficiency of 38.8% under 1 sun (46% under concentrated light).[3] III-V compound multi-junction solar cells have been the most successful technology to achieve the highest solar efficiency, which is beyond the single cell Shockley-Queisser limit, among all types of solar cells. Despite their higher efficiency, wide adoption of III-V solar cells is impeded by the material cost, especially

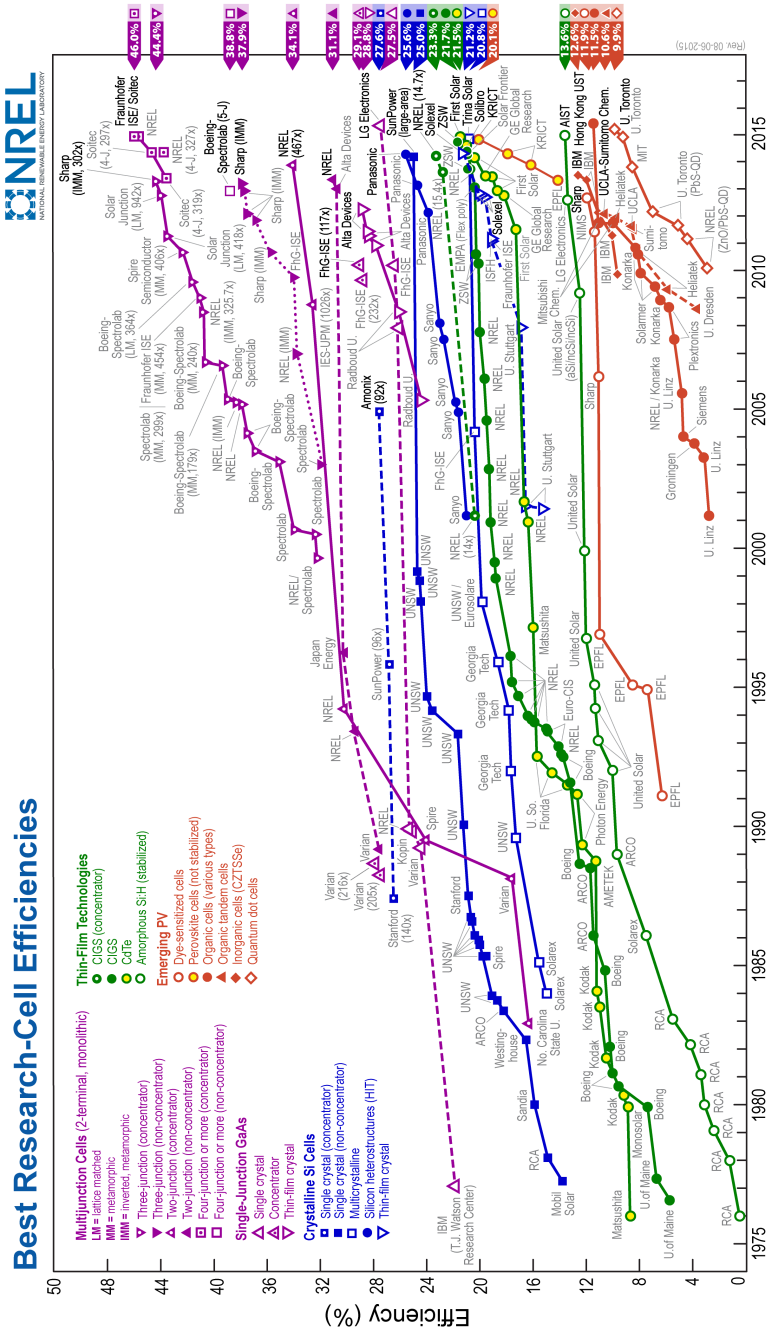


**Figure 1.1**: Best Research solar cell efficiency.[1]

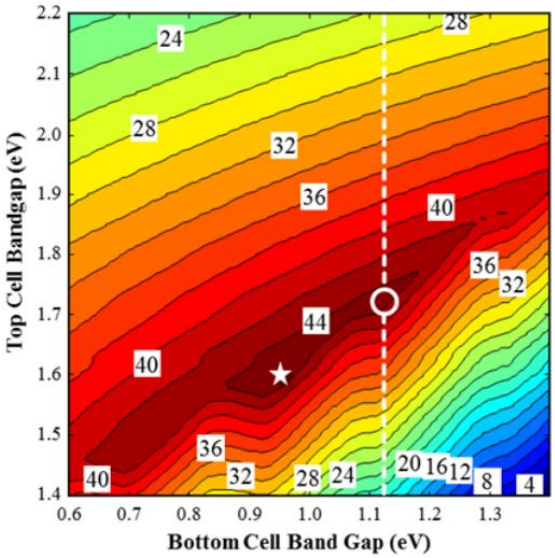


**Figure 1.2**: Theoretical efficiency contour of top and bottom cells under AM 1.5G. The dashed line indicates the fixed 1.12 eV Si bottom cell.[5]

the cost of the substrate. Thus, integration of high-efficiency III-V semiconductors directly onto Si substrate is a very attractive approach to create low-cost, highly efficiency solar cells.

In III-V/Si solar cells, Si can be used as a substrate or can also be used as an excellent active bottom cells. In theory, a dual-junction solar cell that employs 1.12 eV Si as the active bottom-junction could achieve a maximum solar efficiency of 45%[5] under one sun by employing III-V's bandgap of 1.74 eV.,[6,7] as depicted in Figure1.2.

## 1.2 Background and proposed approach

Integration of III-V semiconductors on Si substrate for solar cells began in the 1980s using a monolithic (heteroepitaxial) growth approach. This approach proved to be very challenging as it is susceptible to many forms of mismatch between the two materials: lattice mismatch, thermal expansion mismatch, and polar/non-polar mismatch. In 1986, GaAs was initially integrated directly on Si substrate as a first step towards integration of

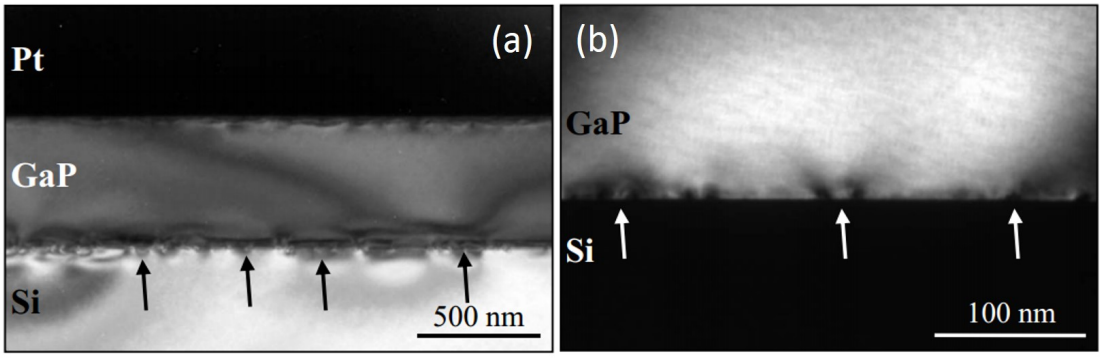


**Figure 1.3**: (a) Bright-field and (b) dark-field cross-sectional transmission electron microscope (TEM) of GaP on Si substrate. The only defects observed are dislocations due to the lattice mismatch between GaP and Si.[18]

lattice-matched InGaP/GaAs dual-junction solar cell on Si substrate.[8] Unfortunately, the aforementioned challenges of monolithic growth, especially the lattice mismatch of 4% between GaAs and Si, resulted in a significant number of misfit dislocations leading to an efficiency of only 7%. In response, researchers have investigated numerous methods to mitigate defects which include (1) using thermal cycle growth with a very thick buffer (e.g., a 7-$\mu$m-thick GaAs buffer) to reduce dislocation density,[9] (2) introducing superlattices to prevent threading dislocations from spreading to the active layers,[10,11] and (3) utilizing a metamorphic buffer layer (e.g., SiGe and GaAsP) to confine the mismatch strain between the III-V top cell and the Si substrate across the thickness of the metamorphic buffer.[12–17]

In recent years, it has been demonstrated that GaP can be successfully grown directly on Si substrates using both molecular beam epitaxy (MBE) and metalorganic chemical vapor deposition (MOCVD).[18,19] GaP is a particularly interesting III-V semiconductor because it exhibits the smallest lattice mismatch to Si (0.37% at 300K) of all binary III-V materials. The successful growth of GaP on Si was accomplished using several steps: (1) double-step formation utilizing an offcut (4°-6° toward <110>) Si substrate combined with proper annealing treatment, (2) Si surface cleaning, (3) Ga-first

migration enhanced epitaxy (MEE) for GaP nucleation, and (4) a multi-temperature MBE GaP growth process. Using these steps, GaP can be grown on Si without any nucleation-related defects such as antiphase domains, stacking faults, and microtwins.[18,19] The only remaining defects are misfit dislocations, which result from lattice mismatch between GaP and Si, as seen in Figure 1.3.

The ability to grow low-defect GaP on Si makes GaP a very promising candidate for the top junction of a dual-junction solar cell. Unfortunately, GaP suffers from an indirect-bandgap and, consequently, a low absorption coefficient. This disadvantage limits the efficiency of GaP to only a few percent, even in optimized designs.[20–22] Moreover, GaP possesses a fixed bandgap of 2.26 eV, which is much larger than the optimal bandgap for the top junction. For these reasons, GaP/Si is instead commonly employed as a high-quality virtual substrate for other III-V top cells. For example, a GaP/Si is commonly employed as a virtual substrate for 1.7 eV GaAsP solar cells.[13] In this particular case, a metamorphic buffer layer is sandwiched between the top cell and the underlying virtual substrate to compensate for the high lattice mismatch between the two. Unfortunately, while the buffer layer enables use of the virtual substrate, it also increases device complexity and introduces crystal defects that naturally occur throughout the buffer as it gradually transitions from one lattice constant to another. In this work, we propose an alternative approach by using GaNP.

## 1.3 Dilute nitride GaNP

Dilute nitride GaNP alloys are a unique semiconductor material in which small amounts of N atoms substitute P (group V) elements in a conventional GaP host semiconductor. Incorporating a small amount of N into GaP splits the conduction band of GaP into two sub-bands, $E_+$ and $E_-$, as seen in Figure 1.4. The $E_-$ acts as the fundamental

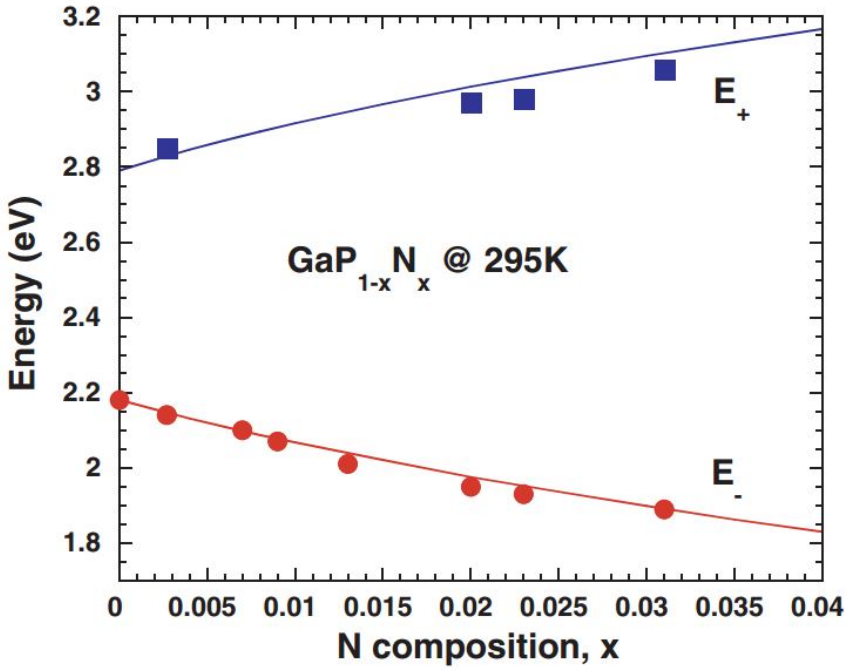


**Figure 1.4**: Two sub-bands, $E_+$ and $E_-$, of GaNP as a function of N concentration. The splitting of the conduction band results from the strong interaction of the N localized states and the GaP host extended states.[25]

bandgap of GaNP. This unusual property of dilute nitride alloys is effectively predicted using the band anti-crossing (BAC) model.[23,24] This model describes the interaction of the two energy levels, which are the extended states of the semiconductor matrix and the N localized states, using a perturbation Hamiltonian.

$$\begin{vmatrix} E - E^M & V_{MN}\sqrt{x} \\ V_{MN}\sqrt{x} & E - E^N \end{vmatrix} = 0 \tag{1.1}$$

where $E^M$ is the dispersion relation for the matrix conduction band, $E^N$ is the N state energy which is located at 2.15 eV above the valence band maximum of GaP,[25] $V_{MN}$ is the interaction coefficient of the matrix conduction band and the N state energy (for GaNP, $V_{MN}$ = 3.05 eV at Γ-band and $V_{MN}$ = 0.90 eV at the X-band ),[25] and $x$ is the N concentration. The eigen values of this equation describe the E-k dispersion relation of

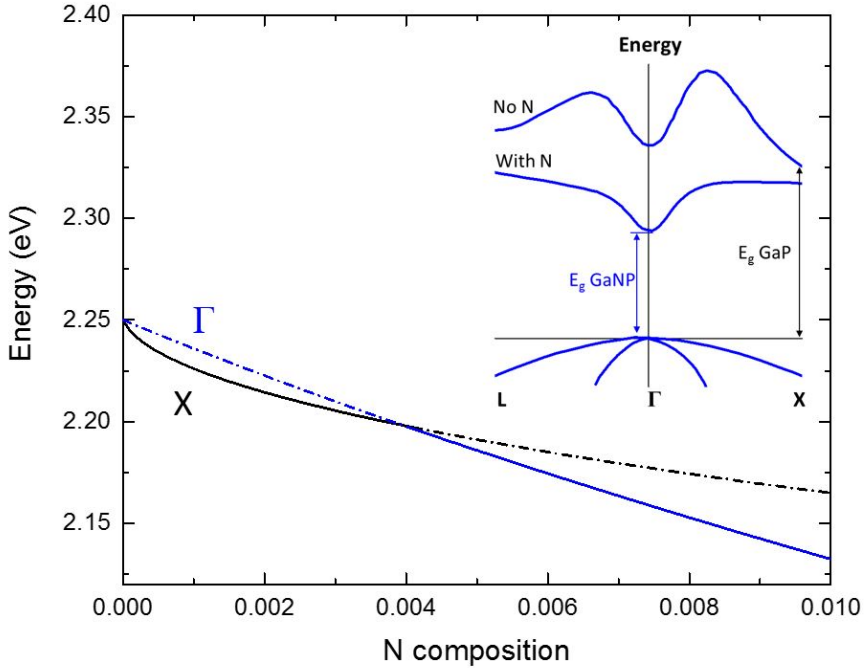


**Figure 1.5**: Theoretical bandgap energy calculated from BAC model as a function of N concentration. Inset shows the E-k diagram of both GaP and GaNP.

the dilute nitride alloy.

$$E_{\pm}(k) = \frac{1}{2}\left\{E^N + E^M(k) \pm \sqrt{(E^N - E^M(k))^2 + 4V_{MN}^2 x}\right\} \tag{1.2}$$

Dilute nitride GaNP is a promising candidate for the top cell in dual-junction solar cells for several outstanding reasons. First, by introducing sufficient N concentration into GaP, the resulting GaNP exhibits a direct-bandgap.[26,27] Figure 1.5 shows the theoretical bandgap energy we calculated using the BAC model (i.e., Equation 1.2 using the parameter values which were previously mentioned for GaNP) as a function of N concentration and the inset of Figure 1.5 shows the E-k diagrams of both GaP and GaNP to illustrate the N effect. As N concentration increases, the energy of the Γ-band decreases faster than the energy of the X-band. This results from the greater interaction coefficient between the matrix conduction band and the N state energy at the X-band, compared

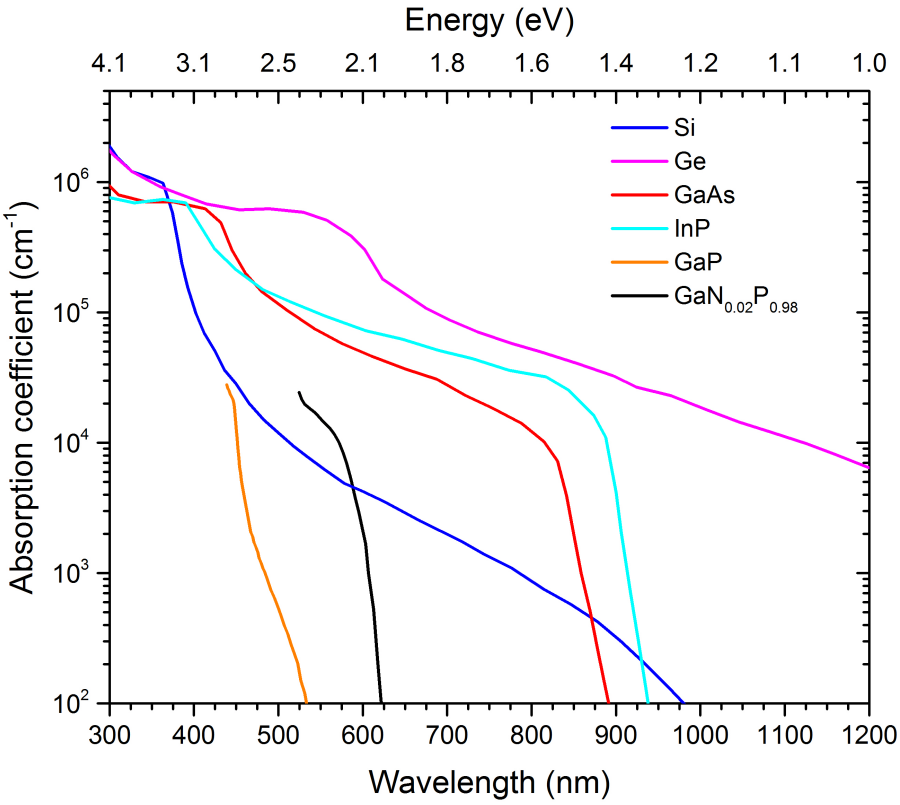


**Figure 1.6**: Absorption coefficient of common semiconductors including GaP and GaNP.

to the Γ-band. At N concentration of only $\sim 0.4\%$, the energy of the Γ-band is lower than the energy at the X-band. Thus, GaNP becomes a direct-bandgap semiconductor at a N concentration of $\sim 0.4\%$. Figure 1.6 shows the absorption coefficient of common semiconductors including indirect-bandgap GaP and direct-bandgap GaNP. A direct bandgap semiconductor, like GaNP or GaAs, exhibits an absorption coefficient of about $10^4$ cm$^{-1}$ above the band edge. This is in contrast to indirect-bandgap GaP, which exhibits an absorption coefficient between $10^2$ and $10^3$ cm$^{-1}$ above the band edge.[28–30]

Second, incorporating N decreases the lattice constant of GaP. At N concentration of $\sim$2%, GaNP becomes lattice-matched with Si. This facilitates the growth of GaNP directly on Si without the need for a metamorphic buffer layer or GaP/Si virtual substrate.

Consequently, the device complexity as well as any crystal defects associated with lattice-mismatched growth can be reduced.

Third, incorporating a small amount of N into GaP drastically decreases the bandgap of GaP due to the strong interaction of the N localized states and the GaP host extended states, which causes the conduction band to split into two sub-bands, $E_+$ and $E_-$, as depicted in Figure 1.4. This allows the bandgap of GaNP to be tuned to the optimal top-junction bandgap of 1.7 eV by incorporating only $\sim$4.5% of N, resulting in only $\sim$0.41% lattice mismatch with Si. Given all its advantages, GaNP is an ideal III-V candidate for the top cell on Si substrates for low-cost solar cell applications.

## 1.4 Scope of dissertation

Given its solar-friendly properties and ease with which it can be grown on Si, GaNP is a promising yet little-studied material for solar cell applications. As a first step towards integration of GaNP solar cells onto Si, the goal of this dissertation is to optimize and demonstrate $\sim$2.05 eV ([N]$\sim$1.8%) GaNP solar cells on a GaP (001) substrate. GaP is chosen as the substrate because it has the closest lattice constant to Si among all III-V substrates. Using GaP as a substrate also rules out the negative effects resulting from defects associated with growth directly on Si. In this dissertation, two configurations of solar cells are explored: (1) thin film GaNP in Chapter 4, and (2) core/shell microwire GaNP in Chapters 5 and 6. We also discuss the growth and characterization of smaller scale GaNP nanowires on Si (111) as another potential solar cell structure in Chapter 7. For all growths, gas-source MBE (GSMBE) is employed.

Chapter 2 describes the basics of solar cells and key solar cell performance parameters. Simulations are performed to show the effect of short circuit current density ($J_{sc}$) and external quantum efficiency (EQE) under various conditions: intrinsic layer

width, emitter width, recombination velocity, and carrier lifetime in the intrinsic layer.

Chapter 3 describes our GSMBE modified to handle gas sources ($PH_3$ and $AsH_3$) and a N plasma source. In addition, several techniques used for material characterization including photoluminescence (PL), current density-voltage (J-V), and EQE measurements are described. Finally, the fabrication and optimization techniques (i.e., rapid thermal annealing (RTA), mesa etch, metallization) are discussed.

Chapter 4 is devoted to the optimization and demonstration of $\sim$2.05 eV ([N]$\sim$ 1.8%) GaNP thin film solar cells on GaP (001) substrate. A high-resolution Discover D8 X-ray diffraction (XRD) system with a Bruker rotating anode diffractometer and a FEI Tecnai F30 300kV transmission electron microscope (TEM) are employed for determining N concentration and structural characterization, respectively. Solar cell performance is determined by using J-V and EQE measurements. Finally, we compare our solar cell performance with the most efficient GaP solar cell to date as well as direct-bandgap InGaP and GaAsP solar cells.

Chapter 5 demonstrates GaP/GaNP core/shell microwire solar cells on GaP (001) substrate. All microwire samples are p-i-n solar cells, for which the fabrication processes are described. Systematic studies have been performed over a series of microwire lengths (L = 6 $\mu$m, 8 $\mu$m, 10 $\mu$m), array periods (P = 4 $\mu$m, 6 $\mu$m, 8 $\mu$m), and microwire sidewall morphology. The structural properties of the microwires are characterized using scanning electron microscopy (SEM) and TEM, and solar cell performance is determined using J-V and EQE measurements.

Chapter 6 describes the fabrication optimization of GaP/GaNP core/shell microwires including the process to create metal array patterns, the reactive ion etching (RIE) process to create vertical microwires, and the wet etch technique to smooth the rough sidewalls and the MBE shell layer.

Chapter 7 is devoted to the study of self-catalyzed GaP, GaNP, and GaNP/GaNP

nanowires grown on Si (111) substrate. Growth windows, structural properties, and optical properties are reported. The structural properties are characterized using SEM and TEM. The optical properties are characterized using PL measurements on both the nanowire array and a single nanowire.

Chapter 8 discusses possible future work.

# Chapter 2

# Design of the Solar Cell

This Chapter describes the physical principles of solar cell operation and its key performance metrics. Simulations are performed to show the effect of short circuit current ($J_{sc}$) and external quantum efficiency (EQE) under varying conditions: intrinsic layer (i-layer) width, emitter width, recombination velocity, and carrier lifetime in the i-layer.

A solar cell is an electronic device that converts photonic energy (i.e., light) into electricity. Photons, which have greater energy than the bandgap of the solar cell, are absorbed by the solar cell and generate electron-hole pairs. The electron-hole pairs are subsequently separated by a built-in electric field and extracted to an external circuit. To simplify the analysis, a solar cell is modeled as a current source in parallel with a diode as is illustrated in Figure 2.1.

When exposed to light, a solar cell produces photo-current (i.e., short circuit current ($I_{sc}$)) that is proportional to the light intensity. This current develops a voltage across the terminals of the cell that is inversely proportional to load resistance. This voltage, in turn, forward biases the diode and generates a parasitic current in the opposite direction to the photo-current that degrades the net current at the load. This reverse current is called dark current ($I_{dark}$), and it is named as such because it is the current that

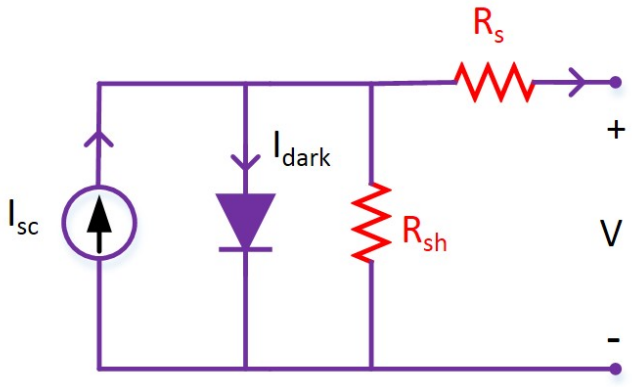


**Figure 2.1**: Equivalent circuit of a solar cell including parasitic resistances.

flows through the device when an external voltage is applied across the terminals of the solar cell in the dark. The dark current is basically the diffusion current in a forward biases cell, and is the saturation current of the diode in a reverse biases.

In a real solar cell, two parasitic resistances, which are series resistance ($R_s$) and parallel (shunt) resistance ($R_{sh}$), are also included in the solar cell model. These resistances cause the power losses in a solar cell. High $R_s$ primarily results from the resistance in the cell material and from the contacts. Low $R_{sh}$, on the other hand, primarily results from current leakage of the solar cell due to manufacturing defects (e.g., cracks, scratches) and local recombination sites (e.g., defects, dislocations, grain boundaries).[31] Accounting for non-idealities, the net current density at the terminals of the cell in the cell is given by:

$$J = J_{sc} - J_o(e^{q(V+JAR_s)/nk_BT} - 1) - \frac{V + JAR_s}{R_{sh}} \tag{2.1}$$

where $q$ is electric charge, $J_o$ is saturation dark current density, $n$ is an ideality factor that accounts for recombination effects, $k_B$ is Boltzmann's constant, T is temperature in K, and A is device area. The effect of the resistances on current density-voltage (J-V) characteristics of solar cells are shown in Figure 2.2. For an efficient solar cell, $R_s$ should

be minimized,while $R_{sh}$ should be maximized.

## 2.1 Performance characteristics

The standard test condition (STC) for a solar cell is air mass 1.5 global (AM 1.5G) spectrum, which defines the power of the incident light as 100 mW/cm$^2$ at sea level due to direct and diffuse incidence. Figure 2.3, as an example, illustrates the experimentally measured current density-voltage and the power-voltage characteristics of our GaNP solar cell under AM 1.5G and highlights the key parameters of a solar cell: (1) short circuit current density ($J_{sc}$), which is the current density when the voltage across the cell is zero, (2) open circuit voltage ($V_{oc}$), which is the maximum voltage of the operation region of the cell, and can be determined as the voltage when the terminals of the cell are isolated, and (3) the current density ($J_m$) and voltage ($V_m$) that result in the solar cell's maximum power density and are closely tied to its fill factor (FF) and solar cell efficiency ($\eta$).

Fill factor (FF) is a measure of how closely a solar cell approaches its ideal performance (i.e., $R_s = R_{sh} = 0$) and is defined as the ratio of the maximum power density to the product of $J_{sc}$ and $V_{oc}$.

$$FF = \frac{J_m V_m}{J_{sc} V_{oc}} \tag{2.2}$$

For an ideal case, FF can be approximated within four decimal places as:[32,33]

$$FF = \frac{\frac{qV_{oc}}{nK_BT} - ln(\frac{qV_{oc}}{nK_BT} + 0.72)}{\frac{qV_{oc}}{nK_BT} + 1} \tag{2.3}$$

The efficiency of a solar cell ($\eta$), is defined as the ratio of its input energy (i.e., incoming light) to its output energy (electrical output at the terminals), and it is often

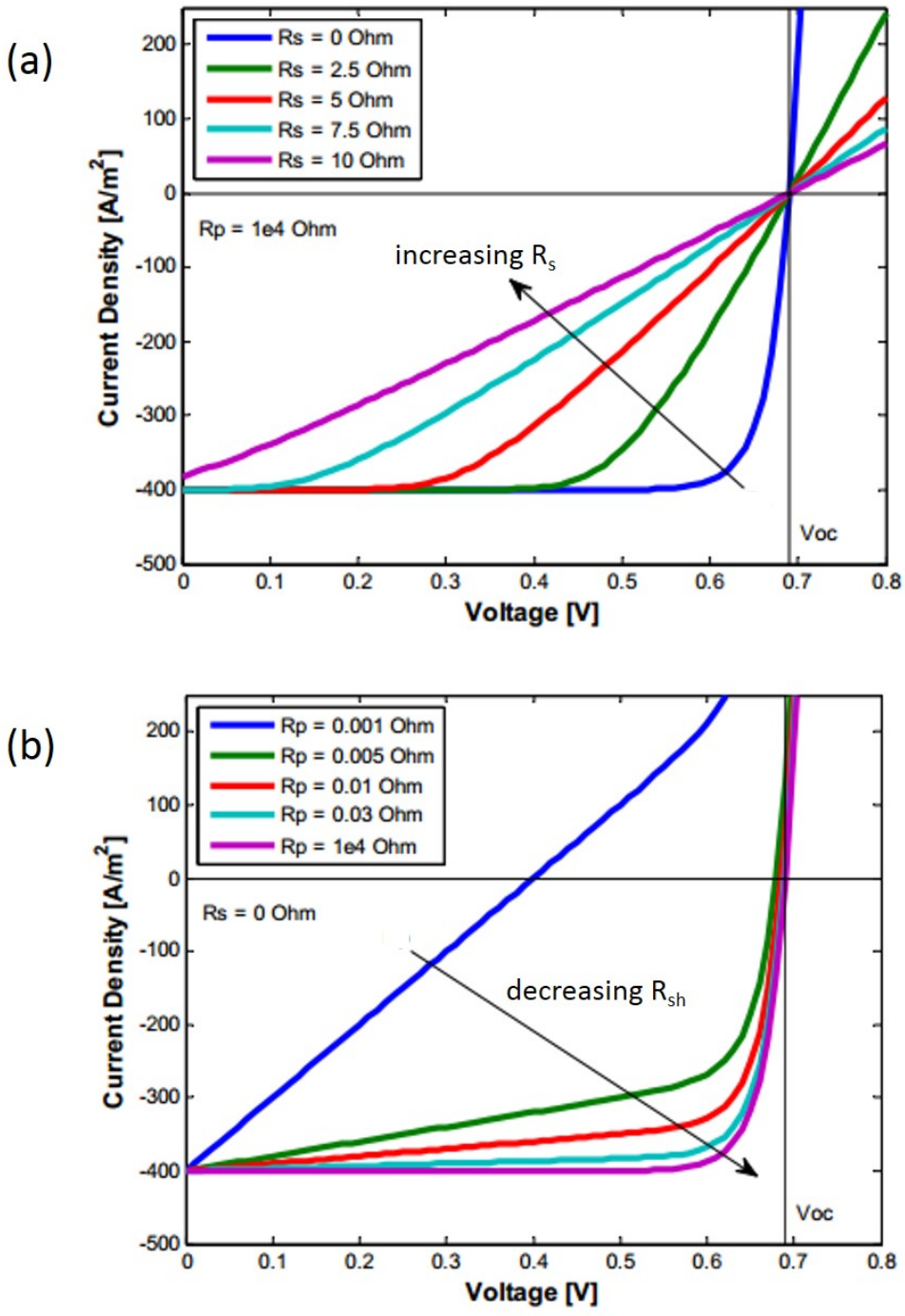


**Figure 2.2**: The effect of (a) series resistance ($R_s$) and (b) shunt resistance ($R_{sh}$, $R_\rho$) on J-V characteristics of solar cells.

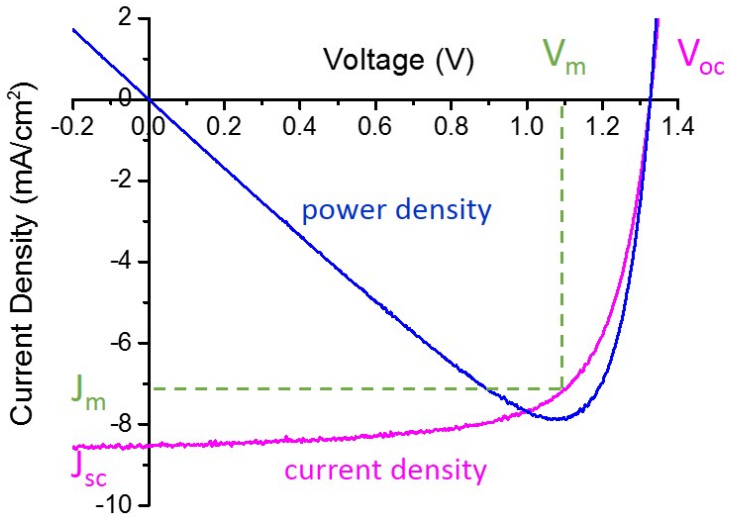


**Figure 2.3**: J-V and P-V characteristics of a GaNP thin film solar cell.

used as a means to compare the performance of solar cells.

$$\eta = \frac{P_m}{P_s} = \frac{J_m V_m}{P_s} \tag{2.4}$$

where $P_m$ is solar cell's maximum power density and $P_s$ is the power density of the incident light. Solar cell efficiency depends directly on the bandgap of the materials that comprise the solar cell. As such, to compare the cell performance of solar cells made of different materials, the bandgap ($E_g$) to $V_{oc}$ offset ($W_{oc}$) is used.

$$W_{oc} = \frac{E_g}{q} - V_{oc} \tag{2.5}$$

$W_{oc}$ has been theoretically and experimentally proven to be independent of $E_g$, and it is commonly used to perform for a fair comparison between solar cells that are comprised of different materials. Figure 2.4 depicts the theoretical and experimentally measured

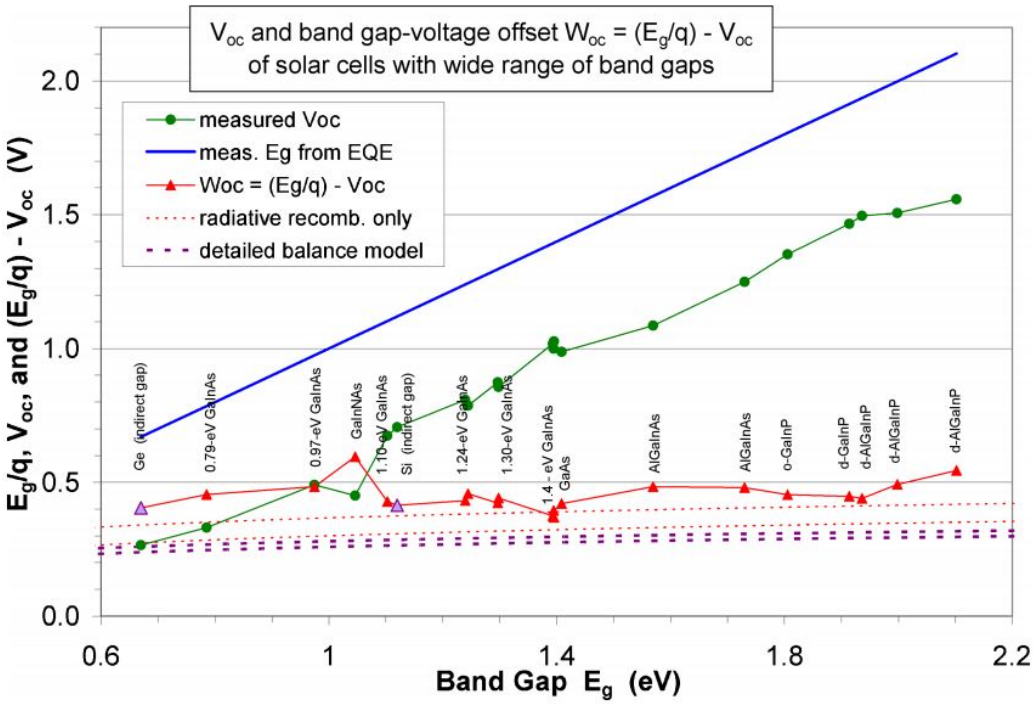


**Figure 2.4**: The theoretical and experimental data of bandgap to voltage offset as a function of bandgap.[34]

values of $W_{oc}$ as a function of $E_g$. Two theoretical models are shown: (1) one in which only radiative recombination is assumed and (2) one that derives $W_{oc}$ from the detailed balance model.[34] Both models calculate $W_{oc}$ as ~0.4 V, which is comparable to the experimental measurement.[34]

## 2.2 Short circuit current

In general, a solar cell junction is composed of three regions: (1) a neutral n-region, (2) a depletion region, and (3) a neutral p-region. The current through the device junction can be solved by using the semiconductor transport equations and Poisson's equation with appropriate boundary conditions. To simplify the problem, we assume that (1) there are no free carriers in the depletion region, (2) within the quasi-neutral

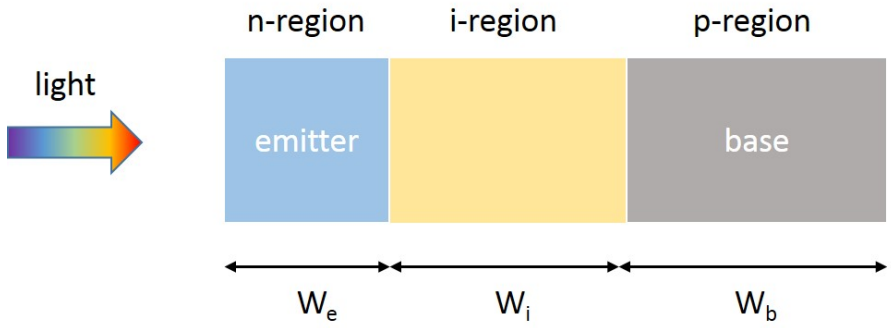


**Figure 2.5**: Schematic p-i-n solar cell showing emitter region, i-region, and base region.

regions, only the minority carriers determine the current, and (3) the minority carriers in the neutral regions are driven only by diffusion due to the absence of electric field.

In this work, we use a p-i-n junction for our solar cell, a schematic for which is shown in Figure 2.5. An n-type layer and a p-type layer are employed as an emitter and a base, respectively. Both layers possess a doping concentration of high-$10^{17}$ to mid-$10^{18}$ $cm^{-3}$, which creates a thin depletion width ($< 20$ nm) in each region, compared to the a thick depletion width in i-region ($> 500$ nm). Thus, our case simply uses the emitter width ($W_e$) as the neutral n-region, the i-layer width ($W_i$) as the depletion region, and the base width ($W_b$) as the neutral p-region.

Using the above assumptions, $J_{sc}$ can be calculated as:[35]

$$j_{sc}(E) = j_e(E) + j_b(E) + j_{i,gen}(E) \tag{2.6}$$

$$J_{sc} = \int_0^\infty j_{sc}(E)d(E) \tag{2.7}$$

where $j_e$ and $j_b$ are the minority carrier current densities from the emitter and the base regions, respectively, and $j_{i,gen}$ is the current density generated in the i-region. Each current density is given by:

$$j_e(E) = [\frac{qb_s(1-R)\alpha L_e}{\alpha^2 L_e^2 - 1}] \times [\frac{(\frac{S_e L_e}{D_e} + \alpha L_e) - e^{-\alpha W_e)}(\frac{S_e L_e}{D_e} cosh\frac{W_e}{L_e} + sinh\frac{W_e}{L_e})}{\frac{S_e L_e}{D_e} sinh\frac{W_e}{L_e} + cosh\frac{W_e}{L_e}} - \alpha L_e e^{-\alpha W_e}] \tag{2.8}$$

$$j_b(E) = [\frac{qb_s(1-R)\alpha L_b}{\alpha^2 L_b^2 - 1}] e^{-\alpha(W_e+W_i)} \times [\alpha L_{b-} \frac{\frac{S_b L_b}{D_b}(cosh\frac{W_b}{L_b} - e^{-\alpha W_b}) + sinh\frac{W_b}{L_b}) + \alpha L_b e^{-\alpha W_b}}{\frac{S_b L_b}{D_b} sinh\frac{W_b}{L_b} + cosh\frac{W_b}{L_b}}] \tag{2.9}$$

$$j_{i,gen}(E) = qb_s(1-R)e^{-\alpha We}(1 - e^{-\alpha W_i}) \tag{2.10}$$

where $b_s$ is incident spectral photon flux density; $R$ is the reflectance of the material; $\alpha$ is the absorption coefficient of the material; $L_e$ and $L_b$ are the diffusion length of minority carriers in the emitter and the base regions, respectively; $S_e$ and $S_b$ are the recombination velocities at the front and the back surface, respectively; and $D_e$ and $D_b$ are the diffusion coefficients of minority carriers in the emitter and the base regions, respectively.

The short circuit current also can be calculated by:

$$J_{sc} = q \int b_s(E) EQE(E) dE \tag{2.11}$$

where EQE is external quantum efficiency, which is the ratio of the number of electrons collected at the terminals of the cell to the number of incident photons. EQE is given by:

$$EQE = \frac{j_e(E) + j_b(E) + j_{i,gen}(E)}{qb_s(E)} \tag{2.12}$$

## 2.3 Open circuit voltage

Open circuit voltage ($V_{oc}$) is defined as the maximum possible potential across the terminals of the solar cell which occurs when the contacts are isolated (i.e., J = 0). $V_{oc}$ can be calculated by:

$$V_{oc} = \frac{nk_BT}{q} ln(\frac{J_{sc}}{J_o} + 1). \tag{2.13}$$

$J_o$ is dependent on the minority carrier diffusion current of the emitter and base regions ($J_{o,e}$ and $J_{o,b}$) as well as the recombination current of the depletion region.

$$J_o = J_{o,e} + J_{o,b} + J_{o,rec} \tag{2.14}$$

where

$$J_{o,e} = \frac{qD_eN_cN_v}{L_e} \times [\frac{\frac{S_eL_e}{D_e} cosh\frac{W_e}{L_e} + sinh\frac{W_e}{L_e}}{\frac{S_eL_e}{D_e} sinh\frac{W_e}{L_e} + cosh\frac{W_e}{L_e}}] \times e^{(\frac{-E_g}{k_BT})} \tag{2.15}$$

$$J_{o,b} = \frac{qD_bN_cN_v}{L_b} \times [\frac{\frac{S_bL_b}{D_b} cosh\frac{W_b}{L_b} + sinh\frac{W_b}{L_b}}{\frac{S_bL_b}{D_b} sinh\frac{W_b}{L_b} + cosh\frac{W_b}{L_b}}] \times e^{(\frac{-E_g}{k_BT})} \tag{2.16}$$

$$J_{o,rec} = qW_i\sqrt{\frac{N_cN_v}{t_et_b}} \times e^{(\frac{-E_g}{2k_BT})} \tag{2.17}$$

In indirect-bandgap material, carrier lifetime is long so very little recombination occurs in the depletion region. Consequently, the diffusion currents $J_{o,e}$ and $J_{o,b}$ likely dominate. Conversely, in direct-bandgap material, carrier lifetime is short resulting in more recombination in the depletion region. In this case, $J_{o,rec}$ likely dominates.

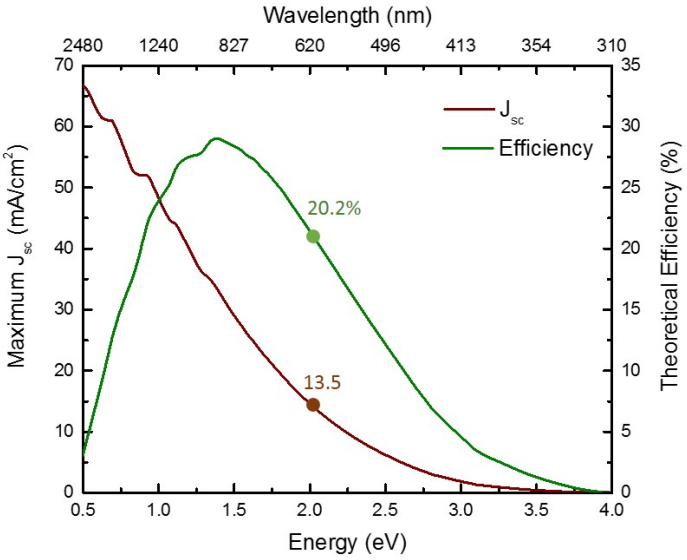


**Figure 2.6**: Calculated maximum short circuit current density and maximum efficiency as a function of bandgap.

## 2.4 Our GaNP solar cell design

In order to optimize our solar cell structure, we perform simulations on a p-GaP/i-GaNP/n-GaP solar cell, which is the structure used in this work, in various conditions. The MATLAB scripts used in calculation are shown in Appendix A. The default parameters used for this structure are listed in Table 2.1. In these calculations, we assume that all incident photons are absorbed in the solar cell (R=0) and that the dominate recombination mechanism is the Shockley-Read-Hall recombination.

### 2.4.1 The maximum $J_{sc}$ and $\eta$ under one sun

The maximum $J_{sc}$ of our GaNP solar cell is calculated using Equation 2.11. We assume AM 1.5G and that 100% of photons possessing greater energy than the cell bandgap are absorbed and converted into electricity at the terminals (i.e., EQE = 1). The resulting value of $J_{sc}$ is then used in combination with $W_{oc} = 0.4$ (see Section 2.1) and

**Table 2.1**: The parameters used in our calculations

| | |
|---|---|
| **General parameters** | |
| Bandgap ($E_g$) | 2.26 eV |
| Effective conduction band density of states ($N_c$)[36] | $1.8 \times 10^{-19}$ cm$^{-3}$ |
| Effective valence band density of states ($N_v$)[36] | $1.9 \times 10^{-19}$ cm$^{-3}$ |
| **Emitter (n-type)** | |
| Doping concentration ($N_e$) | $4 \times 10^{18}$ cm$^{-3}$ |
| Diffusion coefficient of minority carriers ($D_e$)[37] | 1.68 cm$^2$/s |
| Diffusion length of minority carriers ($L_e$)[21] | 190 nm |
| Recombination velocity ($S_e$)[38] | $1 \times 10^6$ cm/s |
| Width of emitter ($W_e$) | 100 nm |
| **Base (p-type)** | |
| Doping concentration ($N_b$) | $6.5 \times 10^{17}$ cm$^{-3}$ |
| Diffusion coefficient of minority carriers ($D_b$)[37] | 1.53 cm$^2$/s |
| Diffusion length of minority carriers ($L_b$)[37] | 4.1 $\mu$m |
| Recombination velocity ($S_b$)[38] | $1 \times 10^6$ cm/s |
| Width of base layer ($W_b$) | 300 $\mu$m |
| **intrinsic layer (i-layer)** | |
| Width of i-layer ($W_i$) | 1 $\mu$m |

Equation 2.3 to calculate the maximum $\eta$ of the cell. Using $E_g = 2.05$ eV GaNP, our GaNP solar cell is capable of providing a maximum $J_{sc}$ and $\eta$ of 13.5 mA/cm$^2$ and 20.2%, respectively, as depicted in Figure 2.6.

### 2.4.2 The effect of the i-layer width

In this study, we compare the EQE and $J_{sc}$ of various solar cells that use varying thicknesses of GaP or GaNP as its i-layer material. In this work, i-layer thickness is varied between 0 and 10 $\mu$m. Figure 2.7 shows the EQE of p-GaP/i-Ga(N)P/n-GaP solar cells with different i-layer thicknesses ($W_i$). The corresponding $J_{sc}$ is shown in Figure 2.8. As can be seen in the figure, increasing $W_i$ improves long-wavelength EQE for both the i-GaP and i-GaNP cells, but the improvement is more pronounced in i-GaNP. This is due to better absorption in direct-bandgap GaNP in comparison to indirect-bandgap GaP. Furthermore, the graphs show that the i-GaP sample needs to be thicker than $\sim$10 $\mu$m in order to maximize long-wavelength EQE whereas the i-GaNP sample only needs to be $\sim$ 5 $\mu$m thick. We also note that $W_i$ has negligible impact on short-wavelength EQE for both samples. Thus, other parameters (e.g., emitter width, recombination velocity at the surface) must be used to improve short-wavelength EQE performance.

### 2.4.3 The effect of the emitter width

In order to enhance short-wavelength EQE, which is independent of $W_i$, the effect of the emitter, where short-wavelength photons are mostly absorbed, is studied. An emitter is typically a highly-doped region that results in very short $L_e$, which is $\sim$190 nm in our case. In our simulations, the thickness of the emitter ($W_e$) is varied from 50 nm to 1 $\mu$m. In the thick emitter region ($W_e > L_e$ ), the generated carriers outside the $L_e$ range recombine before transporting across the junction and, consequently, they do not

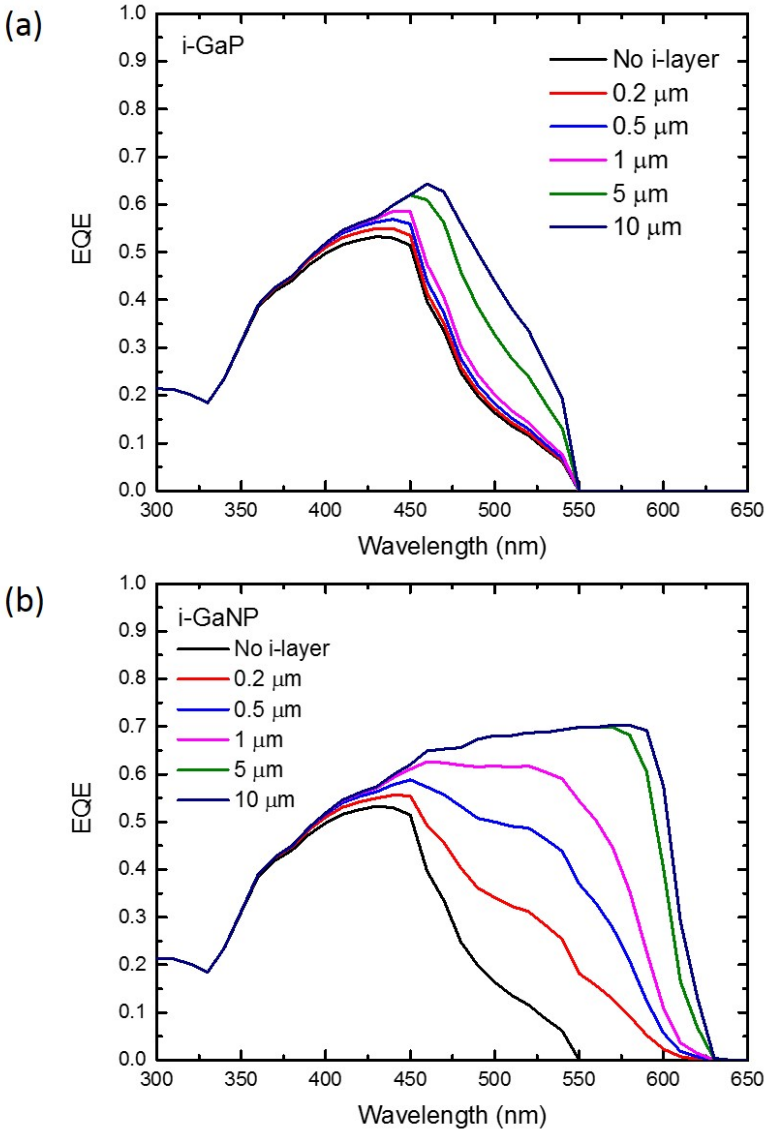


**Figure 2.7**: Calculated EQE from p-i-n solar cell utilizing (a) GaP, and (b) GaNP as an i-layer, of which thickness is varied.

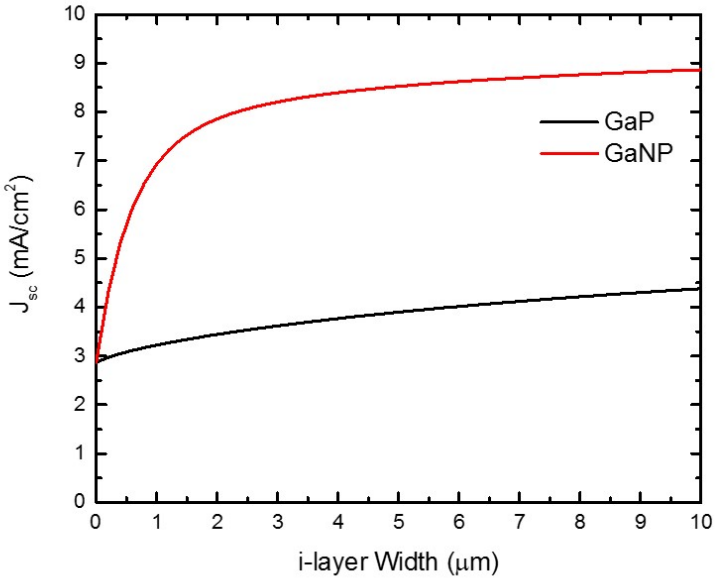


**Figure 2.8**: The corresponding short circuit current density as a function of i-layer thickness.

contribute to the current. Utilizing a thinner emitter layer ($W_e < L_e$ ) shows improved response to short-wavelength photons, as shown in Figure 2.9(a), resulting in improved $J_{sc}$ as seen in Figure 2.9(b). Even though the simulation results show that the emitter needs to be as thin as possible in order to obtain optimal short-wavelength response, a very thin emitter ($L_e \leq 20$ nm) would likely be impractical. At very small values of $L_e$, the emitter layer would likely to be completely depleted and would likely to have high contact resistance, which our simulation does not account for. We also note that varying the emitter thickness shows no significant impact on long-wavelength EQE, which is in line with the fact that long-wavelength photons are primarily absorbed deep in the cell (i.e., not in the emitter) because of their long absorption depth.

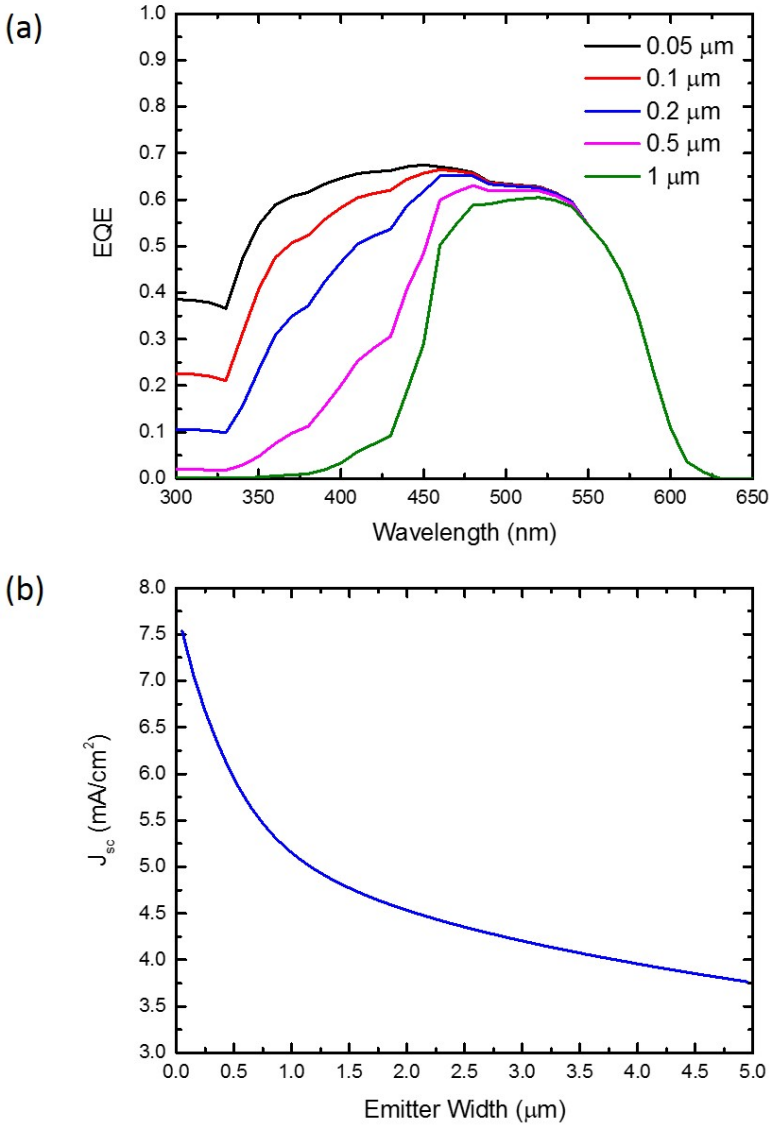


**Figure 2.9**: EQE and corresponding short circuit current density as the effect of emitter thickness.

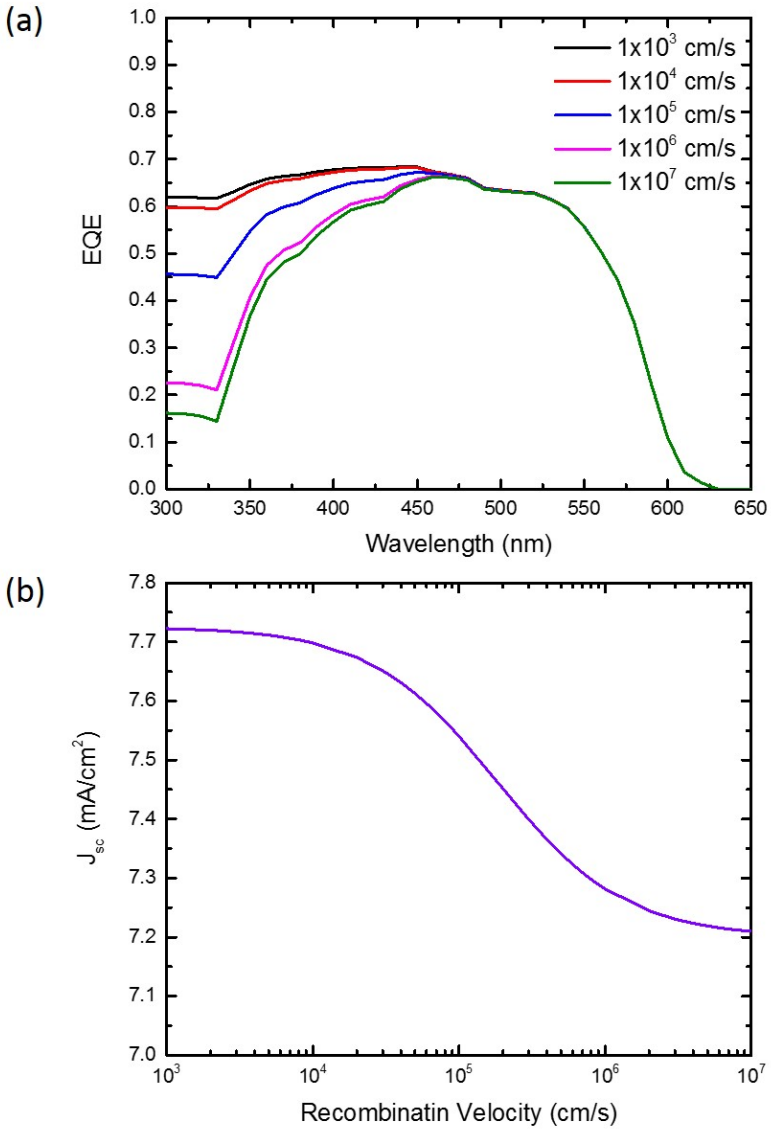


**Figure 2.10**: EQE and corresponding short circuit current density as the effect of recombination velocity at the surface.

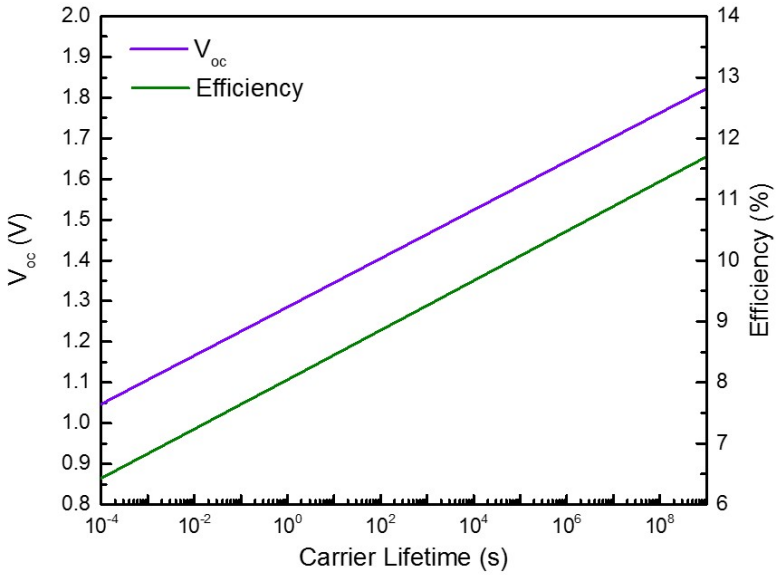


**Figure 2.11**: Open circuit voltage and corresponding efficiency as a function of carrier lifetime.

### 2.4.4 The effect of recombination velocity at the front surface

Another factor that affects short-wavelength EQE response is recombination velocity on the cell surface. Figure 2.10 shows the EQE response of solar cells with various recombination velocities and their corresponding $J_{sc}$. A typical GaP layer possesses a recombination velocity of $10^6$ cm/s which, according to Figure 2.10, results in poor short-wavelength EQE response. This is attributed to significant surface recombination, which can be mitigated/eliminated by surface passivation to reduce the recombination velocity at the surface.

### 2.4.5 The effect of carrier lifetime in the i-layer

In this study, the effect of carrier lifetime in the depletion region is examined. Figure 2.11 shows $V_{oc}$ and $\eta$ as a function of carrier lifetime. Note that we assume the

carrier lifetimes of electrons and holes are the same. From the figure, we can see that the carrier lifetime has a direct effect on $V_{oc}$, which, consequently has a direct effect on $\eta$. Longer lifetime reduces recombination current, which results in greater $V_{oc}$. Note that, carrier lifetime is proportional to the quality of GaNP film. Thus, in order to obtain high $V_{oc}$, the defects in films need to be minimized.

# Chapter 3

# Experiment Procedures

## 3.1 Overview

This Chapter describes our gas-source molecular beam epitaxy (GSMBE) modified to handle gas sources ($PH_3$ and $AsH_3$) and its N plasma source. In addition, several techniques used for material characterization including photoluminescence (PL), current density-voltage (J-V), and external quantum efficiency (EQE) measurements are described. Finally, the fabrication and optimization techniques (i.e., rapid thermal annealing (RTA), mesa etch, metallization) are discussed.

## 3.2 Growth

This section describes GSMBE system, which was used to grow all the devices in this study including thin films, shells of core/shell microwires, and core/shell nanowires. In addition, N plasma, which is an extremely important aspect of dilute nitride growth, is described.

### 3.2.1 Gas-source molecular beam epitaxy

Molecular beam epitaxy (MBE) was invented in the late 1960s at Bell Telephone Laboratories by J.R. Arthur and Alfred Y. Cho.[39] MBE is an advanced ultra-high vacuum (UHV) evaporation technique, which provides atomic-level precision and produces high-purity films. MBE has been widely used for growing thin epitaxial structures made of semiconductors. The composition of the grown films and their doping level depend on the deposition rate of the sources. The typical growth rate is $\sim$1 $\mu$m/h or $\sim$1 monolayer/s, which is slow enough to ensure surface migration of adatoms on the growing surface. Consequently, the surface of the grown film is very smooth. The growth rate of a III-V compound semiconductor is determined by the group-III flux. An overpressure of group-V is provided. The ultra-high vacuum environment allows the use of in-situ monitoring techniques such as reflection high-energy electron diffraction (RHEED). RHEED intensity oscillations are used to determine the growth rate and composition of an alloy, and it is key in enabling the fabrication of sophisticated device structures using MBE.

Gas-source MBE (GSMBE) was introduced in 1980 bringing with its several advantages over traditional MBE.[40] First, GSMBE provides better composition control of mixed group-V compounds enabling the growth of ternary and even quaternary compounds. The flux of group-V material can also be abruptly changed, which facilitates greater device structure flexibility. In addition, the use of thermally cracked arsine and phosphine gases as precursors in GSMBE generates $P_2$ and $As_2$. These dimers possess a higher accommodation coefficient on the growing semiconductor surface than $P_4$ and $As_4$, which are generated by heating solid elemental phosphorus and arsenic in traditional MBE.

Our lab employs a Varian Gen-II MBE modified to handle group-V hydride gas sources. The schematic of our GSMBE system is shown in Figure 3.1. Solid elemental

Al, Ga, and In are used as the group-III sources. Solid elemental Be and Si are used as p-type and n-type dopants, respectively. All group-III fluxes and dopant sources are controlled by varying the temperature of the Knudsen effusion cells. $AsH_3$ and $PH_3$ gases, which are installed in two separate gas cabinets together with potassium permanganate scrubbers, are used as the group-V sources. These gases are introduced into the growth chamber through crackers that are heated to 1000 °C. The crackers thermally decompose $AsH_3$ and $PH_3$ into $As_2$ and $P_2$ as well as $H_2$ by-product before reaching the substrate. The fluxes of the group-V sources are controlled by mass flow controllers (MFCs). The maximum calibrated fluxes of $As_2$ and $P_2$ are 5 sccm and 20 sccm, respectively. All furnaces are equipped in the front with mechanical shutters and pneumatic shutters, which are used to cut off the beams when growth is not desired.

Our GSMBE system consists of three chambers: (1) growth chamber, (2) buffer chamber, and (3) loadlock chamber. The growth chamber vacuum is maintained by an Ebara cryo-pump with a pumping speed of 2200 l/s and a Pfeiffer Model TM U1600 turbo pump with a pumping speed of 1500 l/s. In addition to the pumps, liquid nitrogen shrouds encompassing growth chamber and the sources are used to condense background molecules that inhibit growth of high-purity layers. Typical background pressure in the growth chamber with fed liquid nitrogen and sources heated to operating temperatures is in the low-$10^{-8}$ Torr. When group-V gas is introduced in the growth chamber, the chamber pressure increases to low-$10^{-5}$ Torr. The buffer chamber and loadlock chamber vacuum are maintained by an ion pump and a small turbo pump, respectively.

### 3.2.2 N plasma source

A radio-frequency (RF) plasma N source is used for N incorporation in our studies. This is the most common technique for N plasma source because it provides stable excited $N_2$ molecules and atomic N flux with good uniformity. The N plasma

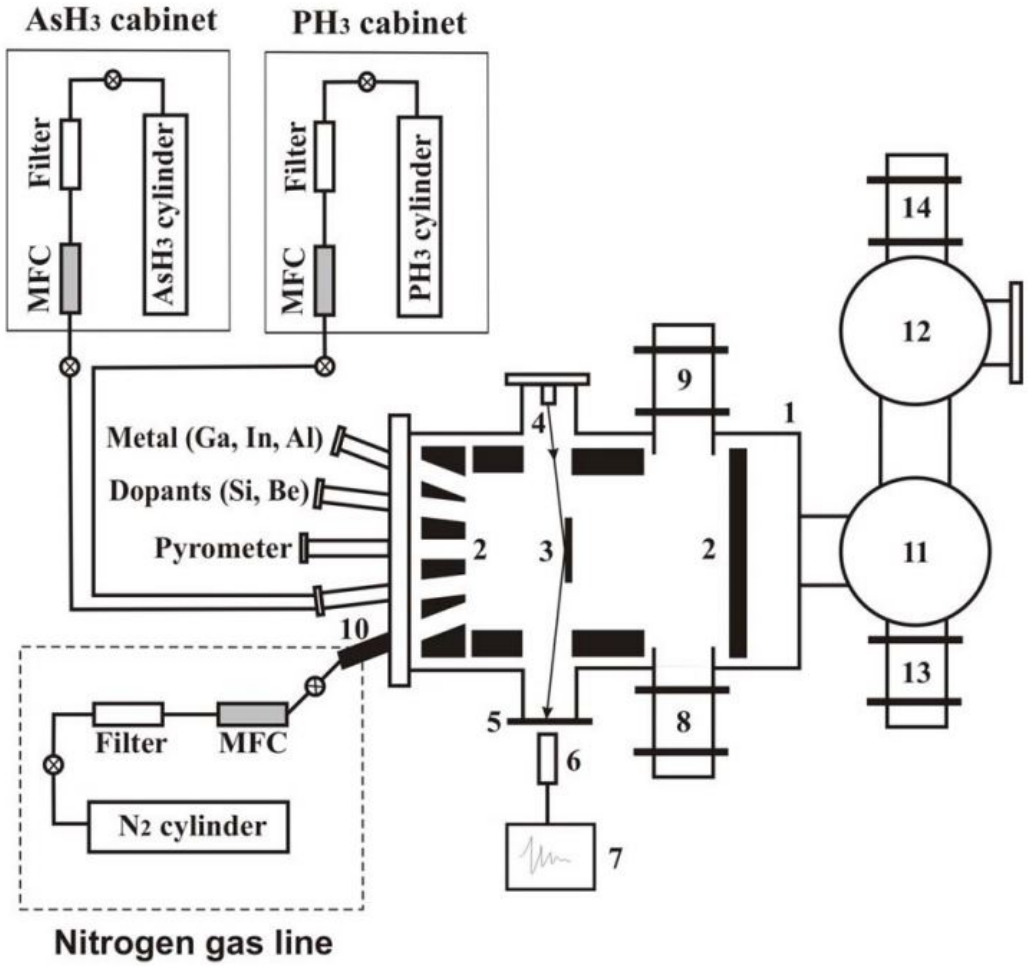


**Figure 3.1**: Schematics of the modified Varian Gen-II gas-source molecular beam epitaxy (Adapted from V. Odnoblyudov's Ph.D. thesis, UCSD, 2006).

source is generated in multiple steps. First, ultra-high purity (99.99%) $N_2$ gas is sent through a regulator, which maintains a constant pressure of 50 psi. The regulated gas is then purified using a Matheson Gases & Equipment 6190-V4MM Membrane to remove water vapor and $O_2$. The resultant $N_2$ flux is then sent through an MFC and an RF plasma excited at 13.56 MHz, which is created by an Oxford Applied Research Model MPD21 RF plasma generator. Within the RF plasma, active N radicals are generated and injected into the growth chamber through a beam exit aperture, which has 16 holes each with a diameter of 0.3 mm. The final component is a shutter that is used to cut off the N radical beam when no N is required.

The N plasma discharge described earlier is generated in a pyrolytic boron nitride (PBN) tube by inductively-coupled RF excitation at 13.56 MHz. The resultant N plasma discharge is composed of (1) the desired N radicals, which are used in the growth; (2) inert $N_2$ molecules, which do not participate in the growth process; and (3) $N_2$ ions, which do not incorporate into films, but negatively impact growth by bombarding the surface of the growing films. The undesired surface ion bombardment can be mitigated by employing parallel deflector plates and establishing an electric field between them to divert the ion beam away from the substrate. However, our system does not have this feature.

The composition and rate of plasma discharge are controlled using two primary factors, RF power and $N_2$ flux. The effect of these parameters on the resultant plasma discharge varies and can be inferred by monitoring the plasma discharge's optical emission intensity, which is monitored using a Si photodetector in our system. The relationship between RF plasma, $N_2$ flux, and optical emission intensity is illustrated in Figure 3.3, the data for which was produced experimentally by previous students. Examining the black lines, we note that for a fixed RF power, the optical emission intensity levels off as flux increases. This indicates the generation of N radicals is saturating (i.e., poor flux to N

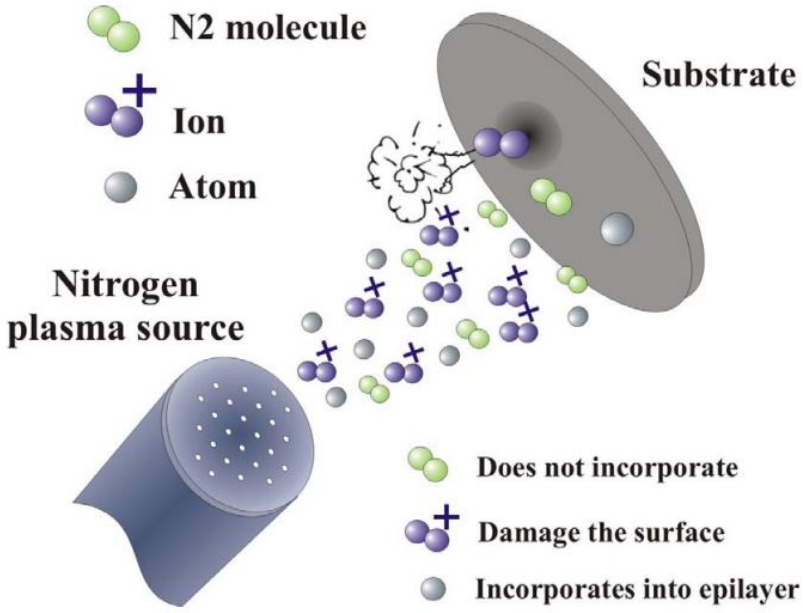


**Figure 3.2**: Schematic of the N plasma source and N species produced by plasma discharge (Adapted from V. Odnoblyudov's Ph.D. thesis, UCSD, 2006).

radical conversion efficiency). Note that, increasing the flux increases pressure which is detrimental to growth. Also, the proportional of undesired $N_2$ ions increases as RF power increases (>350 W) resulting in poor samples. Taken together, the optimal plasma source conditions are those encircled in the lower left corner of 3.3. These conditions result in a low pressure growth environment and provide maximum plasma source efficiency.

### 3.2.3 Reflection high-energy electron diffraction

Reflection high-energy electron diffraction (RHEED), which is an in-situ surface analytical technique, is commonly employed in MBE to (1) investigate the surface quality of the grown film and substrate and (2) calibrate growth rate. This geometry of RHEED is suitable to MBE because a high energy electron beam from RHEED gun is at grazing incidence (1°-3°), while atomic or molecular beams hit almost normally on the substrate. Because of the grazing incidence, the penetration of the beam into the surface is low (only

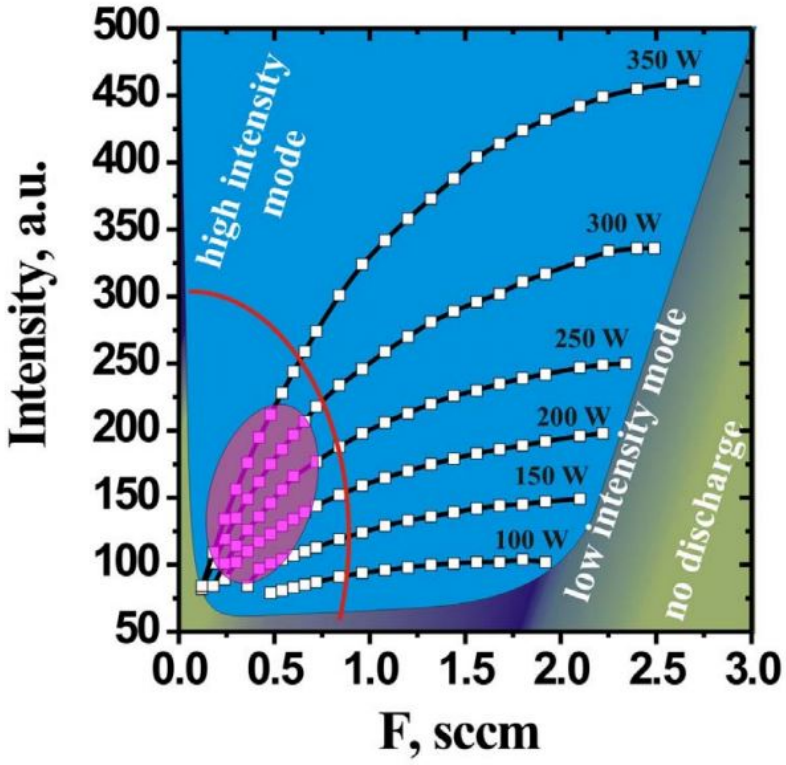


**Figure 3.3**: The experimental dependence of the plasma intensity as a function of the $N_2$ flux at a given applied RF power (Adapted from V. Odnoblyudov's Ph.D. thesis, UCSD, 2006).

a few atomic layers). To investigate surface quality, first the high energy electron beam hits a sample and the reflected beam of electrons construct a pattern of reciprocal space map of the sample which can be explained by using Bragg's law. Such RHEED patterns are displayed on a phosphorous screen. Streaky patterns indicate an atomically smooth surface. In contrast, spotty patterns indicate a poor-quality film i.e., three-dimensional island growth.

When the growth is initiated, the RHEED intensity exhibits an oscillatory behavior. The oscillation period is commonly used to calibrate the beam flux to accurately control the growth rate, layer thickness, and alloy composition. In our experiment, as seen in Figure 3.4, we use RHEED oscillation induced by group-III adatoms under group-

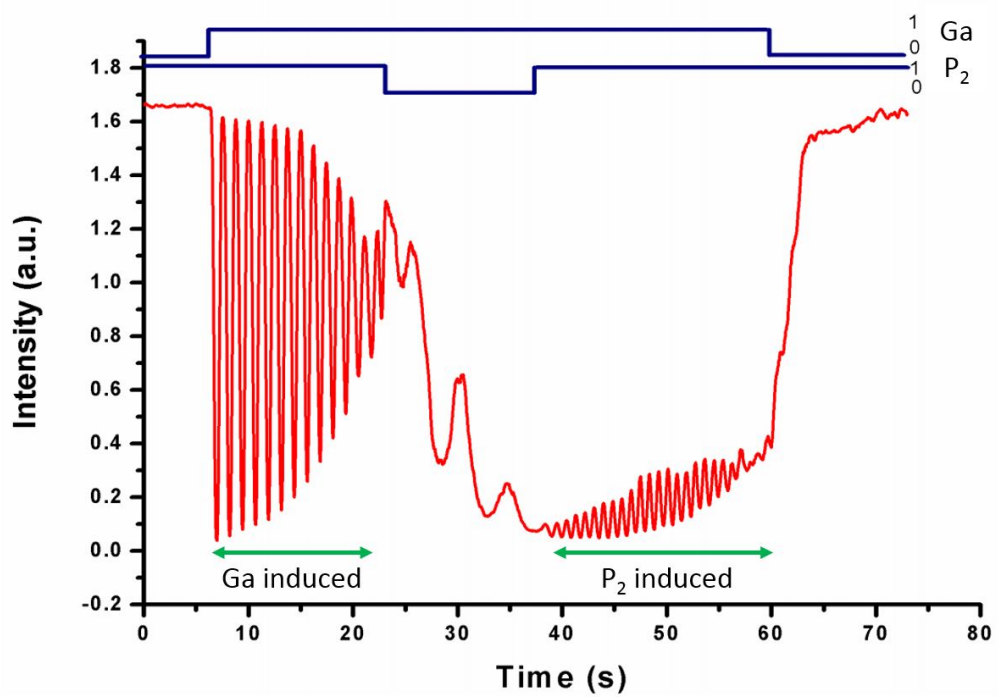


**Figure 3.4**: Ga and $P_2$ induced RHEED oscillation (Adapted from Y. J. Kuang's Ph.D. thesis, UCSD, 2014). The top of the graph shows the status of Ga and $P_2$ shutters i.e., 1 is open, and 0 is close.

V overpressure to calculate the incorporation rate of Ga. On the other hand, RHEED oscillation induced by group-V adatoms on a surface with excess group-III adatoms is used to calculate P incorporation rate. Thus, the V/III incorporation ratio reported in this work is the ratio of P and Ga incorporation rate.

## 3.3 Characterization

This section describes the characterization method we employ. After a sample is grown, PL measurements are performed to determine its optical properties. The sample is then fabricated into solar cells, which are then characterized using J-V and EQE measurements to determine the overall solar cell performance.

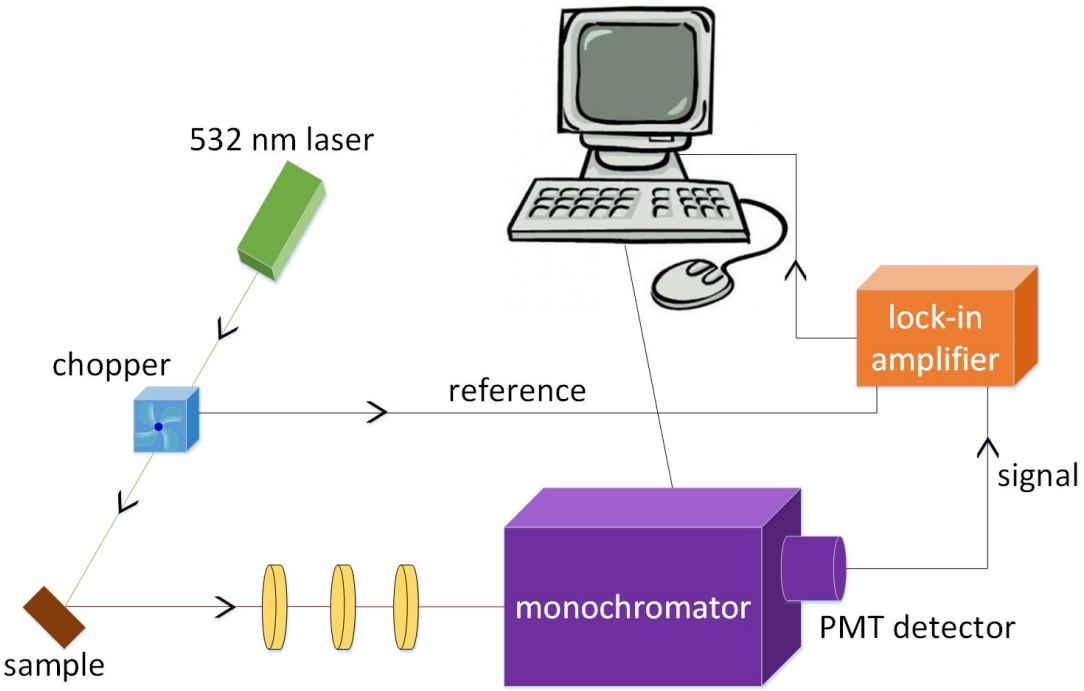


**Figure 3.5**: Schematic of our PL measurement setup.

### 3.3.1 Photoluminescence

Photoluminescence (PL) is the technique we use to characterize the optical properties of materials in this study. In a PL experiment, a semiconductor sample is excited by photons, which have an energy larger than the semiconductor's bandgap. As a result of this excitation, electron-hole pairs are generated, which then recombine radiatively with the emission of photons (luminescence). The energy of the emitted photons roughly corresponds to the bandgap of the excited material since the recombination of the electron-hole pair represents the transition of electrons from the conduction band to the valence band.

The PL measurement system we employ in this work is depicted in Figure 3.5. A 50 mW semiconductor laser with an output wavelength of 532 nm is used as the light source. First, the laser is sent through a chopper in the lock-in technique to mitigate noise signal from external source before striking the sample. Then the light emission from the sample is dispersed by wavelength inside a SPEX1870 monochromator and detected by

a downstream Hamamatsu R636-10 photomultiplier tube (PMT). The last component, a lock-in amplifier, works in conjunction with the chopper by sampling the output of the PMT at the same frequency. By doing so, noise from external light sources is eliminated.

### 3.3.2 Current-voltage characteristic

Current-voltage (I-V) measurement is used to investigate the performance of solar cells. The important parameters obtained from this measurement are (1) solar cell efficiency ($\eta$), (2) short-circuit current ($J_{sc}$), (3) open-circuit voltage ($V_{oc}$), and (4) fill factor (FF). The relationship of between these parameters is described in Section 2.1. In our I-V measurement setup, a Newport 67015 solar simulator using a 150 W Xenon lamp equipped with a 1.5 AM filter is used as a light source. A 1 cm $\times$ 1 cm calibrated PV Measurements, Inc. Si solar cell is used as a reference cell to calibrate the intensity of the light source to AM 1.5G (100 mW/cm$^2$) for measurements. A DY2300 potentiostat instrument and its software are used to apply the voltage and measure generated current.

### 3.3.3 External quantum efficiency

External quantum efficiency (EQE) is the ratio of the number of carriers collected by a solar cell to the number of incident photons at a given energy. Our EQE measurement system is shown in Figure 3.6. EQE is performed as follows: light from a solar simulator is dispersed by wavelength inside a Cornerstone 260 monochromator and only desired wavelength of the light is allowed through a slit to strike the sample. When the single-wavelength light strikes the sample, current is generated and measured by a picoammeter. This process is done for all wavelengths of interest, and the results are consolidated by a computer into a graph. In the experiment, a calibrated Newport 818-UV Si p-i-n photodiode without OD3 attenuation is employed as a reference. The EQE is calculated

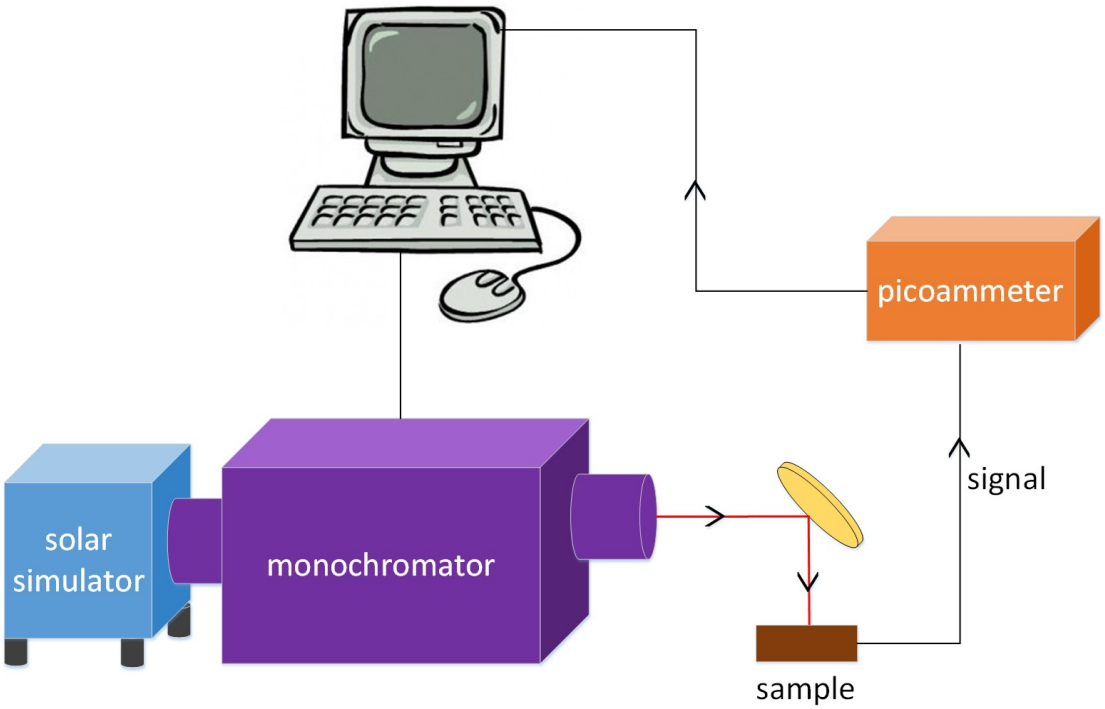


**Figure 3.6**: Schematic of our EQE measurement setup.

as:

$$EQE = R_{\lambda,sample}\frac{q}{h\nu} = \frac{R_{\lambda,sample}}{\lambda} \times 1240 \tag{3.1}$$

where $R_{\lambda,sample}$ is the photoresponsivity of the sample, $q$ is electronic charge, $h$ is Planck's constant, $\nu$ is incident photon frequency, and $\lambda$ is the photon wavelength. $R_{\lambda,sample}$ is calculated as:

$$R_{\lambda,sample} = \frac{J_{sample}}{P_{inc}} = R_{\lambda,ref}\frac{J_{sample}}{J_{ref}} \tag{3.2}$$

where $J_{sample}$ and $J_{ref}$ are the measured current density from the sample and the reference, respectively, $P_{inc}$ is the incident optical power, and $R_{\lambda,ref}$ is the photoresponsivity of the reference.

## 3.4 Solar cell fabrication

This section describes the fabrication process employed for our solar cells. Each solar device begins with a grown sample about 0.5 cm $\times$ 0.5 cm to 1 cm $\times$ 1 cm in size. The processes described here include RTA, mesa etch, and mineralization.

### 3.4.1 Rapid thermal annealing

Dilute nitride materials often contain a significant number of defects, notably anti-site defects, due to the combination of N incorporation, relatively low growth temperature, and ion damage from RF N plasma. Post-growth RTA is employed to mitigate such defects, which degrade the solar cell performance of the device.[41–43]

Rapid thermal annealing (RTA) is performed using AG Associates Heatpulse 610 RTA tool. To optimize the process, GaNP samples are annealed under $N_2$ ambient over a series of temperatures for 30 s. The optical properties of each sample were then characterized using PL, with a high PL intensity corresponding to a smaller number of defects. Figure 3.7 shows the results of this characterization. As expected, the as-grown sample exhibits very low PL intensity. With respect to the annealed samples, we observed that PL intensity increases as temperature increases. The maximum PL intensities we observed are obtained from an annealing temperature of 750 °C and 800 °C. Beyond this temperature, and as noted in one of our previous studies, mutual passivation begins to occur. Active Si dopants in the dilute nitride are passivated by N to form Si-N pairs resulting in reduced doping concentration of the material. To avoid this, an annealing temperature of 750 °C is determined as the optimal temperature for RTA, and RTA at this temperature is employed on all device in this dissertation.

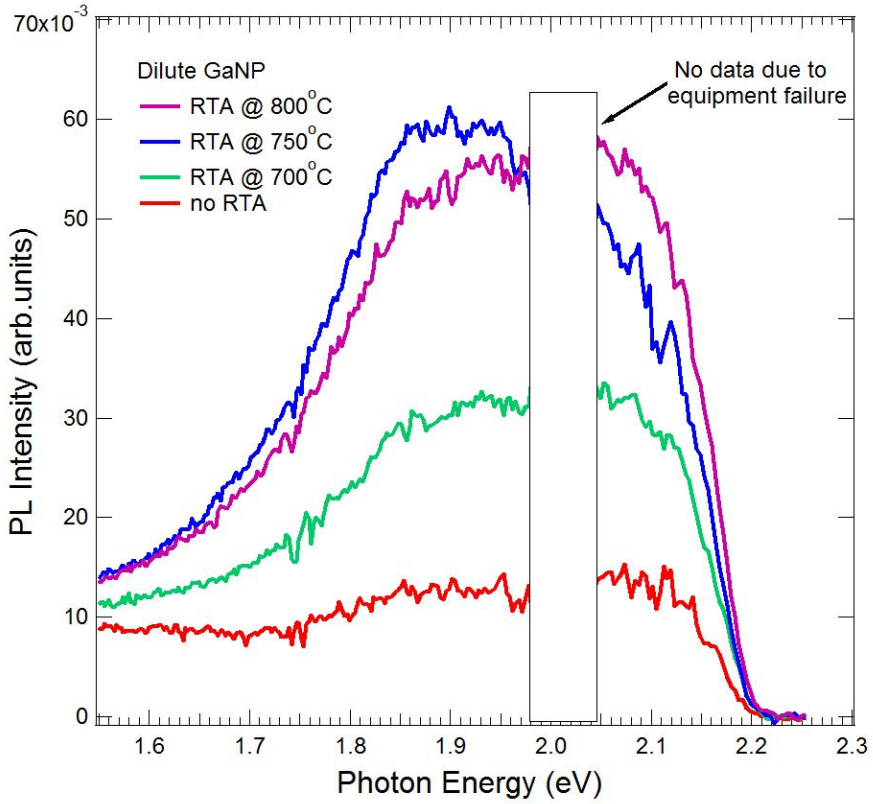


**Figure 3.7**: PL performance after RTA for GaNP samples.

### 3.4.2 Mesa etch

Mesa etching is performed after RTA. Mesa etching by reactive-ion etching (RIE) is employed to prevent short circuits at the edges of the cell and also to define the dimensions of the active cell as shown in Figure 3.8. In our experiment, prior to etching, an etch mask is fabricated by spinning photoresist onto the sample and subsequently photolithography is used to create the pattern mask. The mesa etch is performed by RIE using an Oxford Plasmalab 80 equipped with a 13.56 MHz RF source. The etching gases used are $Cl_2$ and $BCl_3$. As with RTA, we determined the optimal RIE conditions experimentally. Refer to chapter 6 for a detailed description of the optimization process.

The xperimentally-determined optimal conditions for RIE are as follows: 5 sccm of $Cl_2$ and 100 sccm of $BCl_3$ gas with an RIE power and pressure of 200 W and 36.5

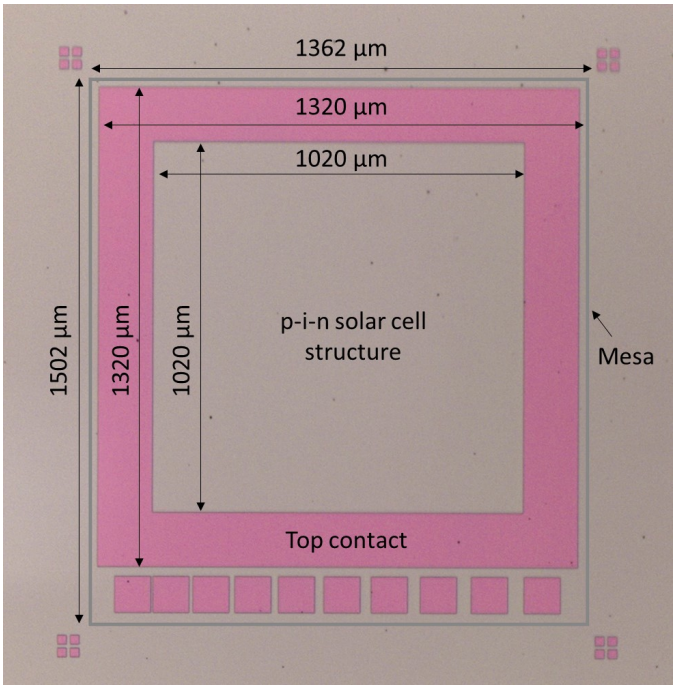


**Figure 3.8**: Our p-i-n GaNP solar cell under optical microscope.

mTorr, respectively. The resultant etching rate under these conditions is approximately 0.4 $\mu$m/min. A 6-minute mesa etch is preformed on all samples to obtain a mesa with a height of approximately 2.5 $\mu$m.

### 3.4.3 Metallization

The n-type top contact is deposited by using a Temescal BJD 1800 electron-beam (e-beam) evaporator. This tool utilizes a high-energy electron beam to vaporize a source material target that is directionally deposited onto the sample. The thickness of the deposited metal is monitored using a 6 MHz quartz crystal thickness monitor.

For our contact to n-type GaP, Pd and Si targets are used. The device is first masked with photoresist, and then a 50 nm layer of Pd is deposited followed by a 75 nm layer of Si. The evaporation rate of each material is $\sim$0.5 $\mathring{A}$/s. The evaporation process takes place in a high-vacuum chamber. During the evaporation process, the pressure is in

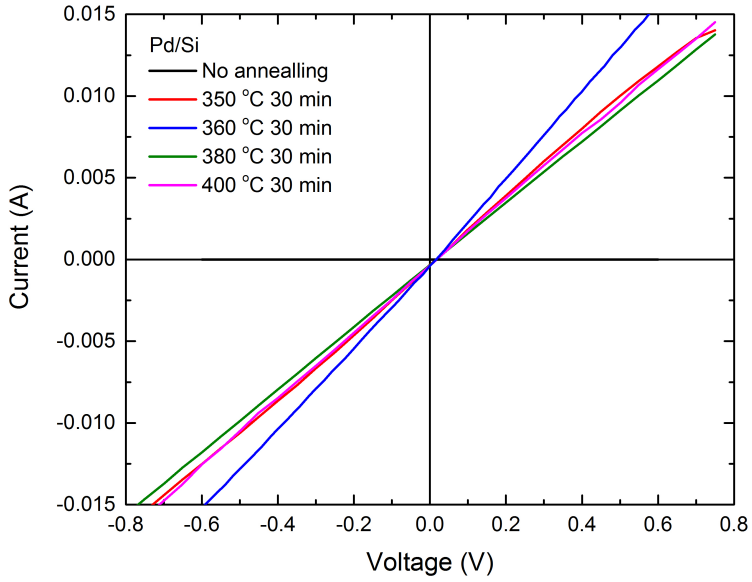


**Figure 3.9**: I-V characteristics of Pd/Si contact on n-type GaP.

the high-$10^{-7}$ Torr.

The p-type bottom contact is deposited by using an Edwards E306A thermal evaporator, which uses heat from a filament to vaporize metal pellets. As with the e-beam evaporator, a 6 MHz quartz crystal is used to determine the thickness of the deposited metal.

For our contact to p-type GaP, a Au/Zu/Au multilayer structure is used. The device is first deposited by a 20 nm layer of Au, followed by a 30 nm layer of Zn, and a final 30 nm layer of Au. The evaporation rate of each material is in the range of 0.5 - 1 *Å*/s. The process occurs in a high-vacuum chamber with a pressure in the low-$10^{-6}$ Torr.

After each metal contact deposition, thermal annealing is performed to assure the alloying of the deposited metal with the underlying semiconductor. More importantly, it produces an ohmic contacts. To optimize the annealing conditions, various temperatures and time are employed on Pd/Si and Au/Zn/Au contacts as illustrated in Figure 3.9 and Figure 3.10, respectively.

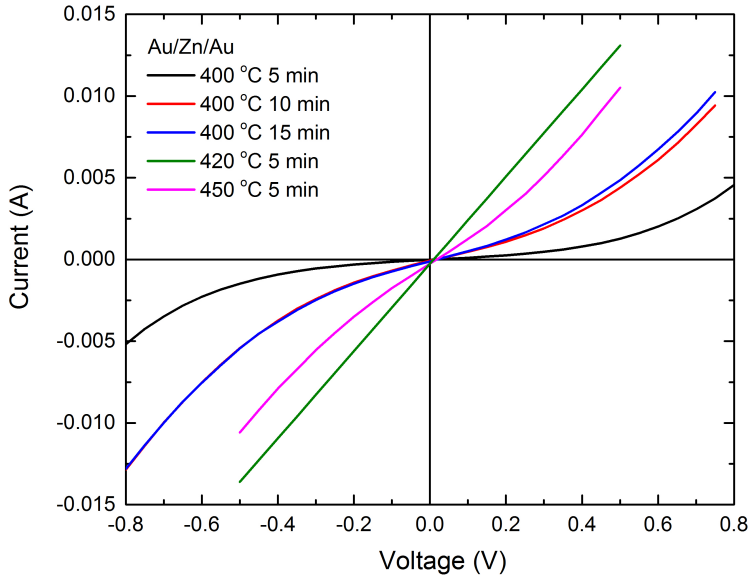


**Figure 3.10**: I-V characteristics of Au/Zn/Au contact on p-type GaP.

The Pd/Si contact is annealed with foaming gas (5% $H_2$ balanced with $N_2$) for 30 minutes at 350 °C, 360 °C, 380 °C, and 400 °C. As seen in Figure 3.9, ohmic contact behavior results under all conditions with only a slight variation in resistance. Thermal annealing at 360 °C is selected as the optimal condition as it provides the smallest resistance of $\sim 6 \times 10^{-4}$ Ω-cm$^2$.

The Au/Zn/Au contact was initially annealed at 400 °C for 5 minutes, 10 minutes and 15 minutes. The resultant I-V characteristics of the contacts annealed under these conditions, shown in Figure 3.10, clearly demonstrate non-ohmic behavior. Consequently, the annealing temperature is raised to 420 °C for 5 minutes and 450 °C for 5 minutes. Their resultant I-V characteristics conclude that the only condition to produce ohmic behavior is annealing at 420 °C for 5 minutes, making it the optimal annealing condition for p-type contact. The contact resistance of a contact annealed under this condition is $\sim 6.8 \times 10^{-5}$ Ω-cm$^2$.

# Chapter 4

# GaNP Thin Film Solar Cells

## 4.1 Overview

This Chapter is devoted to the optimization and demonstration of $\sim$2.05 eV ([N] $\sim$ 1.8%) GaNP thin film solar cells on GaP (001) substrate as a first step toward the integration of GaNP on Si. This GaNP layer is almost lattice-matched with Si. A high-resolution Discover D8 X-ray diffraction (XRD) system with a Bruker rotating anode diffractometer and a FEI Tecnai F30 300kV transmission electron microscope (TEM) are employed for determining N concentration and structural characterization, respectively. Solar cell performance is determined by using current density-voltage (J-V) and external quantum efficiency (EQE) measurements. Finally, we compare our solar cell performance with the most efficient GaP solar cell to date as well as direct-bandgap InGaP and GaAsP solar cells.

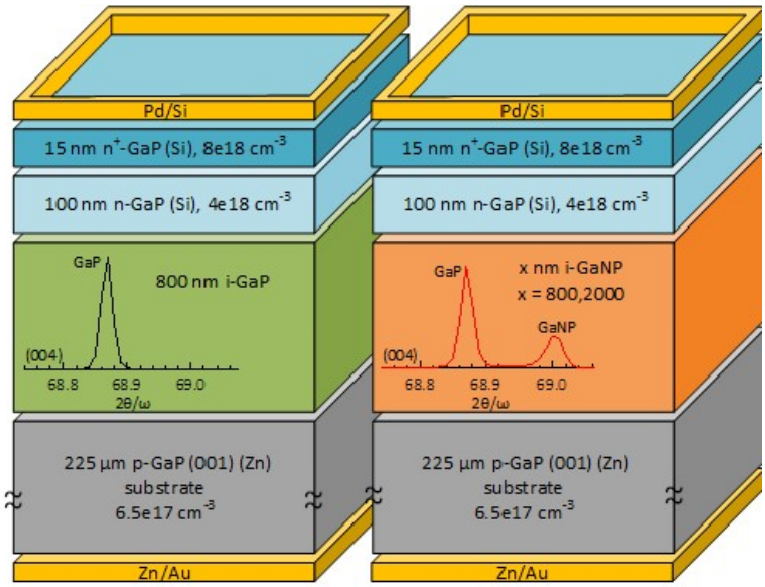


**Figure 4.1**: Cross-section schematic of the solar cells presented in this work. Insets are the measured XRD spectra. The XRD spectra of the GaNP samples confirm proper incorporation of N.

## 4.2 Device structures

To explore the range of GaNP solar cell performance, we conducted a systematic study to correlate the GaNP material quality with their device figures of merit. Figure 4.1 shows a cross-section of our solar cell structures. Their band diagram is depicted in Figure 4.2. The p-i-n GaP solar cell is used as the control sample. To compare GaP and GaNP, the second sample is identical to the control sample except that i-GaP is replaced with i-GaNP. For further improvement, the i-GaNP thickness of a third sample is increased to 2000 nm to allow more efficient optical absorption. Henceforth, these three samples will be referred to as <material>-<i-layer thickness>: GaP-800, GaNP-800, and GaNP-2000, respectively.

Regarding our solar cell structures (Figure 4.1), highly doped p-type ($6.5\times10^{17}$ $cm^{-3}$) GaP (001) is chosen as the substrate to minimize series resistance to the back contact. The next layer, i-Ga(N)P, serves to enhance carrier collection by extending

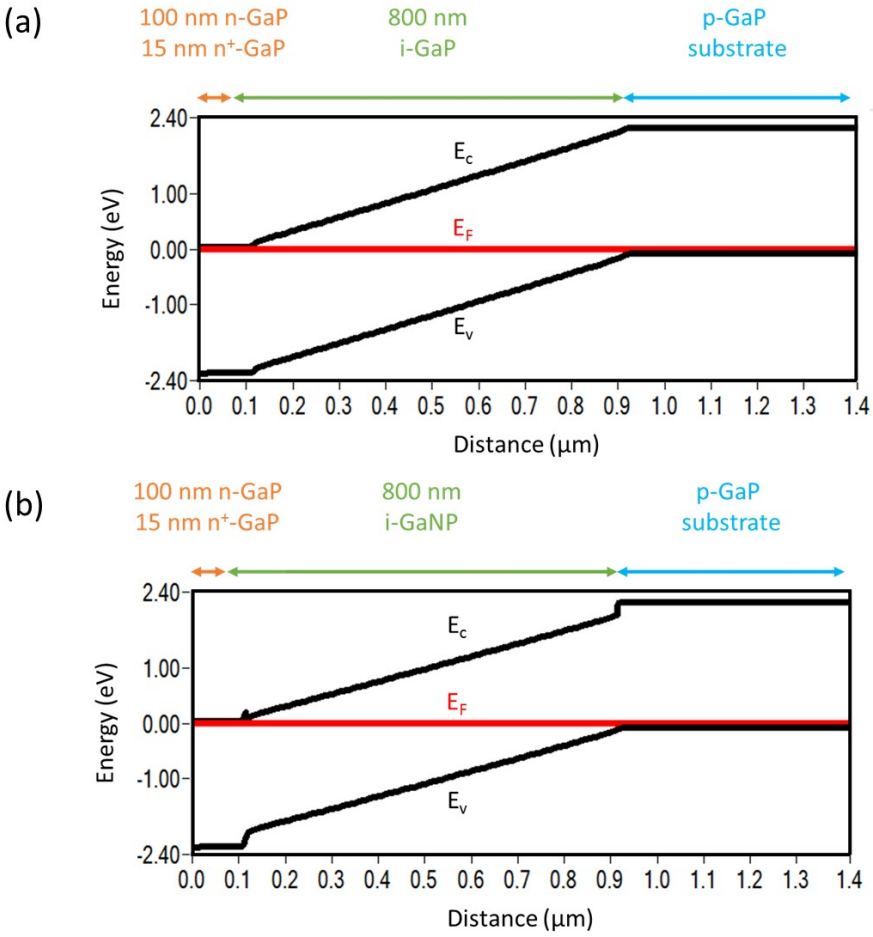


**Figure 4.2**: The band diagram of (a) GaP-800 and (b) GaNP-800.

the built-in electric field across the absorbing undoped region. This intrinsic layer also aids the short diffusion length of dilute nitride material.[44–46] The following n-type layer is divided into two sub-layers: first, a standard 100 nm thick n-GaP sub-layer doped with Si at $4\times10^{18}$ $cm^{-3}$ to act as the emitter, followed by a 15-nm-thick highly doped ($8\times10^{18}$ $cm^{-3}$) n-GaP sub-layer, denoted as $n^{+}$-GaP, to reduce series resistances from the inner portions of the cell to the metal contacts and to create a thin tunneling barrier for ohmic-like contacts. The $n^{+}$-GaP sub-layer is also kept very thin to minimize carrier loss by recombination due to its very short hole minority carrier diffusion length, which is below 190 nm.[21] No window layer is used for any of the samples discussed in this

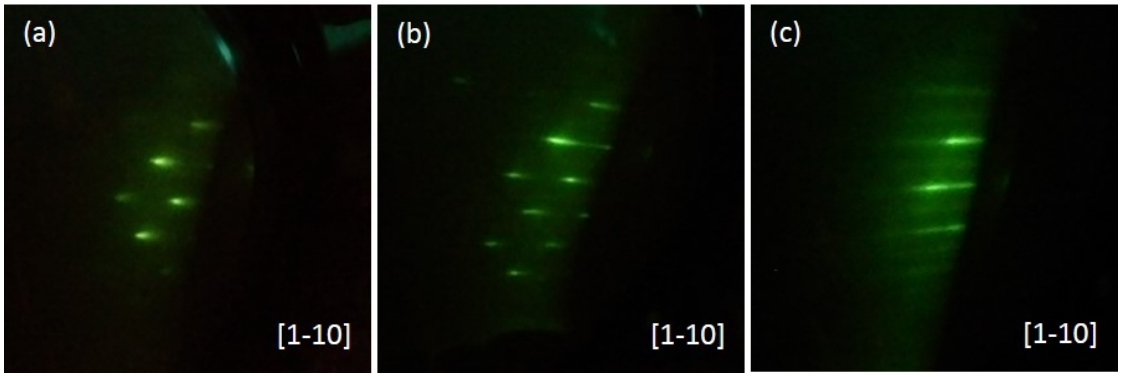


**Figure 4.3**: RHEED reconstruction patterns of device layers (a) after oxide desorption (b) during the growth of GaNP, and (c) after the growth of GaNP.

work.

## 4.3 Growth

All samples were grown on p-GaP (001) substrates in a Varian Gen-II molecular beam epitaxy (MBE) system modified to handle gas sources. Thermally cracked $PH_3$ at 1000°C and RF N plasma excited at 13.56 MHz were used for P and N sources, respectively. Solid elemental Ga was used to generate a Ga beam from an effusion cell. Solid Si was used as the n-type dopant. Prior to growth, native oxide was desorbed under $P_2$ overpressure at 600°C. The substrate temperature was then decreased to 570°C to grow the i-Ga(N)P layer followed by the n-GaP layer. A substrate temperature of 570°C was chosen because this is in the optimal growth temperature range to minimize N-related defects before phase separation in dilute nitride. During growth, reflection high energy electron diffraction (RHEED) measurements were used to monitor the surface morphology of the samples in situ. The surface reconstruction pattern after the growth of each layer showed a streaky 2x4 reconstruction, indicative of a smooth surface. As an example of RHEED pattern, Figure 4.3 shows the RHEED patterns in [1-10] or a 2x pattern (a) after oxide desorption but prior to growth, (b) during growth, and (c)

after the growth of GaNP. The chevron shaped diffraction pattern in (a) is indicative of rough surface conditions before growth. The spotty-steaky pattern in (b) indicates that the surface conditions were beginning to smooth. The surface conditions became very smooth in (c) as indicated by a steaky RHEED pattern. All layers were grown at 1 $\mu$m/h with V/III incorporation ratio $\sim$2.5, calibrated by Ga-induced RHEED intensity oscillation. The substrate was rotated at 5 RPM during growth to ensure uniformity.

## 4.4 Structural characterization

X-ray diffraction (XRD) was performed to determine the N concentration. An XRD 2$\theta$/$\omega$ line scans on the (115) and (004) plane is shown in Figure 4.4. According to XRD measurements, our GaNP samples have a N concentration of $\sim$1.8%.

GaNP with [N] = 1.8% has a lattice mismatch f = 0.31% with GaP. Using the energy balance model for misfit strain relaxation,[47] and assuming 60$^\circ$ mixed dislocations typical for zincblende materials, we estimate a GaNP critical thickness of $\sim$40 nm. This is well below the $\sim$1 $\mu$m optical absorption length in GaNP and below the thicknesses used in our cells. Therefore, full relaxation of misfit strain is expected in our structures. To characterize the structural integrity of the GaNP/GaP structures, we conducted detailed TEM characterization on all three sample structures as shown in Figure 4.5 and Figure 4.6. For the GaP-800 structure, an epitaxial defect-free interface was obtained, as expected (Figure 4.5(a)). All GaNP/GaP samples exhibited epitaxial, yet defective interfaces with misfit defects that were often found to have edge dislocation components in the cross-sectional cut plane. Figure 4.5(b) shows the GaNP-2000 structure with clearly visible defect contrast at the GaP/GaNP interface. Aside from the interface, the GaNP layer is a single crystalline layer, as obtained by extensive selective area diffraction (SAD) characterization and imaging in the <110> beam axis. Figure 4.5(c) shows a

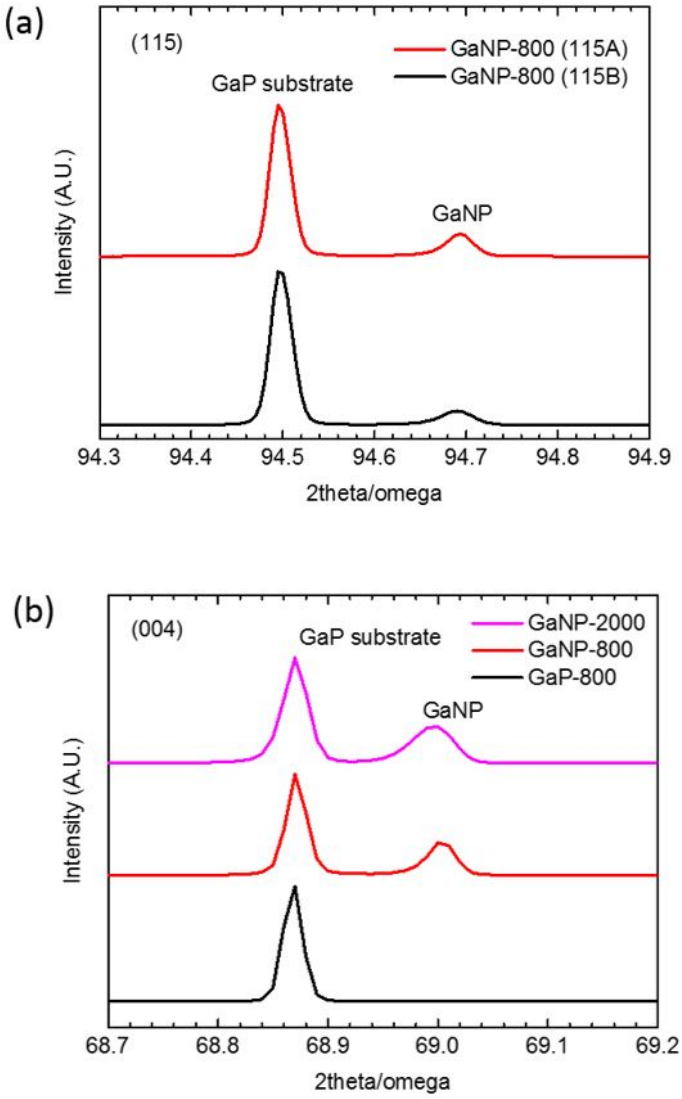


**Figure 4.4**: (a) XRD spectra showing two $\{115\}$ asymmetric peaks, labled as (115A) and (115B), peformed on GaNP-800. The GaNP peaks for both scans are shown at the same position, indicating a fully relaxed GaNP layer on GaP substrate for GaNP-800. According to this result, GaNP layer of GaNP-2000 can be assumed as a fully relaxed layer. With their fully relaxed GaNP layers together with (b) (004) symmetric XRD, we estimate that the GaNP layers have [N] of 1.8%.

representative high-resolution TEM (HRTEM) image at the center of the GaNP layer (area enclosed with a small red square in Figure 4.5(b)). Notably, we do not observe threading dislocations in the GaNP layers which is the key for enhanced power conversion efficiencies in our cells. The contrast of misfit dislocations at the GaNP/GaP interface was observed for multiple g-vector orientations in TEM.

## 4.5 Electrical results and discussion

J-V characterization was performed under dark and AM1.5G conditions. Figure 4.7 shows the J-V characteristics of GaP-800, GaNP-800, and GaNP-2000, respectively, and Table 4.1 lists key performance metrics extracted from the aforementioned graphs. We used the slope of the semi-log dark J-V curve to calculate the ideality factor (n-factor) of the devices. Despite series resistance effects that led to nonlinear slope of the J-V characteristics, we estimate n-factor = 1.8 for GaP-800 and $\geq 2$ for the GaNP cells. The n-factor of GaP-800 is similar to prior reported n-factor for GaP cells.[22] The higher n-factor of GaNP indicates that GaNP samples suffer higher Shockley-Read-Hall recombination in the depletion region when compared to GaP-800.[35] This likely results from the GaP/GaNP defective interface.

By examining the GaP-800 and GaNP-800 samples in Figure 4.7(b) and Table 4.1, the GaNP-800 sample exhibits a slightly lower fill factor (FF) as expected. This is due to its higher n-factor value. The lower FF in the GaNP-800 sample is more than compensated by a significant increase in $J_{sc}$ and a slight increase in $V_{oc}$. This results in a net efficiency of approximately twice that of GaP-800. However, because the bandgap of GaP-800 and GaNP-800 are not the same, a portion of the GaNP-800 $J_{sc}$ can be attributed to its lower bandgap. To more accurately compare GaP-800 to GaNP-800, we define

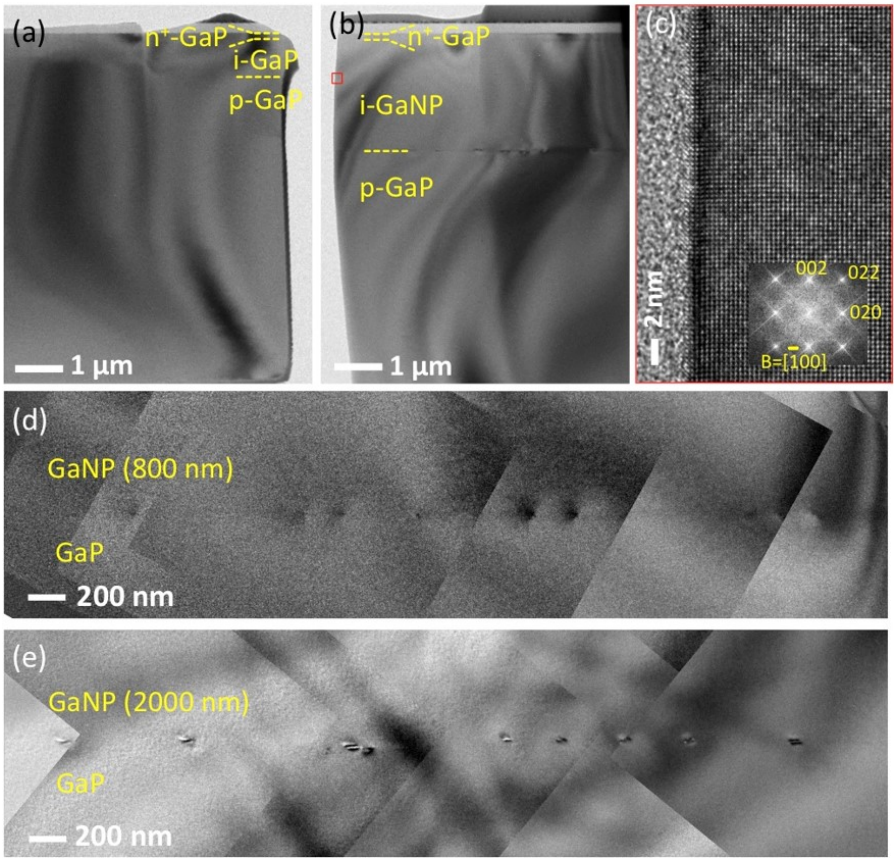


**Figure 4.5**: TEM images along the [001] zone axis with a g=[020] beam condition showing (a) defect free GaP-800 and (b) GaNP-2000 with misfit defects at the GaP/-GaNP interface. (c) High resolution TEM (HRTEM) showing the crystalline i-GaNP layer in the region enclosed by the red square in (b). (d)-(e) Merged relatively high magnification TEM images at the GaP/GaNP interfaces showing the defect density of GaNP-800 and GaNP-2000, respectively.

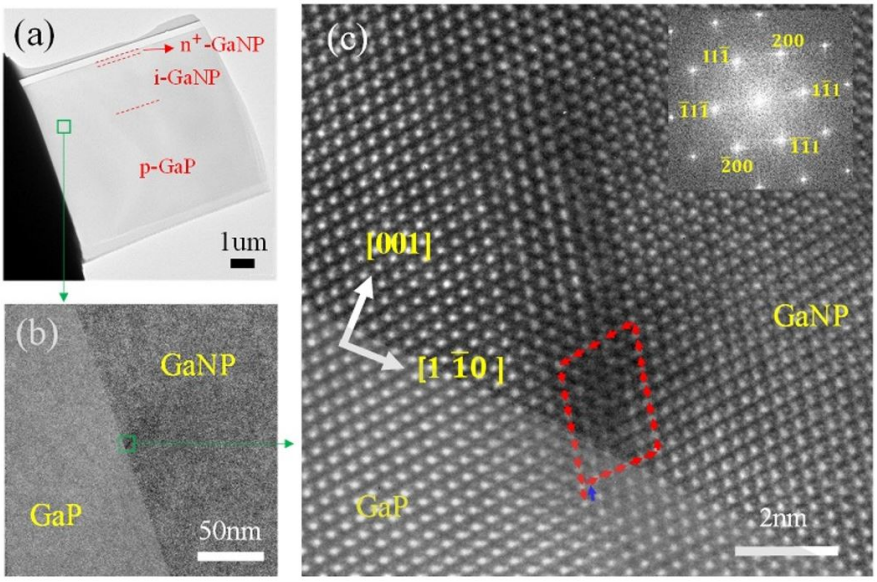


**Figure 4.6**: TEM images of a typical misfit dislocation. (a) An Overview TEM image of the GaNP-2000 cell, (b) Low magnification TEM image of a misfit dislocation, (c) HRTEM image with a Burgers circuit completed around one misfit dislocation at the GaP/GaNP interface indicating a projected a/3<111> Burgers vector.

the $J_{sc}$-ratio, listed in Table 4.1, as the measured $J_{sc}$ over the maximum possible $J_{sc}$ calculated by assuming EQE equal to 1 for all energies above the bandgap. By using this method, the $J_{sc}$-ratio of GaNP-800 is $\sim$1.4x higher in comparison to the $J_{sc}$-ratio of GaP-800. This clearly indicates that adding N has a large impact on improving $J_{sc}$ and, ultimately, solar efficiency. Consequently, we conclude that the interface defects seen in TEM observations do not have a significant adverse effect on the solar cell efficiency of the GaNP-800 sample.

Having established GaNP as a better material than GaP for solar cell applications, we now investigate the effect of intrinsic layer thickness on solar cell performance. Examining GaNP-800 and GaNP-2000 in Figure 4.7(b), $J_{sc}$ increases with thickness, as expected, due to the longer light absorption length of the thicker samples and results in slightly elevated $V_{oc}$. With the $J_{sc}$ and $V_{oc}$ observations combined, the overall solar efficiency of GaNP increases as thickness increases. Furthermore, our work shows that

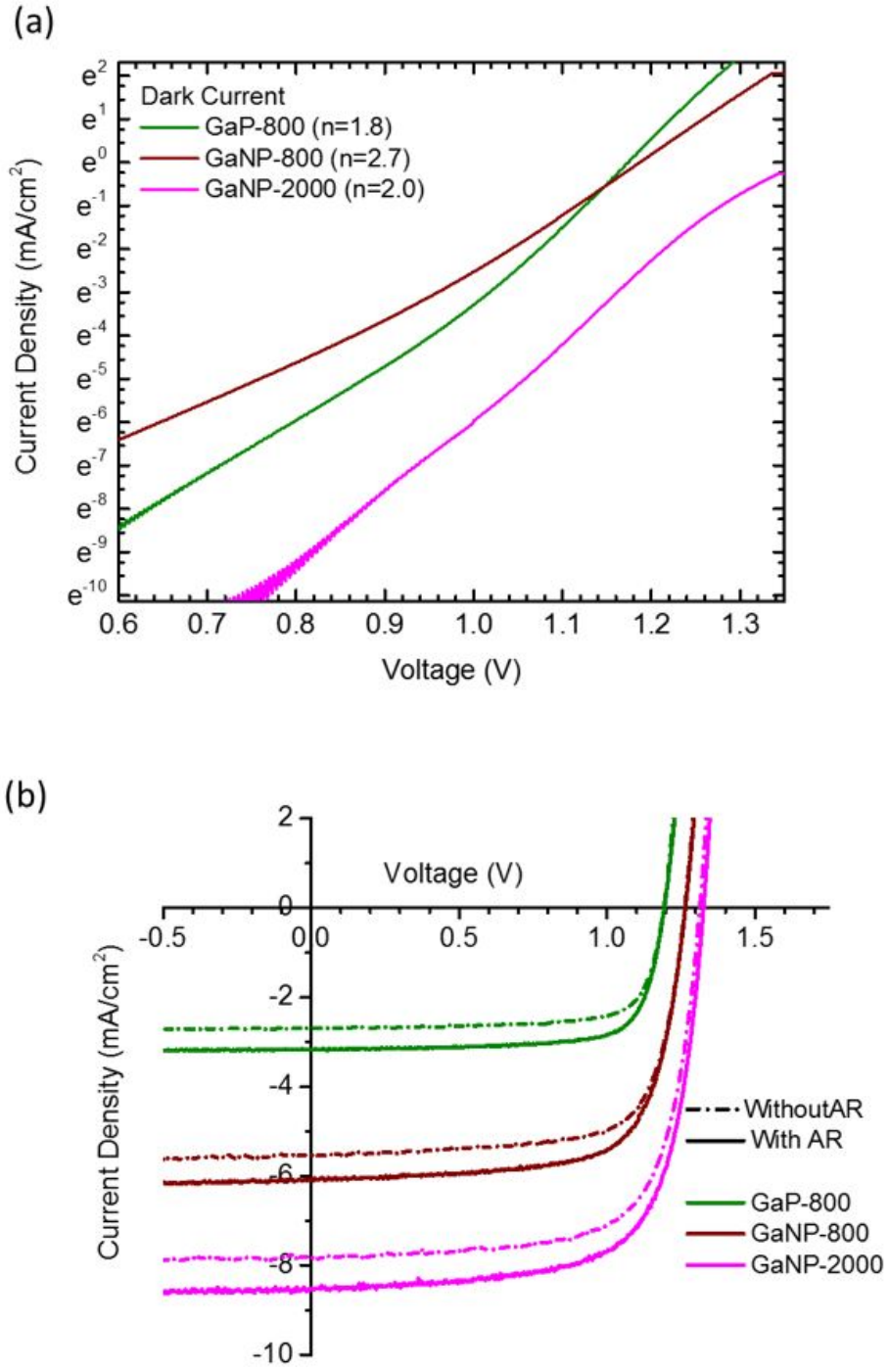


**Figure 4.7**: J-V characteristics of GaP-800, GaNP-800, and GaNP-2000 under (a) dark condition and (b) AM 1.5G condition with and without AR coating.

**Table 4.1**: Performance parameters of GaP-800, GaNP-800, and GaNP-2000 with and without AR coating.

| | sample | $J_{sc}$ (mA/cm$^2$) | $V_{oc}$ (V) | $J_{sc}$-ratio (%) | FF (%) | η (%) | n-factor |
|---|---|---|---|---|---|---|---|
| Without AR | GaP-800 | 2.69 | 1.19 | 30 | 77 | 2.5 | 1.8 |
| | GaNP-800 | 5.52 | 1.26 | 42 | 73 | 5.1 | 2.7 |
| | GaNP-2000 | 7.80 | 1.31 | 60 | 71 | 7.3 | 2.0 |
| With AR | GaP-800 | 3.17 | 1.19 | 35 | 76 | 2.9 | - |
| | GaNP-800 | 6.08 | 1.26 | 46 | 71 | 5.5 | - |
| | GaNP-2000 | 8.53 | 1.33 | 65 | 69 | 7.9 | - |

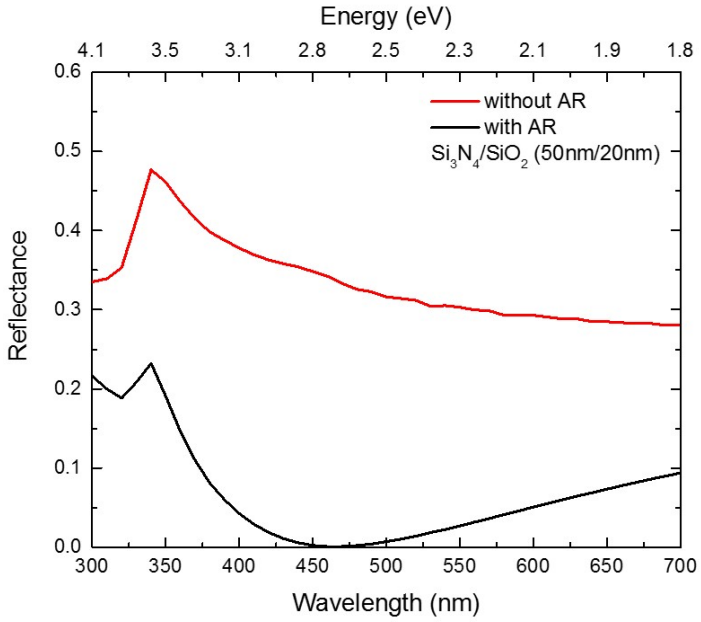


**Figure 4.8**: The calculated reflectance of GaP with/without the double layer AR coating, which consists of $Si_3N_4$ (40 nm) and $SiO_2$ (20 nm), as a function of wavelength.

efficiency is not yet limited by minority carrier diffusion length. Thus, this trend may continue beyond the maximum thickness, 2000 nm in GaNP-2000, studied in this work.

In addition to studying the impact of intrinsic layer thickness on solar efficiency,

we also investigated the impact of surface reflection reduction on solar performance. To do so, we added a $Si_3N_4/SiO_2$ double-layer anti-reflection (AR) coating on the surface of each device. The AR layers were deposited by plasma-enhanced chemical vapor deposition (PECVD) with a thickness of 50 nm and 20 nm, respectively. The thicknesses of the layers were calculated to have a low reflectance, $< 5\%$, across wavelengths in the range of 400 nm - 600 nm as shown Figure 4.8. Figure 4.7(b) shows the J-V characteristics of each device with and without an AR coating. The AR coatings enhance $J_{sc}$ but have very little effect on $V_{oc}$. Accordingly, AR coatings increase overall solar efficiency for all devices studied. Combining all techniques mentioned thus far, our best solar cell, GaNP-2000, produces an efficiency of 7.9%.

## 4.6 Optical results and discussion

To closely probe each material's solar cell performance, EQE measurements were performed. EQE is the ratio of the number of carriers collected by a solar cell to the number of incident photons at a given energy; thereby accounting for both light absorption and recombination losses. Figure 4.9 shows the measured 300 nm - 700 nm EQE spectra for GaP-800, GaNP-800, and GaNP-2000. In Figure 4.9(a), the absorption edges of GaP-800 and GaNP-800 are $\sim$540 nm and $\sim$615 nm, respectively. This agrees with the GaP bandgap (2.26 eV) and GaNP bandgap (2.05 eV). Of particular note, GaNP-800 exhibits two EQE peaks. The short wavelength peak in the range of $\sim$350 nm to $\sim$450 nm is comparable to the peak of GaP-800 in the same region. We suggest that this characteristic is driven by the n- and p-type GaP layers of GaNP-800 cell structure (Figure 4.1). It follows, then, that the long wavelength peak in the range of$\sim$450 nm to $\sim$615 nm can be attributed to the GaNP layer and its lower bandgap. Additionally, the absorption edge of GaNP-800 increases more sharply than that of GaP-800 due to the direct bandgap

of GaNP. This considerable advantage has a direct effect on solar efficiency within the wavelengths of interest. This is clearly reflected in the improved $J_{sc}$-ratios listed in Table 4.1. Finally, with respect to the effects of AR coatings on solar efficiency, while overall solar efficiency is increased as expected, we observed degradation of performance at shorter wavelengths. This is possibly due to the AR coating absorbing light in the shorter wavelengths, especially given that $Si_3N_4$ has a bandgap of 2.4 - 4.7 eV.

Examining the EQE of the GaNP devices (Figure 4.9(b)), we observe increased EQE at all wavelengths as the thickness is increased. With regard to our highest efficiency solar cell, GaNP-2000 with AR coating, its EQE is larger than 0.80 in the range of $\sim$450 nm to $\sim$560 nm and reaches its maximum value of 0.95 at 530 nm. This confirms that the photocurrent is not yet limited by the minority carrier diffusion length in the i-GaNP and p-GaP layers. In addition, high EQE at long wavelengths indicates little to no effect from rear surface recombination. With respect to front surface conditions, the EQE of all devices slowly decreases at short wavelength. This is indicative of poor surface conditions. This can be improved by (1) increasing the diffusion length in the emitter region (e.g., optimizing growth conditions), (2) optimizing the emitter thickness, and (3) reducing the front surface recombination velocity (e.g., passivating the front surface, implementing a window layer). Such improvements should be the focus of future work.

## 4.7 Comparison to other solar cells

In this work, we also compare our results against the current most efficient GaP solar cell, henceforth denoted ME-GaP, which was reported to have a solar efficiency of 2.90%[20] (ME-$GaP_W$) and 2.42%[21] (ME-$GaP_{NW}$) with and without a window layer, respectively. Since none of our devices implemented a window layer, we performed comparisons against ME-$GaP_{NW}$. ME-$GaP_{NW}$ consists of an 8 $\mu$m thick p-type GaP base

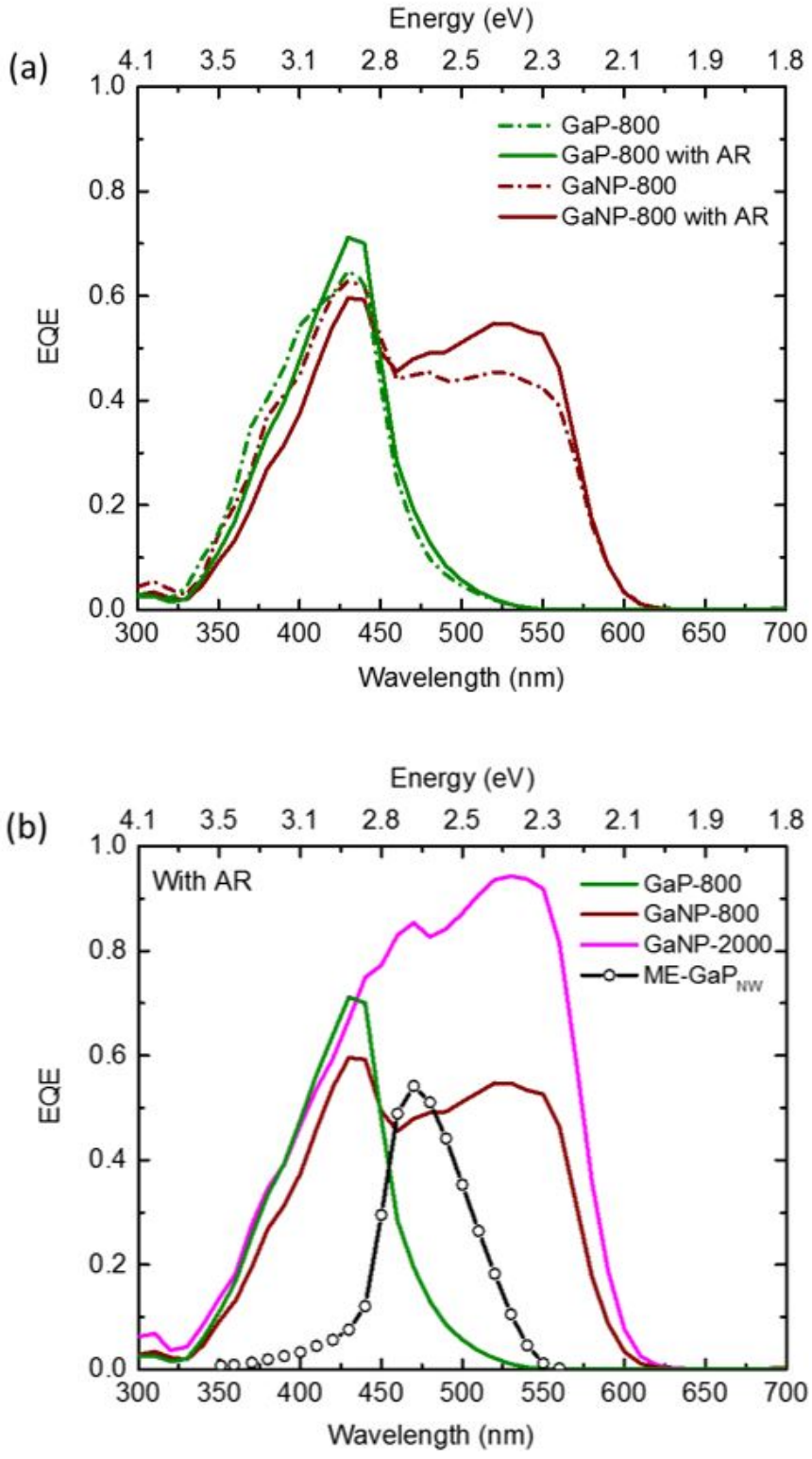


**Figure 4.9**: (a) EQE measurements with and without an AR coating of GaP-800 and GaNP-800 (b) EQE measurements with an AR coating of GaP-800, GaNP-800, GaNP-2000, and ME-GaP$_{NW}$.

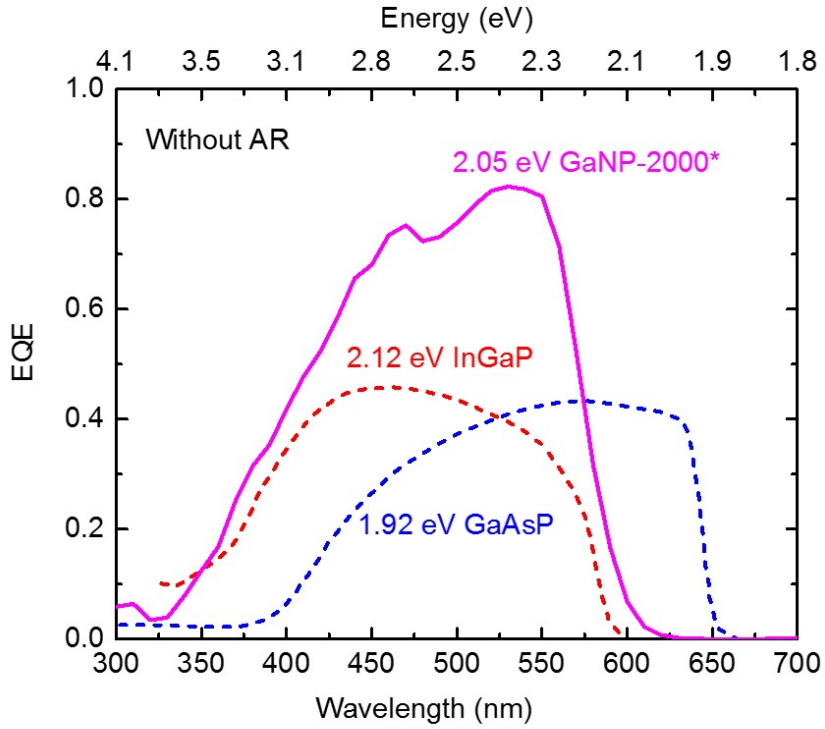


**Figure 4.10**: Comparison of EQE measurements between our best GaNP solar cells and InGaP and GaAsP solar cells, which have similar direct bandgap.

layer and a 0.8 $\mu$m thick n-type GaP emitter layer.

For GaP-800 and ME-GaP$_{NW}$, both absorption edges, depicted in Figure 4.9(b), begin at $\sim$550 nm due to their identical GaP material. The EQE of ME-GaP$_{NW}$ then increases much faster than that of GaP-800 at the long wavelength range of $\sim$460 to $\sim$550 nm. This can be attributed to it being a much thicker device. However, utilization of a thinner emitter layer (shorter than the hole minority diffusion length) in GaP-800 results in significant gains in short wavelength EQE when compared to ME-GaP$_{NW}$. Comparing our most efficient sample, GaNP-2000, to ME-GaP$_{NW}$, GaNP-2000 exhibits considerably improved EQE performance across all wavelengths.

In addition, to date, our GaNP solar cells exhibit higher efficiency than other wide direct-bandgap solar cells grown on GaP substrate, illustrated in Figure 4.10. InGaP (2.12 eV) and GaAsP (1.92 eV) solar cells with active layer thicknesses of $\sim$ 2 $\mu$m achieve

efficiencies of only 3.89%[48] and 4.8%,[49] respectively; the low efficiencies partly result from their lattice mismatch, which requires the growth of defective metamorphic buffer layers.

## 4.8 Conclusions

In summary, these are some highlights of our materials and devices studies. First, in the materials studies, the dilute nitride GaNP layers were grown by gas-source molecular beam epitaxy with [N]$\sim$1.8% (2.05 eV), which is closely lattice-mated to Si. TEM shows epitaxial layers that have no observable defects under HRTEM in the volume of the GaNP layer above the interface. Most of the lattice-mismatch appears to stem from misfit dislocations in the plane of the GaNP/GaP interface. This is a significant observation because any threading dislocations in the volume of the GaNP layer would reduce the minority carrier lifetime. Second, the interface defects have some impact on ideality factor and resulted in slightly lower FF, compared to GaP. Third, the reduction in FF was more than fully offset by the higher light absorption in the direct bandgap GaNP. This resulted in significantly increased solar efficiency as compared with pure GaP. Finally, we conclude that we have not yet reached the optimal thickness of GaNP for solar cell applications. Thus far in our studies, thicker GaNP layers exhibited significantly higher EQE across all wavelengths. However, we have not yet observed the solar conversion efficiency be limited by the minority carrier diffusion length, even for our thickest sample, GaNP-2000. It is likely that further increases in the layer thickness will provide additional gains in solar efficiency until the minority carrier diffusion length is exceeded. A more in-depth study of the effect of layer thickness on solar cell efficiency is required. Overall, we conclude that GaNP solar cells provide a significant increase in efficiency over their GaP counterparts. Experimentally, the best GaNP solar cell studied

in this work delivers better efficiency (7.9%) than the most efficient indirect-bandgap GaP and direct-bandgap InGaP and GaAsP solar cells to date. These performance gains are expected to motivate further investigation into the integration of GaNP into future dual-junction solar cells on Si substrate.

## 4.9 Acknowledgments

This Chapter was partially published in **S. Sukrittanon***, R. Liu*, Y. G. Ro, J. L. Pan, K. L. Jungjohann, C. W. Tu, S. A. Dayeh, "Enhanced conversion efficiency in wide-bandgap GaNP solar cells", *Appl. Phys. Lett.*, 100, 053108 (2015). *Equal contribution. The work was supported by the National Science Foundation under grant no. DMR-1106369. The TEM work was performed at the Center for Integrated Nanotechnologies (CINT), U.S. Department of Energy, Office of Basic Energy Sciences User Facility at Los Alamos National Laboratory (Contract DE-AC52-06NA25396) and Sandia National Laboratories (Contract DE-AC04-94AL85000).

# Chapter 5

# GaP/GaNP Microwire Solar Cells

## 5.1 Overview

An array of radial-junction microwires has garnered much attention recently as an alternative to planar solar cells and as a means to enhance solar cell efficiency.[50,51] The array configuration and microwire geometry can be independently tuned to allow multiple passes of light through the microwire material resulting in enhanced light absorption over a wide range of wavelengths. Furthermore, the radial junction decouples the direction of light absorption and carrier collection. This provides a short minority-carrier collection path, the length of which is equal to the wire diameter, resulting in effective light collection. In addition, instead of nanowires, microwires possess the optimal diameter that is in the order of the minority-carrier diffusion length to obtain maximum solar cell efficiency.[52] In contrast to thin film, microwires also open up the market for light-weight, portable, and flexible solar cells.[53,54]

For the past decade, Si-based radial-junction solar cells have been intensively researched, and array morphologies have recently achieved an efficiency of $\sim$16.5%.[55] Multi-junction solar cells have been demonstrated to achieve higher efficiency than the

efficiency achievable with single-junction solar cells. Thus, integration of high-efficiency III-V semiconductors on Si is a very attractive approach to accomplish both low cost and highly efficient solar cells.[56,57] A simple exemplary configuration is a dual-junction solar cell that employs Si as the inner junction and 1.7 eV III-V semiconductor as the outer junction.[6,7]

In Chapter 4, we previously optimized and demonstrated ∼2.05 eV GaNP, which is nearly lattice-matched with Si, thin film solar cells on GaP (001) substrate. The GaNP thin film solar cells achieve a maximum efficiency of 7.3%, even in the absence of a window layer and an anti-reflection (AR) coating (7.9% with an AR coating). This GaNP solar cell's efficiency is higher than other wide-bandgap solar cells: 2.42% for an indirect- bandgap GaP (2.26 eV), 3.89% for direct-bandgap InGaP (2.12 eV), and 4.8% for direct-bandgap GaAsP (1.92 eV). Although there are few studies focused on the integration of III-V onto Si wires,[58–61] to the best of our knowledge, no similar studies have fabricated and discussed GaNP microwire solar cells to date.

This Chapter is devoted to demonstration of GaP/GaNP core/shell microwire solar cells on GaP (001) substrate, depicted in Figure 5.1(a). All microwire samples are p-i-n solar cells, for which the fabrication processes are described. Systematic studies have been performed over a series of microwire lengths (L = 6 $\mu$m, 8 $\mu$m, 10 $\mu$m), array period (P = 4 $\mu$m, 6 $\mu$m, 8 $\mu$m), and microwire sidewall morphology. The array periods of the microwires are shown in Figure 5.1(b-d) for P = 4 $\mu$m, 6 $\mu$m, 8 $\mu$m, respectively. The structural properties of the microwires are characterized using scanning electron microscopy (SEM) and transmission electron microscopy (TEM), and solar cell performance is determined using current density-voltage (J-V) and external quantum efficiency (EQE) measurements.

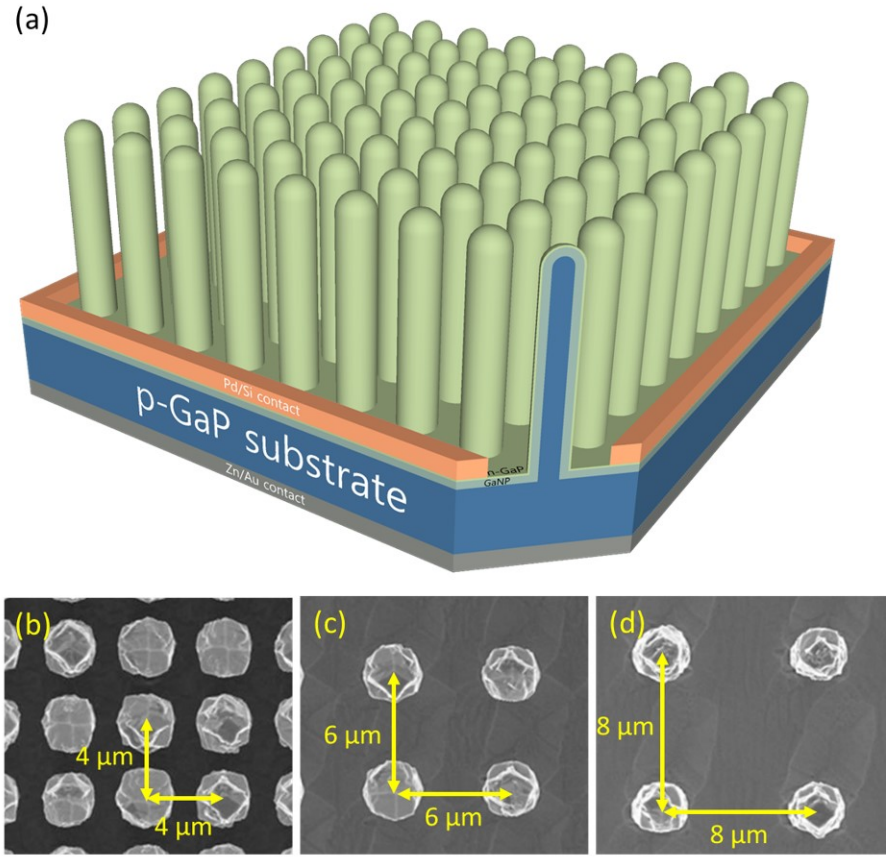


**Figure 5.1**: (a) Schematic of GaP/GaNP core/shell microwire solar cells in this work (b)-(d) SEM showing top-view of microwires with different array period: 4 $\mu$m, 6 $\mu$m, and 8 $\mu$m, respectively.

## 5.2 Device structure

All microwire samples are p-i-n solar cells that were fabricated by using a top-down dry etching technique to create p-GaP microwires, followed by using a step-mediated growth approach by gas-source molecular beam epitaxy (GSMBE) to grow the surrounding i-GaNP and n-GaP shells, respectively. The benefit of utilizing an RIE approach instead of MBE vapor-liquid-solid (VLS) growth for cores is that it does not suffer from twining planes which are commonly observed in III-V semiconductors grown by VLS.[62–64] However, using MBE growth is beneficial for shell growth because it provides the freedom to independently control the thickness, the material, and the doping

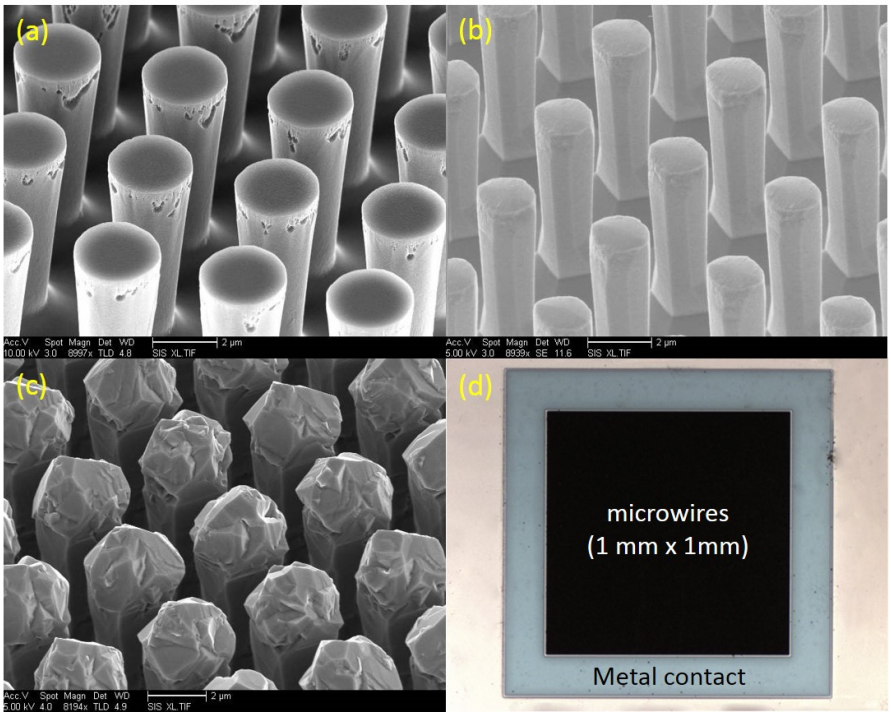


**Figure 5.2**: The fabrication process schematic of GaP/GaNP core/shell microwire solar cell, involving (a) RIE to create p-GaP cores, (b) wet etch to smooth the sidewalls of the microwires, and (c) i-GaNP and n-GaP shell growth by MBE. (d) SEM showing the dimension of the final device, which consists of microwire array (black) and the front contact (blue).

concentration of the shells.

Our p-i-n microwire structures are fabricated on highly doped p-type ($1.5 \times 10^{18}$ $cm^{-3}$) GaP (001) substrate to form microwire cores with minimal series resistance to the back contact. The GaP core diameter is approximately 2 $\mu$m, which is comparable to its minority diffusion length of the highly-doped GaP.[37] The next layer is a 500-nm-thick i-GaNP shell grown in MBE. GaNP is used to promote light absorption due to its direct bandgap, and an i-layer is employed to aid the short diffusion length of dilute nitride materials. The final layers are a 100-nm-thick n-GaP ($4 \times 10^{18}$ $cm^{-3}$) layer that acts as a standard emitter followed by a 15-nm-thick highly doped $n^{+}$-GaP ($8 \times 10^{18}$ $cm^{-3}$) to reduce series resistances from the inner portions of the cell to the metal contacts.

Figure 5.2 displays SEM images of the microwires at different steps of the

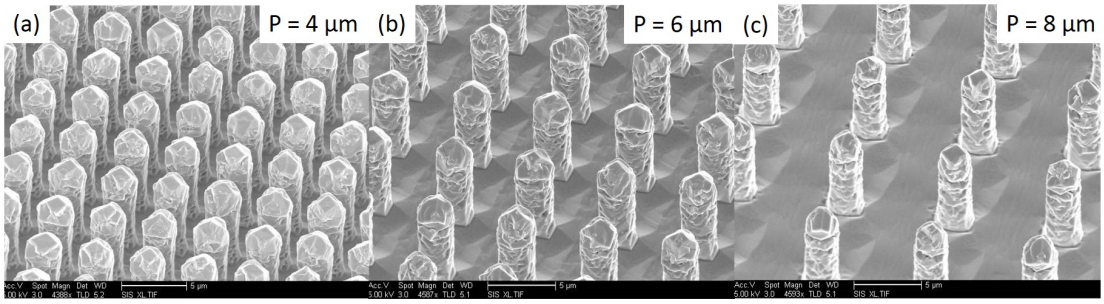


**Figure 5.3**: SEM images showing microwire arrays with length of 6 $\mu$m swept across array periods of (a) 4 $\mu$m, (b) 6 $\mu$m, and (c) 8 $\mu$m.

fabrication procedure that consists of (a) reactive-ion-etching (RIE) to obtain vertical microwires, (b) wet etch to mitigate the rough sidewalls, (c) shell growth in MBE, and (d) the final device of a microwire solar cell. The details of the fabrication are discussed in Chapter 6. The microwires after the shell growth exhibit the formation of sidewalls, shown in Figure 5.2(c), indicating anisotropic shell growth. The tips of the microwires feature facets with various orientations, which more likely stem from the facet tips after the wet etch process. Base on SEM observations of several shell growths, the growth rate of the shell roughly corresponds to half the growth rate on the planar layers.

## 5.3 The effect of array period and microwire length

We now focus on the geometrical effects on microwire solar cell performance for a fixed dot diameter of 2 $\mu$m. Figure 5.3(a-c) show 45° SEM images of arrays of microwires with length of 6 $\mu$m swept across array periods of 4 $\mu$m, 6 $\mu$m, 8 $\mu$m. J-V characteristics of these samples, depicted in Figure 5.4(a) and listed in Table 5.1, show an increase in short circuit current ($J_{sc}$) in microwires with tighter pitch (i.e. higher physical fill factor, PFF); the microwires with P = 4 $\mu$m exhibit a 16% higher $J_{sc}$ compared to those with P = 8 $\mu$m. It should be noted that $J_{sc}$ is generated by both the microwires and the underlying planar layer. These results are as expected since microwires exhibit

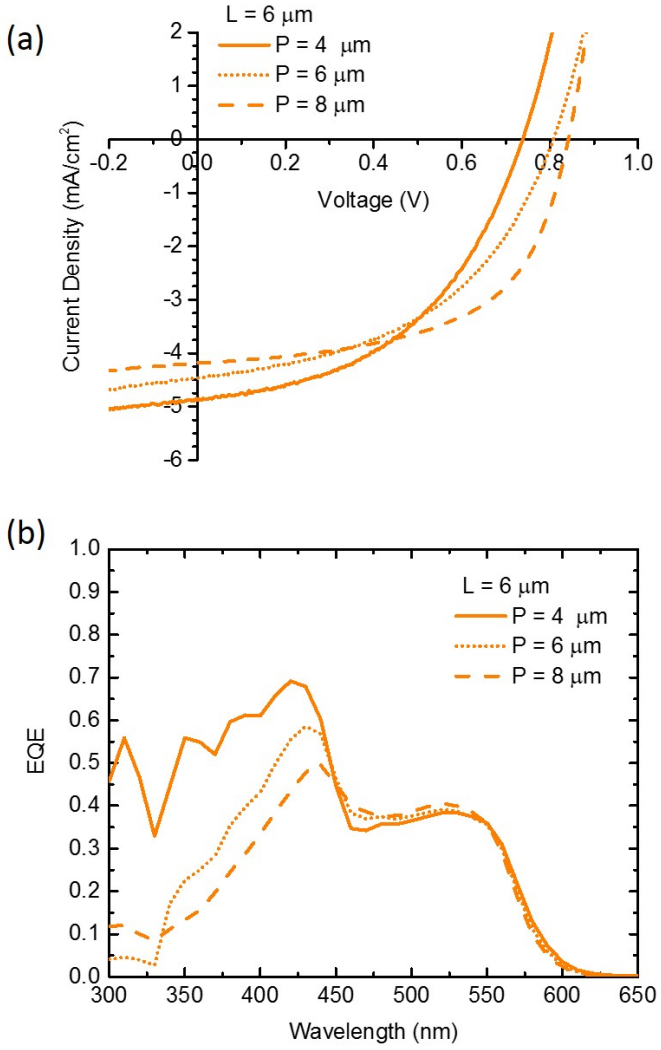


**Figure 5.4**: (a) J-V characteristics and (b) EQE of 6-$\mu$m-long microwire solar cells with different period arrays.

**Table 5.1**: The solar cell parameters from microwire solar cells with different lengths and array periods

| L ($\mu$m) | P ($\mu$m) | $J_{sc}$ (mA/cm$^2$) | $V_{oc}$ (V) | FF | $\eta$ (%) |
|---|---|---|---|---|---|
| 6 | 4 | 4.87 | 0.74 | 0.47 | 1.69 |
| | 6 | 4.46 | 0.81 | 0.47 | 1.70 |
| | 8 | 4.19 | 0.84 | 0.57 | 2.01 |
| 8 | 4 | 5.48 | 0.71 | 0.50 | 1.96 |
| | 6 | 4.65 | 0.74 | 0.51 | 1.75 |
| | 8 | 4.13 | 0.82 | 0.55 | 1.86 |
| 10 | 4 | 1.57 | 0.52 | 0.45 | 0.36 |
| | 6 | 4.85 | 0.78 | 0.52 | 1.95 |
| | 8 | 4.30 | 0.78 | 0.52 | 1.75 |

higher light absorption and more efficient carrier collection over thin films. In addition, it has been demonstrated theoretically and experimentally that the reflectance of the wires with facet tips is reduced when compared to planar surface or even wires with flat tips.[65] This increase of $J_{sc}$ with higher PFF is accomplished with a reduction of open-circuit voltage ($V_{oc}$).[60] This indicates that the gains of $J_{sc}$ with tight pitch are outweighed by an increase in recombination currents. The increased recombination current in tight pitch can result from a larger recombination at (1) the microwire outmost non-passivated surface, (2) defective GaP/GaNP interface, and (3) defective GaNP shells. The fill factor (FF) decreases with higher PFF for the same reasons.

To delve further into the physics of operation of our microwire cells, we performed EQE measurements on the different pitch samples in the wavelength range of 300 nm to 650 nm. The EQE spectra, shown in Figure 5.4(b), shows the absorption edges at $\sim$615 nm for all samples indicating that the GaNP shells possess a bandgap of $\sim$2.05 eV. All microwires exhibit two EQE peaks, which is similar to the behavior seen in Figure 4.9

for GaNP thin films. The short wavelength peak (∼350 nm to ∼450 nm) stems primarily from the GaP layer, while the long wavelength peak (∼450 nm to ∼615 nm) stems primarily from the GaNP layer. As PFF of the microwires increases, we observe that short wavelength EQE increases, yet there is no significant change in long wavelength EQE. This implies that the increase in short wavelength EQE is the main contributor in the enhancement of $J_{sc}$. This could result from better short-wavelength absorption in the microwires compared to the underlying planar layers. It should be noted that short wavelength light is primarily absorbed in the highly-doped emitter layer. The thin film emitter (∼230 nm), from MBE growth, is two times thicker than the microwire emitter (∼115 nm). This thin film emitter, which is thicker than the hole-minority diffusion length (∼190 nm[21]), results in high recombination and degraded short-wavelength EQE. As a result, the thinner emitter layer of the microwires provide significant gains in short wavelength EQE compared to the underlying thin films. Higher short-wavelength EQE at higher PFF also implies that surface recombination, which is primarily related to short wavelength performance, do not exhibit a major negative impact on microwire $J_{sc}$. This observation suggests that surface recombination is not a major factor in the $V_{oc}$ degradation discussed earlier.

In order to understand the effect of length on solar cell performance, we also fabricated and studied longer microwires. Microwire pattern and period were kept the same and only length was varied as L = 8 $\mu$m and L = 10 $\mu$m. The resulting J-V characteristics and EQE spectra are depicted in Figure 5.5. For L = 8 $\mu$m, J-V characteristics show that $J_{sc}$ increases and $V_{oc}$ decreases with microwire array density, and the EQE results show that $J_{sc}$ is sensitive to short wavelengths. Both observations are in line with the L = 6 $\mu$m sample. This trend continues for L = 10 $\mu$m with the exception of the P = 4 $\mu$m sample. The P = 4 $\mu$m sample exhibits much lower $J_{sc}$ and $V_{oc}$ compared to other microwires in this study, and we attribute this to MBE shadow effect, which

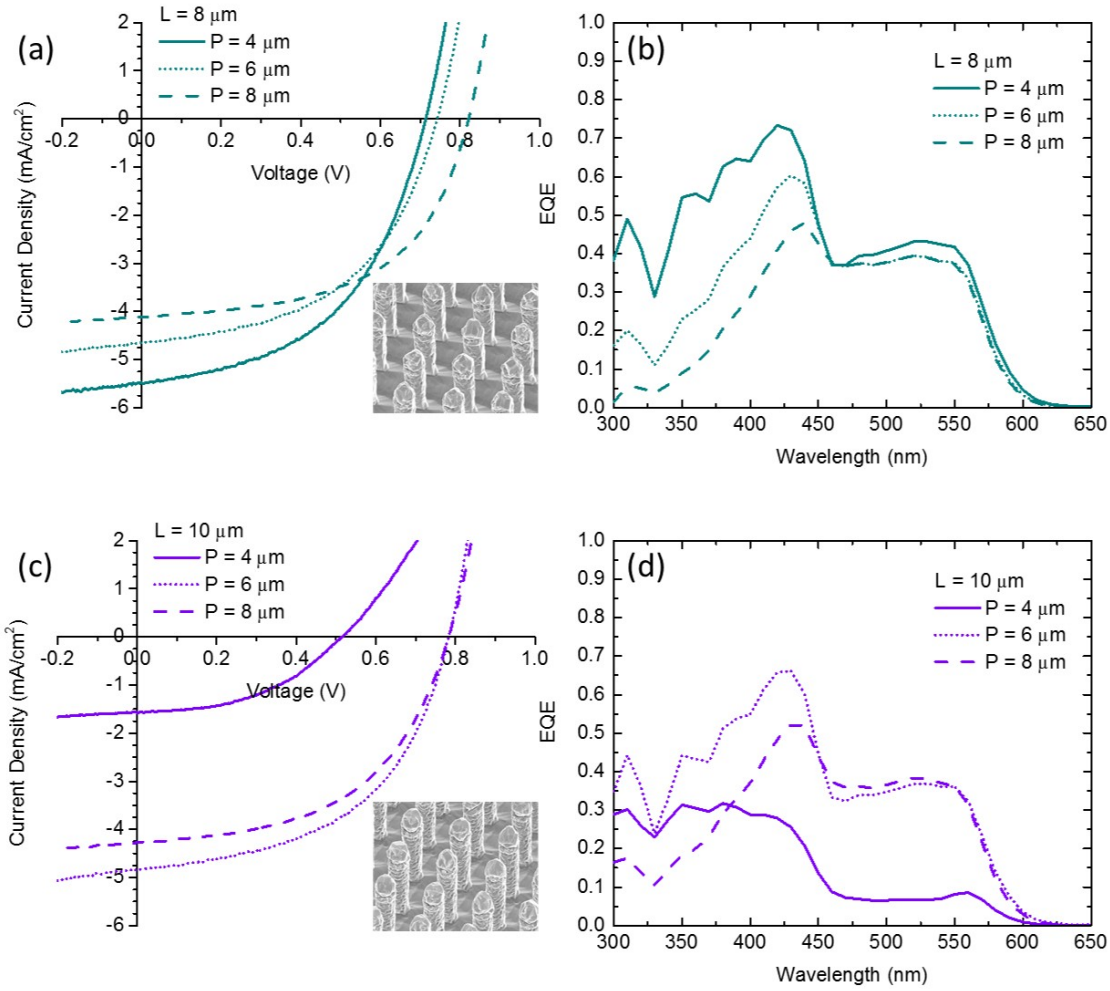


**Figure 5.5**: J-V characteristics and EQE of microwire solar cells with different period arrays for (a),(b) 8-$\mu$m-long microwire solar cells, and (c),(d) 10-$\mu$m-long microwire solar cells.

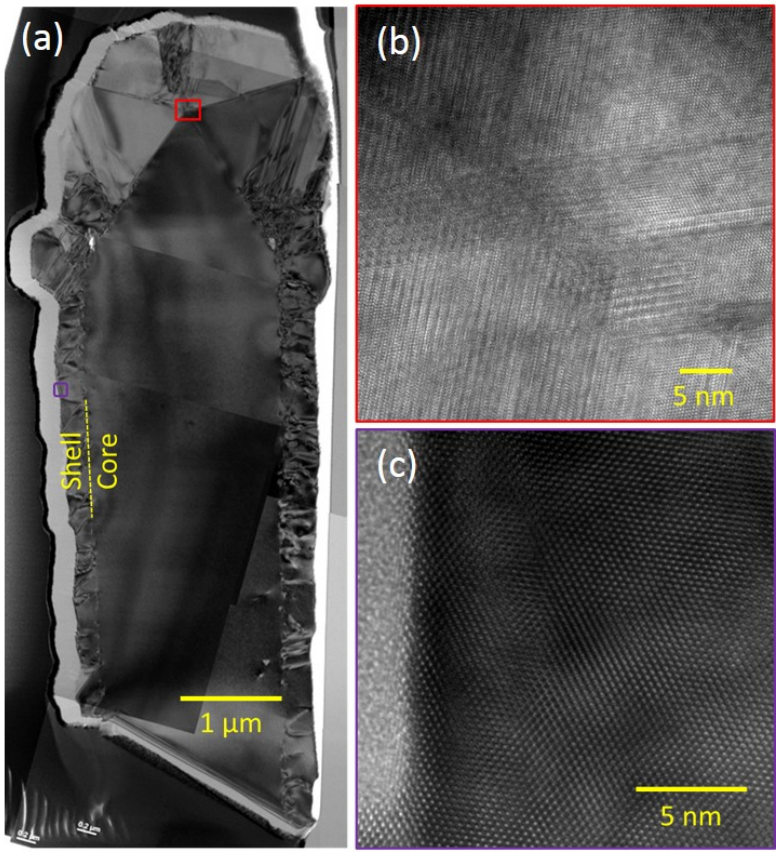


**Figure 5.6**: TEM image along the [110] zone axis with a g = [1-11] beam condition showing (a) low magnification bright field image of the microwire with L = 6 $\mu$m and P = 6 $\mu$m, (b) HRTEM image of the tip area (red square), and (c) HRTEM image of the non-defective sidewall (purple square).

is exacerbated by the length of the microwire. Excluding this result, we also observe that for a fixed period, $J_{sc}$ increases as microwire length increases.[59] This effect is more pronounced in higher PFF, which is as expected.

To investigate the crystal quality of the microwire solar cell, TEM measurement was perform along [110] zone axis on the 6-$\mu$m-long microwire with P = 6 $\mu$m, as an example. From TEM image, shown in Figure 5.6(a), it is observed the microwire possesses a large number of misfit defects at the GaP/GaNP interface, which also contribute to a large number of threading dislocations in the shell layers. We strongly believe that these defects are the main cause of $V_{oc}$ degradation in the microwire solar cells with

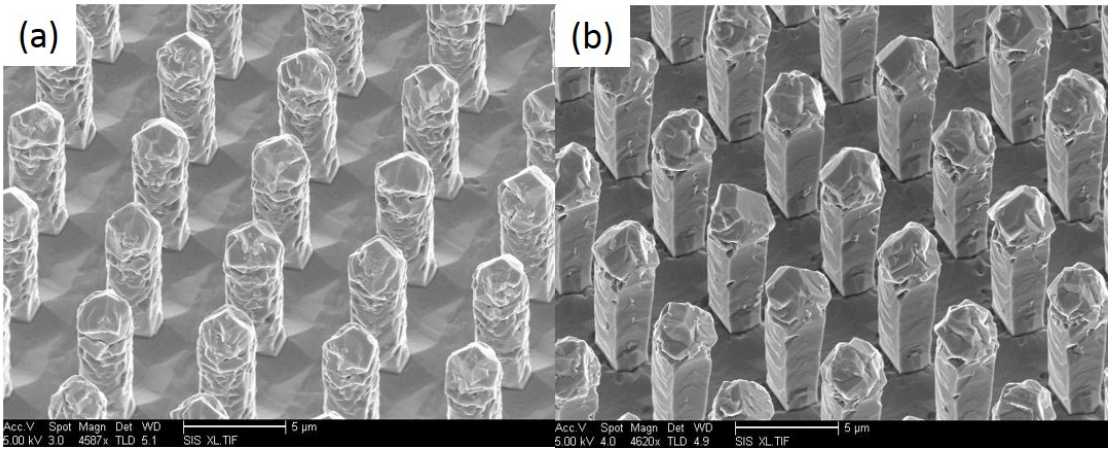


**Figure 5.7**: SEM showing 6-$\mu$m-long microwires (P = 6 $\mu$m) with (a) rough sidewalls, and (b) smooth sidewalls.

high PFF. The density of interface defects in the microwire is greater than what is seen in our previous work of GaP/GaNP thin film. This implies that the number of defects at the GaP/GaNP interface of the microwire is not only a result from GaP/GaNP lattice mismatch, but a result from the surface roughness of the core prior to shell growth. While wet etch smoothening can help to mitigate the issue, we were unable to completely eliminate the introduction of interface defects resulting from the sidewall roughness in our experiment. TEM image also shows the facet tips aligning in multiple orientations. The intersection of tip facets (red square) are shown in high-resolution TEM, as seen in Figure 5.6(b).

## 5.4 The effect of sidewall morphology

To decrease the number of aforementioned defects both at GaP/GaNP interface and in the shell, we repeated our previous experiment for L = 6 $\mu$m and P = 6 $\mu$m with the only difference being that we performed a slower wet etch to further smoothen the rough core sidewalls caused by RIE prior to shell growth. After shell growth, the resultant SEM image, Figure 5.7(b), shows smoother shell sidewalls which is likely to

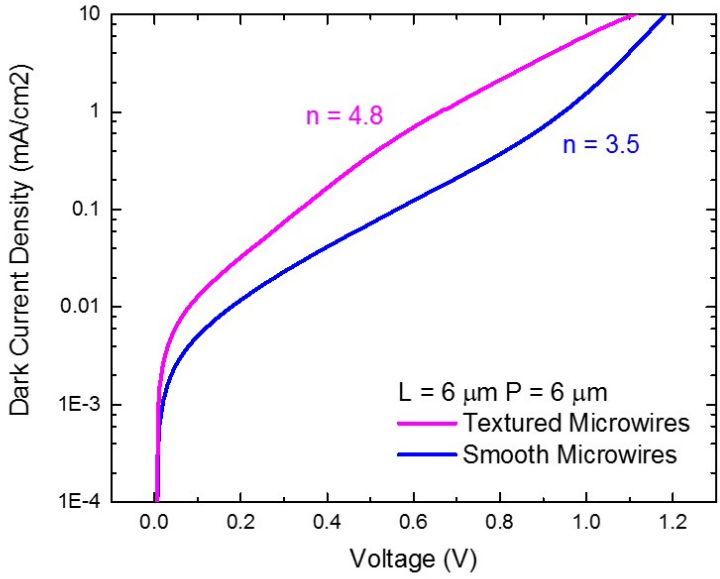


**Figure 5.8**: J-V characteristics of textured and smooth 6-$\mu$m-long microwires (P = 6 $\mu$m) under dark condition.

be less defective. To compare solar cell performance with different sidewall morphologies, J-V characteristics were performed under dark and AM 1.5G conditions on this smooth microwire sample and compared against the measurements performed on the original (textured) microwire sample, which feature the same length and array period. Maximum ideality factors (n-factor) calculated from the slope of the semi-log dark J-V curve, depicted in Figure 5.8, are 3.5 and 4.8 for the smooth microwires and textured microwire, respectively. This higher n-factor in the textured microwires indicates that the textured microwires suffer higher Shockley-Read-Hall recombination in the depletion region,[35] which results in greater recombination current and consequently degrades the $V_{oc}$ performance.

According to J-V curves under light condition, the sample with smooth sidewalls exhibits significant improvement in $V_{oc}$ performance over the sample with textured sidewalls, as shown in Figure 5.9(a), and listed in Table 5.2. This is in line with the

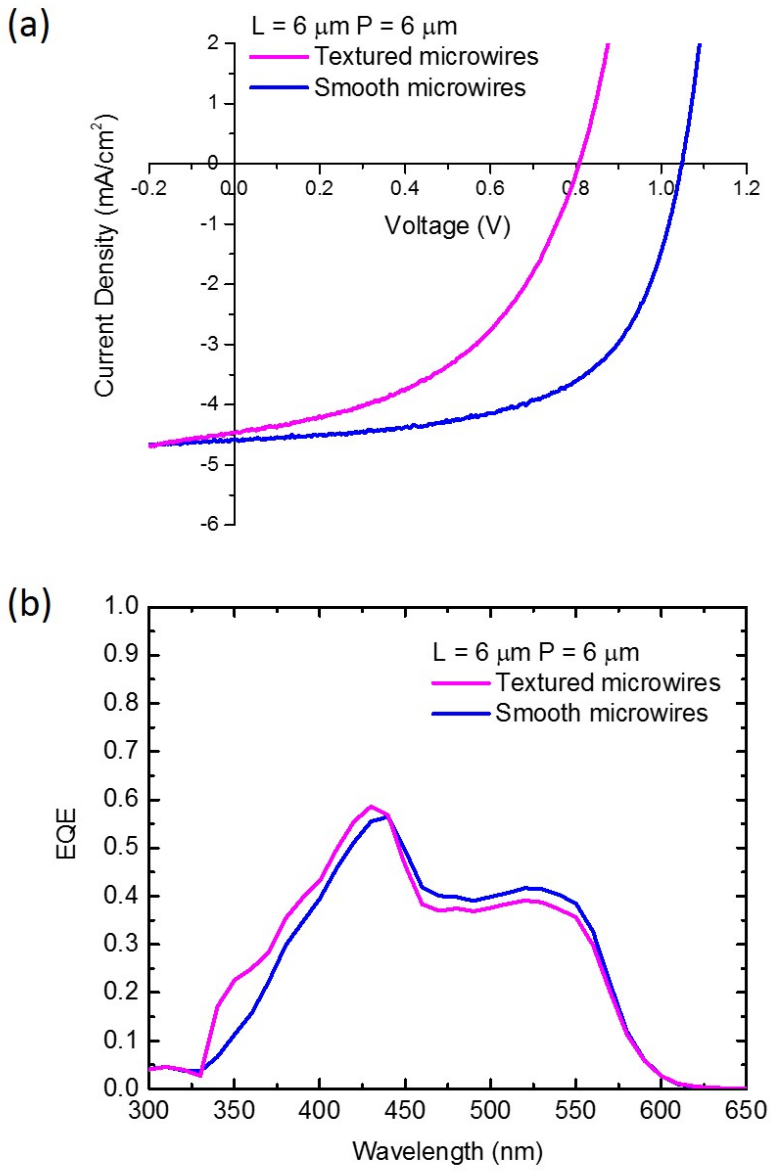


**Figure 5.9**: Comparison of (a) J-V characteristics and (b) EQE of 6-$\mu$m-long microwire (P = 6 $\mu$m) solar cells between the textured and the smooth microwire solar cells.

**Table 5.2**: The solar cell parameters from microwire solar cells (L = 6 $\mu$m and P = 6 $\mu$m) with different sidewall morphology, after AR coating and also the parameters from the thin film solar cell in the same growth run

| | $J_{sc}$ (mA/cm$^2$) | $V_{oc}$ (V) | FF | $\eta$ (%) | n-factor |
|---|---|---|---|---|---|
| Textured microwires | 4.46 | 0.81 | 0.47 | 1.7 | 4.8 |
| Smooth microwires | 4.57 | 1.05 | 0.60 | 2.9 | 3.5 |
| Smooth microwires with AR | 5.01 | 1.07 | 0.60 | 3.2 | - |
| Thin film | 4.17 | 1.36 | 0.77 | 4.4 | 1.8 |

results from the dark current. This is direct evidence to confirm that defects in the shell layer and interfacial defects have a major impact on the $V_{oc}$ performance in the microwire solar cells. FF is also improved with the smooth microwires as expected due to their lower n-factors. However, we note that sidewall morphology has no significant impact on $J_{sc}$, as no change of $J_{sc}$ was observed. The EQE results, as depicted in Figure 5.9(b), also show negligible change as a result of sidewall smoothening. It should be noted that textured sidewalls do provide the benefit of better light absorption due to good coupling of incident light,[59] but this benefit is offset by poorer minority carrier collection in these microwires resulting in no significant change in $J_{sc}$ performance between textured and smooth samples.

To confirm the lower number of defects in the microwires with smooth sidewalls, TEM along [110] zone axis was performed. Figure 5.10(a) shows that the smooth microwire possesses much fewer defects at the GaP/GaNP interface and also in the shell. The fewer defects result in lower recombination current. This result is in line with the aforementioned J-V characteristics. It should be noted that, these defects are still greater than the defects observed in thin film solar cell.

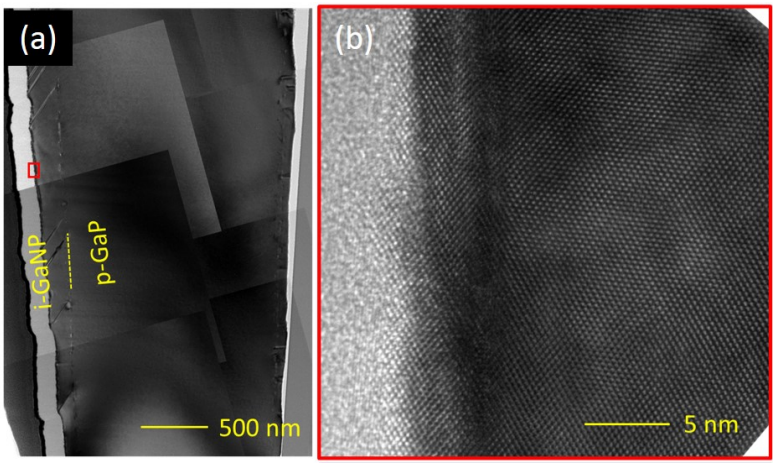


**Figure 5.10**: TEM image along the [110] zone axis with a g = [1-11] beam condition showing (a) bright field image of the smooth microwire with L = 6 $\mu$m and P = 6 $\mu$m, and (b) HRTEM image of the shell (red square).

## 5.5 Effect of anti-reflection coating

In addition to the above studies, we also investigated the impact of surface reflection on solar cell performance. A $TiO_2/Si_3N_4/SiO_2$ AR tri-layer was deposited on a smooth microwire sample with thicknesses of 33 nm, 52 nm, and 88 nm, respectively. The AR layers were deposited using sputtering for $TiO_2$ and plasma-enhanced chemical vapor deposition (PECVD) for $Si_3N_4$ and $SiO_2$. The calculated reflectance of these three AR layers are sub-5% for wavelengths between 400 nm and 1100 nm, as shown in Figure 5.11. Figure 5.12 shows the J-V characteristic and EQE of identical samples with and without the AR coating. The AR coating provides an appreciable improvement in $J_{sc}$ and a slight improvement in $V_{oc}$. The EQE result reveals that the increased $J_{sc}$ results from improved light response for short and medium wavelengths but not for long wavelengths near the band edge. From this, we infer that the long-wavelength EQE is not limited by the reflection of light but is, instead, limited by the i-GaNP thickness. It should be noted that the long-wavelength EQE (500 nm to 615 nm) corresponds to the absorption and carrier collection only in i-GaNP. GaP, which has larger bandgap, cannot absorb those

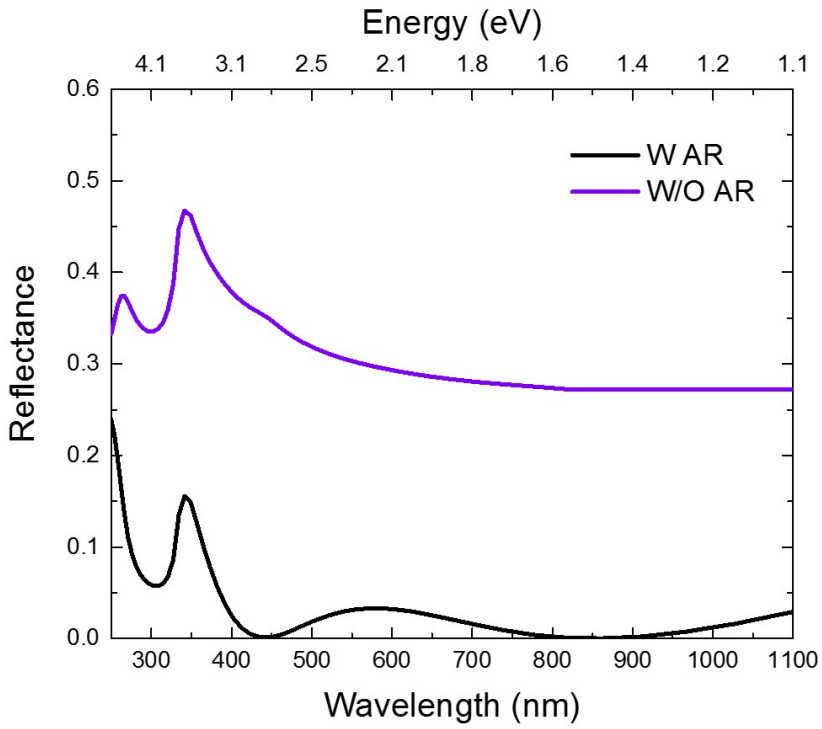


**Figure 5.11**: The calculated reflectance as a function of wavelength of GaP with/without the AR coating, which consists of $TiO_2$ (33 nm), $Si_3N_4$ (52 nm), and $SiO_2$ (88 nm).

long-wavelength photons. Thus far, our best microwire sample achieves an efficiency of 3.2% with $J_{sc}$ = 5.01 mA/cm$^2$, $V_{oc}$ = 1.07 V, and FF = 0.60.

## 5.6 Conclusions

In conclusion, we have successfully fabricated GaP/GaNP core/shell microwires utilizing a novel technique: top-down dry etching to create the cores and MBE to create the shells. The following are some highlights of our results. First, for a fixed length, $J_{sc}$ increases with increasing PFF. This improvement in $J_{sc}$ stems primarily from better response in short-wavelength light. Second, for a fixed array period, $J_{sc}$ increases as microwire length increases. Third, the degradation of $V_{oc}$ in our microwire sample is caused primarily by defects at the GaP/GaNP interface and in the shells. Surface

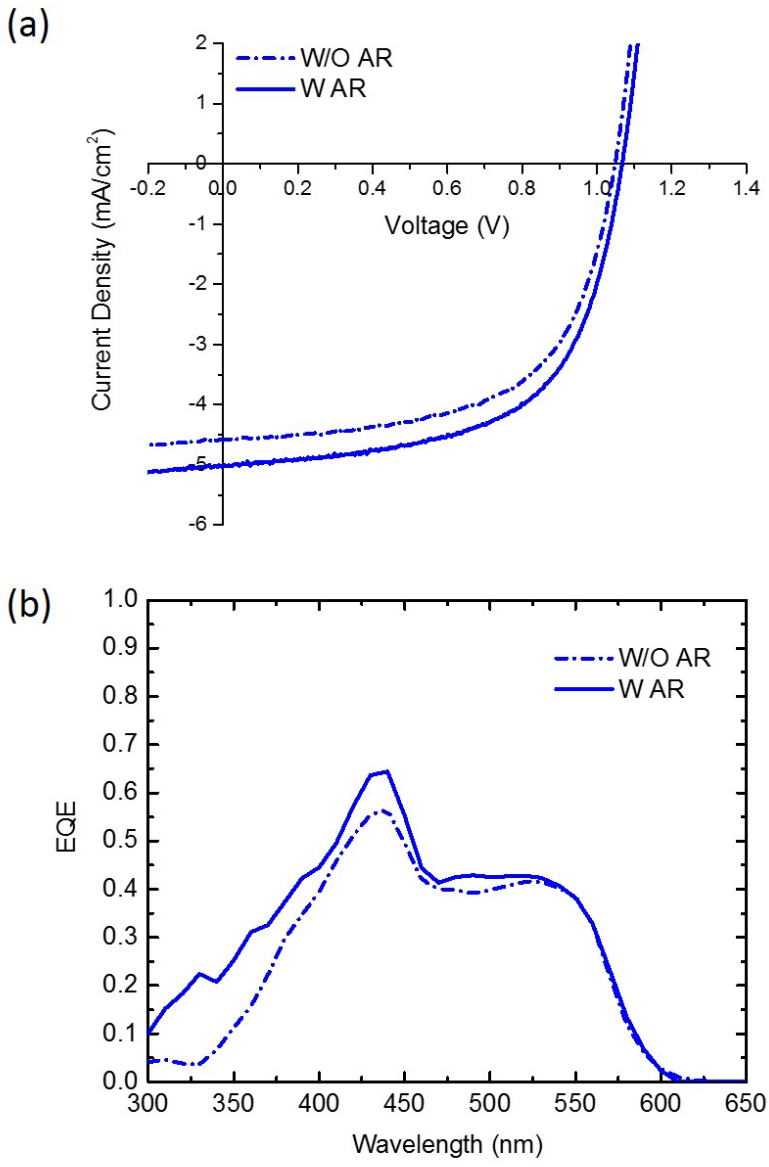


**Figure 5.12**: (a) J-V characteristics showing the improvement of $J_{sc}$ on the microwire solar cell (L = 6 $\mu$m and P = 6 $\mu$m) after AR coating and (b) their corresponding EQE.

recombination does not show a substantial negative impact on microwire performance in our experiment. Finally, our best efficiency from microwire solar cell is 3.2% with smooth sidewalls and AR coating. Compared to the thin film solar cell in the same growth run, the parameters for which are listed in Table 5.2, our best microwire solar cell exhibits greater $J_{sc}$ but poorer $V_{oc}$. This results from larger light absorption but greater number of defects in the microwire structure. For future work, optimization of core fabrication and shell growth process must be studied with the goal of minimizing defects. We believe that mitigating defects will enable our microwire solar cell to surpass thin films in term of efficiency.

## 5.7 Acknowledgements

This Chapter was partially in the preparation material for the publication. The work was supported by the National Science Foundation under grant no. DMR-1106369, No. DMR-1503595, and No. ECCS-1351980. The TEM work was performed at the Center for Integrated Nanotechnologies (CINT), U.S. Department of Energy, Office of Basic Energy Sciences User Facility at Los Alamos National Laboratory (Contract DE-AC52-06NA25396) and Sandia National Laboratories (Contract DE-AC04-94AL85000).

# Chapter 6

# The Fabrication of GaP/GaNP Core/Shell Microwire

Chapter 6 is devoted to the description of the fabrication optimization of GaP/-GaNP core/shell microwires reported in this work including the process to create metal array patterns, the reactive ion etching (RIE) process to create vertical microwires, and the wet etch technique to smooth the rough sidewalls and the MBE shell layer.

Figure 6.1 illustrates the microwire fabrication procedure. Processing begins with a p-type GaP ($1.3 \times 10^{18}$ cm$^{-2}$) substrate with dimensions of 0.5 cm $\times$ 0.5 cm to 1 cm $\times$ 1 cm, as shown in (a). An array pattern, illustrated in (b), is applied using photolithography technique, and Ni metal is subsequently deposited to create an etch mask, as seen in (c). In (d), the sample is RIE etched to create vertical microwires. Wet etch is then employed in (e) to smooth the rough sidewalls, which arise from the RIE etching procedure. Finally in (f), the shell layer is grow on the top of the existing microwire structure using MBE. The process equipment used in this report is described in Chapter 3.

Prior to all process steps, samples are ultrasonically cleaned in acetone, iso-

propanol (IPA), and deionized (DI) water in the given sequence to degrease the surface. Samples are then baked at 120 °C on a hotplate for 10 minutes to evaporate moisture.

## 6.1 Step 1: Fabrication of etch mask

The array pattern shown in Figure 6.1(b) is created by photolithograhpy using a Karl Suss Mask Aligner 6. The photomask used in this work has an opaque hole array, each 2 $\mu$m in diameter and with spacing of 4 $\mu$m and 6 $\mu$m. After the hole pattern is created, depicted in Figure 6.2(a), Ni metal is deposited onto the pattern, and subsequently the Ni metal outside the holes (i.e, on photoresist) is lifted off. The result is a Ni dot pattern, shown in Figure 6.2(b), that is then used as an etch mask. The detailed procedure is as follows:

1. Spin NR71-1500P negative photoresist onto samples at 4000 RPM for 40 s and acceleration of 500 RPM/s. The final film thickness is approximately 1.3 $\mu$m.
2. Hard-bake samples at 150 °C on a hotplate for 1 min.
3. Expose the photoresist for 16 s (176 mJ/cm$^2$ ) under UV light to create an array pattern.
4. Soft-bake samples at 100 °C on a hotplate for 2 min.
5. Develop the resist in a Resist Developer RD6 solution for 8 s.
6. Rinse in DI water and blow dry with $N_2$ gun.
7. Load samples into an e-beam evaporator chamber and immediately pump the chamber down to a base pressure of $2 \times 10^7$ Torr.
8. Deposit a 300-nm-thick Ni metal layer onto the samples. Gradually increasing the deposition rate from from 0.5 $\AA$/s to 1.5 $\AA$/s.

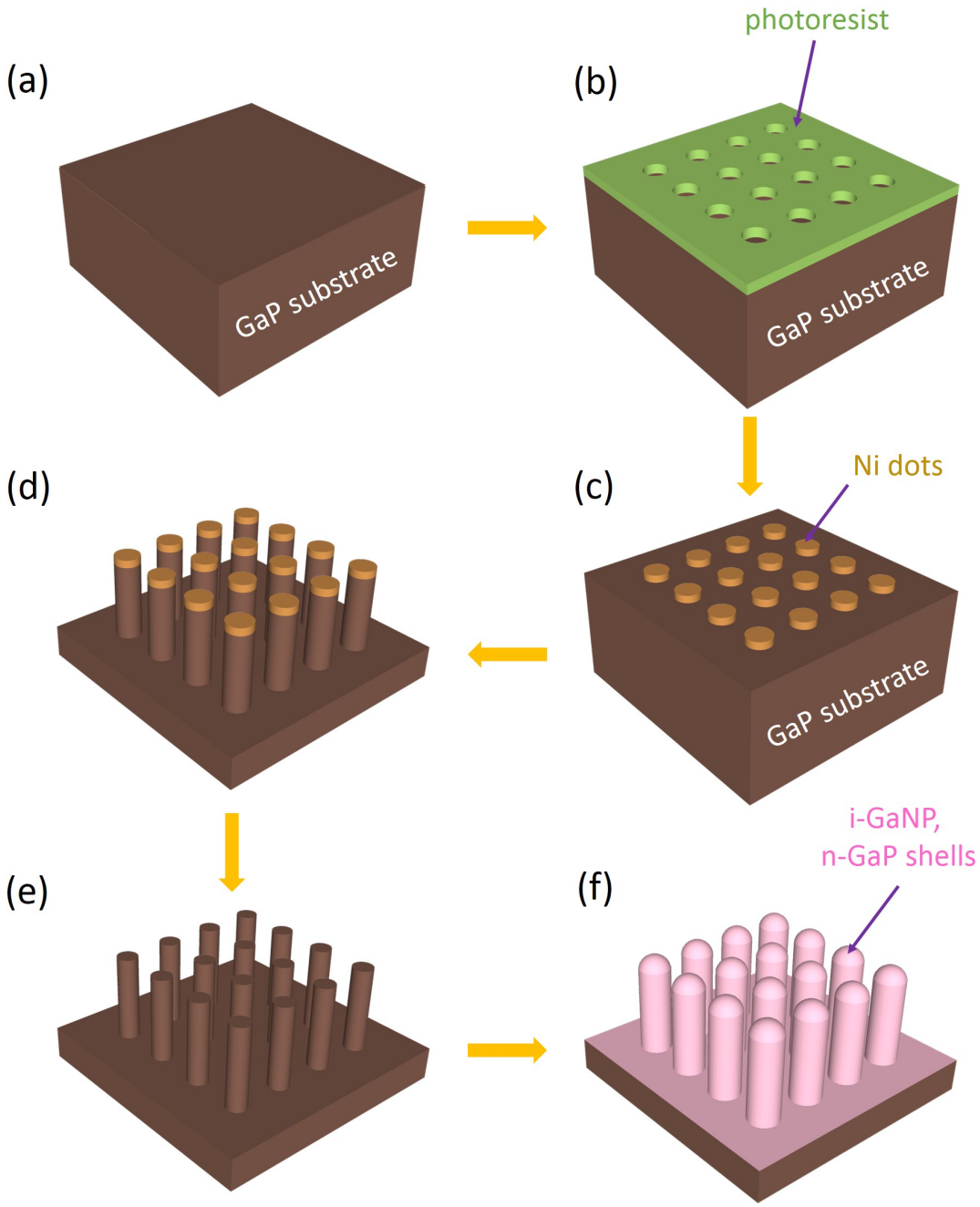


**Figure 6.1**: The fabrication steps of microwires: (a) a p-GaP substrate used for processing, (b) an array pattern from photolithography, (c) a Ni array as an etch mask, (d) a microwire array from RIE process, (e) a smooth-sidewall microwire array from wet etch, and (f) i-GaNP and n-GaP shells over the etched microwires using MBE.

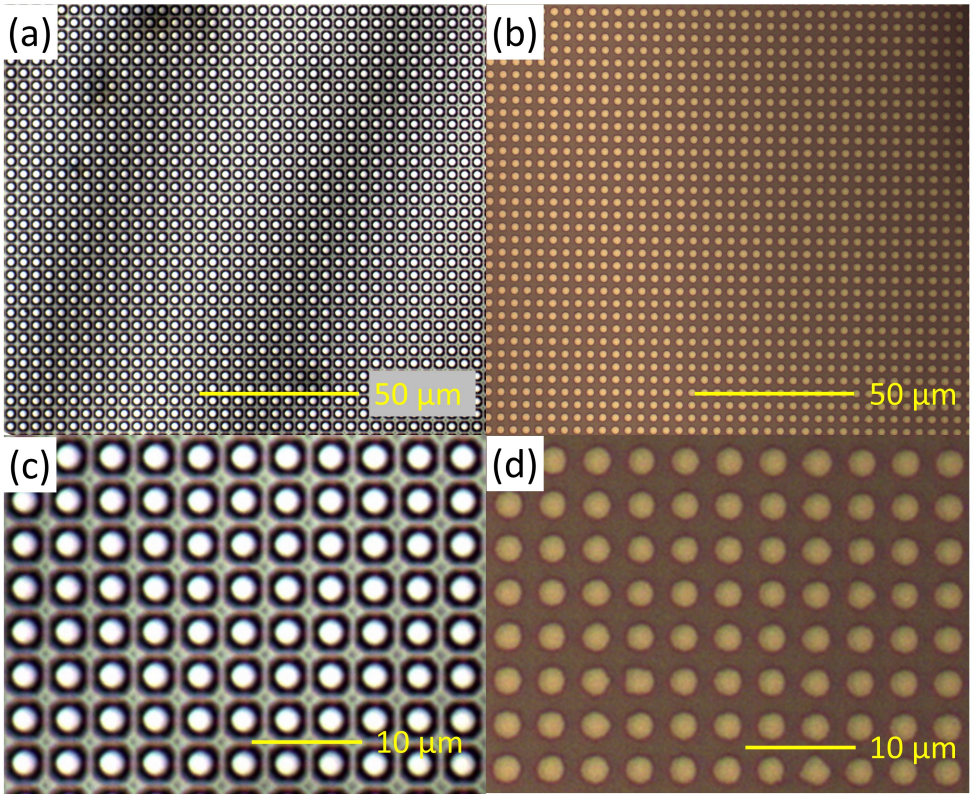


**Figure 6.2**: The opical microscope images showing (a) the patterned photoresist deployed by photolithography, (b) the Ni dot array used as an etch mask after lift-off process, (c) and (d) is a high resolution images of (a) and (b), respectively.

9. Lift-off the excess Ni by submerging the samples in Remover PG solution at 80 °C for approximately 3 hours or until the lift-off process is completed.

10. Rinse the wafer with acetone, IPA and DI water in sequence resulting in a completed circular Ni dot array that will be used in the dry etch step.

## 6.2 Step 2: Top-down dry etch process

A variety of chemistries are available to etch the GaP wafer.[66–68] The most common processes utilize $Cl_2$, $BCl_3$, or a combination of the two. Etching is achieved in two ways: (1) a chemical process in which $Cl_2$ and $BCl_3$ are excited and produce reactive

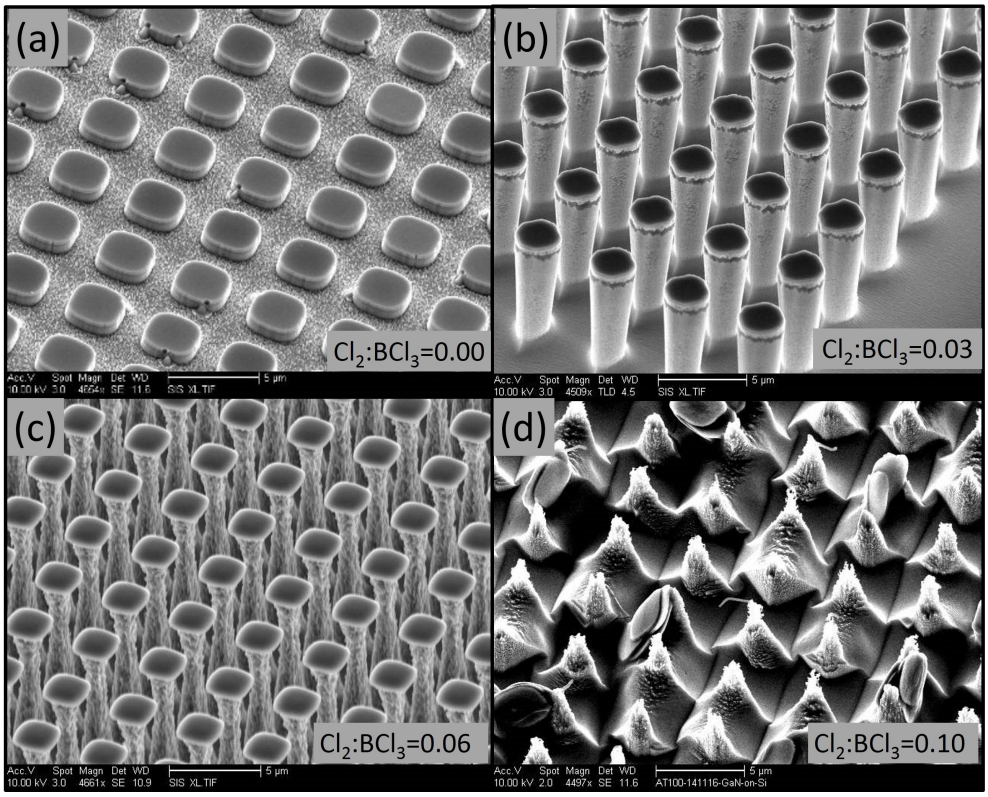


**Figure 6.3**: Optimization process of RIE with various ratios of $Cl_2$ to $BCl_3$ under a constant pressure and power of 36.5 mtorr and 200 W, respectively. All RIE is performed for 15 minutes.

Cl atoms, which react promptly on the GaP surface to form highly volatile $GaCl_3$; and (2) a physical process in which the surface of the sample is bombarded by ions that are also produced in plasma.[68] By controlling each process, we can control the resulting etch profile and surface morphology. A smooth isotropic under cut profile can be achieved by employing only the chemical process, and employing only the physical process results in a rough but vertical profile. In this work, a smooth vertical profile is desired so a combination of both processes is required.

In our experiment, the RIE etching process is performed in an Oxford Plasmalab 80 system equipped with a 13.56 MHz RF source at room temperature. The etching gases employed are $Cl_2$ and $BCl_3$. In working towards the optimal RIE etching conditions for our work, we first determined the best ratio of $Cl_2$ and $BCl_3$. Samples with the Ni mask

described in section 6.1, were etched using various ratios of $Cl_2$ and $BCl_3$ ($Cl_2/BCl_3$): 0.00, 0.03, 0.06, and 0.10. In all cases, RIE power, pressure, and the flow rate of $BCl_3$ were kept constant at 200 W, 36.5 mTorr, and 100 sccm, respectively. The resulting etch rate and etch profile are observed using scanning electron microscopy (SEM). Figure 6.3 shows 45° SEM images of the samples after RIE for 15 minutes under various gas mixture ratios. Among the conditions, faster etch rates are achieved by using greater $Cl_2/BCl_3$, but we also observed that employing greater $Cl_2$ and $BCl_3$ reduces anisotropic profile. This suggests that $Cl_2$ is the primary contributor to the chemical etch process whereas $BCl_3$ is the primary contributor to the physical etch process. In addition, $BCl_3$ was researched by other groups to be able to form a polymer that could passivate sidewalls thereby facilitating anisotropic etch.[69]

The approximate etch rate of the 0.00, 0.03, and 0.10 samples was calculated to be 70 nm/min, 490 nm/min, and 800 nm/min, respectively, and their 45 ° SEM images highlighting their etch profile and morphology are shown in Figure 6.4. For the images, the 0.00 condition results in a smooth anisotropic etch. However their etch rate are too slow for our microwire solar cells with the length of 6-10-$\mu$m. On the other hand, the 0.10 condition produces much faster etch rate, but the resulting microwires feature least anisotropic etch. Consequently, the 0.03 condition is selected as an optimal condition since it produces acceptable vertical etch profiles with a reasonable etch rate.

Similar to the $Cl_2/BCl_3$ ratio, RIE power was also swept in order to determine the optimal condition. In this experiment, RIE power was swept from 200 W to 300 W with pressure and $Cl_2/BCl_3$ held constant at 36.5 mTorr and 0.03, respectively. Figure 6.5 shows the resulting microwires after etching for (a) 200 W and (b) 300 W for 30 minutes. As expected, faster etch rates are achieved with greater RIE power but the resulting sample suffers from severe undercut as shown in 6.5b. Consequently, RIE power at 200 W is selected as the optimal condition.

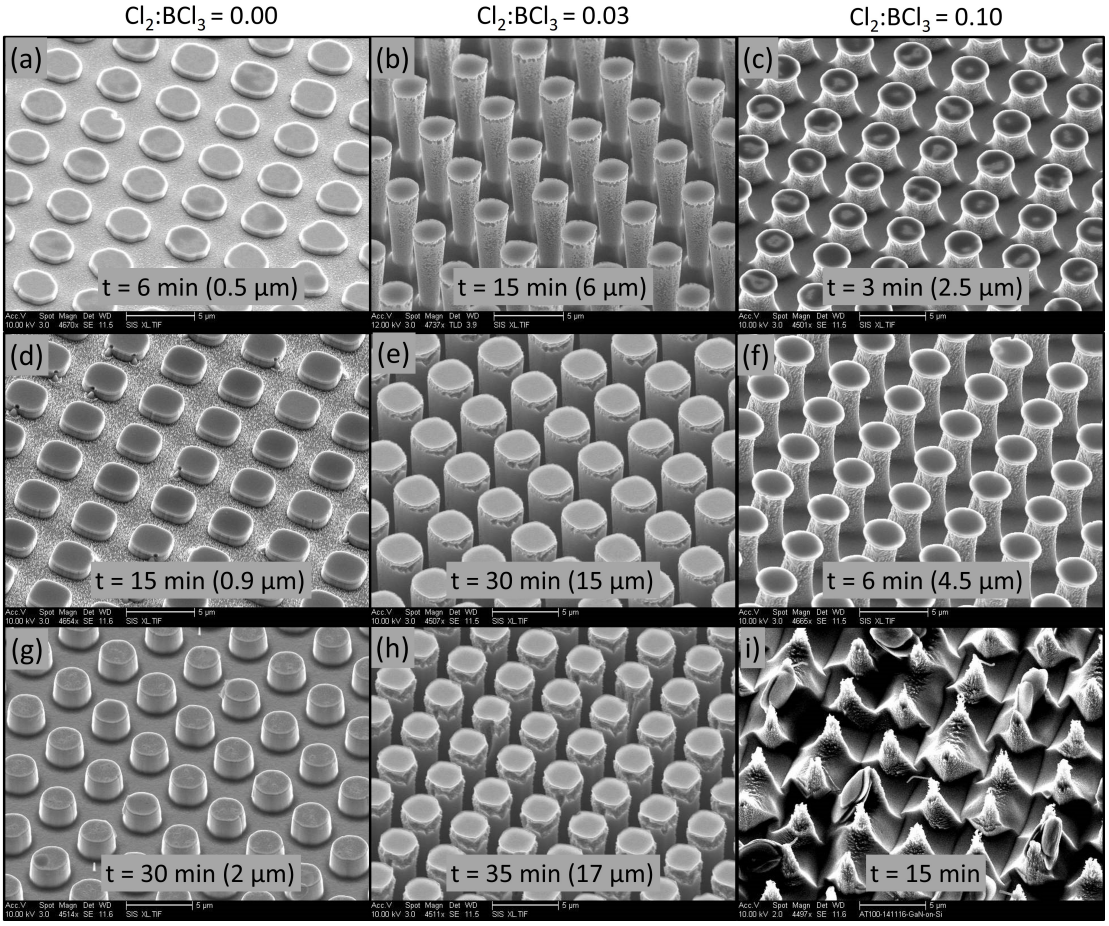


**Figure 6.4**: The 45 ° SEM images of the etch profile and their morphology of the etched samples under the $Cl_2/BCl_3$ of (a),(d),(g) 0.00, (b),(e),(h) 0.03, and (c),(f),(i) 0.10.

In summary, we experimentally determined the optimal RIE conditions for our work as RIE power of 200 W, and a $Cl_2/BCl_3$ ratio of 0.03 under the pressure of 36.5 mTorr. These conditions are used during microwire fabrication as well as during mesa etch. The detailed fabrication procedure is as follows:

1. Clean the etch chamber using $O_2$ plasma for 30 min.

2. Condition the chamber.

   (a) Pump the chamber down to $5 \times 10^{-5}$ Torr.

   (b) Inject 3 sccm of $Cl_2$ and 100 sccm of $BCl_3$ for 90 s while simultaneously

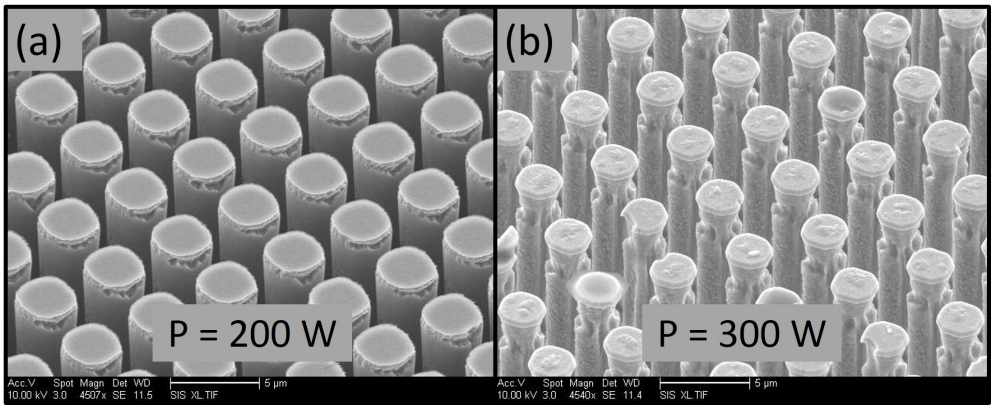


**Figure 6.5**: Comparison of the microwires using (a) 200 W and (b) 300 watt for 30 minutes under the identical pressure and the $Cl_2/BCl_3$ of 36.5 mTorr and 0.03, respectively.

adjusting chamber pressure to 36.5 mTorr.

(c) Light the plasma using an RIE power of 200 W.

(d) Wait 10 min.

(e) Stop RIE power and all gases.

(f) Clean the chamber by injecting Ar for 30 s and pumping down to $1 \times 10^{-4}$ Torr. Repeat 5 times.

3. Load samples with Ni patterned mask into the chamber.

4. Pump the chamber down to $5 \times 10^{-5}$ Torr.

5. Inject 3 sccm of $Cl_2$ and 100 sccm of $BCl_3$ for 90 s while simultaneously adjusting chamber pressure to 36.5 mTorr.

6. Light the plasma using an RIE power of 200 W.

7. Wait X min, where X depends on the target length (the etch rate for these conditions is $\sim$490 nm/min).

8. Stop RIE power and all gases.

9. Clean the chamber by injecting Ar for 30 s and pumping down to $1 \times 10^{-4}$ Torr. Repeat 5 times.

10. Pump the chamber down to $5 \times 10^{-5}$ and vent the chamber.

11. Take out the sample and dip it in Ni etchant TFB for 15 min to remove the Ni dots. This ensures the Ni dots are completely removed. Ni etchant TFB consists of nitric acid, potassium perfluoroalkyl sulfonate, and water.

12. Clean the sample with DI water and blow dry it with a $N_2$ gun.

13. The microwires are ready for the next step.

## 6.3 Step 3: Wet etch

The RIE etch performed in the previous step results in microwires with rough sidewalls. Wet etching aims to smoothen these sidewalls, which will promote better MBE shell growth. Standard wet chemical etching of GaP involves oxidizing the surface with an oxidizer and etching the oxide using various acids or bases. Our procedure uses $H_2O_2$ as an oxidizer and HCl is used to etch the oxide.[70]

In our experiment, the wet etch is performed using a HCl:$H_2O_2$:$H_2O$ = 1:1:1 solution at room temperature. To prepare the solution, 60 ml of HCl is added into 60 ml of DI water, followed by adding 60 ml of 30% $H_2O_2$. This condition provides an approximate etch rate of 20 nm/min. The samples are submerged in this solution for about 25 minutes to smooth the sidewalls, and then they are rinsed with DI water and blow dried with a $N_2$ gun. This wet etch process is very sensitive and cannot be reproduced reliably. Consequently, microscope is employed for coarse-detail evaluation of the sidewalls, and find-detail evaluation is then performed using SEM for assuming positive results. If the sidewalls are rougher than desired, the sample is dipped again in the solution.

The morphology of the sidewall is vitally important to achieve a smooth shell layer. Figure 6.6 shows 45° SEM images of microwires after undergoing the wet etch process for (a) 0 min, (c) 15 min, and (e) 25 min. The subsequent shell growth of each sample is depicted in (b), (d), and (f), respectively, and clearly shows a strong relationship between sidewall roughness and branch growth. In the extreme case, the very rough sidewalls of the sample in (a) provide a large number of nucleation sites, which result in the formation of branched nanowires during shell growth, depicted in (b). As sidewall roughness decreases, the number nucleation sites decreases resulting in fewer branch formations after shell growth in (d). This trend continues, as expected, eventually resulting in clean shell formation without branches as shown in (f).

## 6.4 Step 4: Shell growth

All microwire shell layers reported in this work are grown in a Varian Gen-II MBE system modified to handle gas sources. Thermally cracked $PH_3$ at 1000 °C and radio frequency (RF) N plasma excited at 13.56 MHz are used as P and N sources, respectively. Solid elemental Ga is used to generate a Ga beam from an effusion cell. Solid Si and Be are used as the n-type and p-type dopants, respectively.

Prior to the growth of the shells, the GaP microwire samples, for which the fabrication process is described in previous sections, are dipped into a HCl solution at room temperature for 5 minutes to remove oxide, and subsequently bonded to the substrate holder using In. In order to observe the growth morphology using RHEED, a thin film sample is mounted at the middle of the substrate holder as this is where the RHEED electron beam . The samples are then loaded into the load-lock chamber, buffer chamber, and growth chamber, respectively. In the growth chamber, oxide removal is again performed. This time is by desorption at 600 °C under $P_2$ overpressure to protect

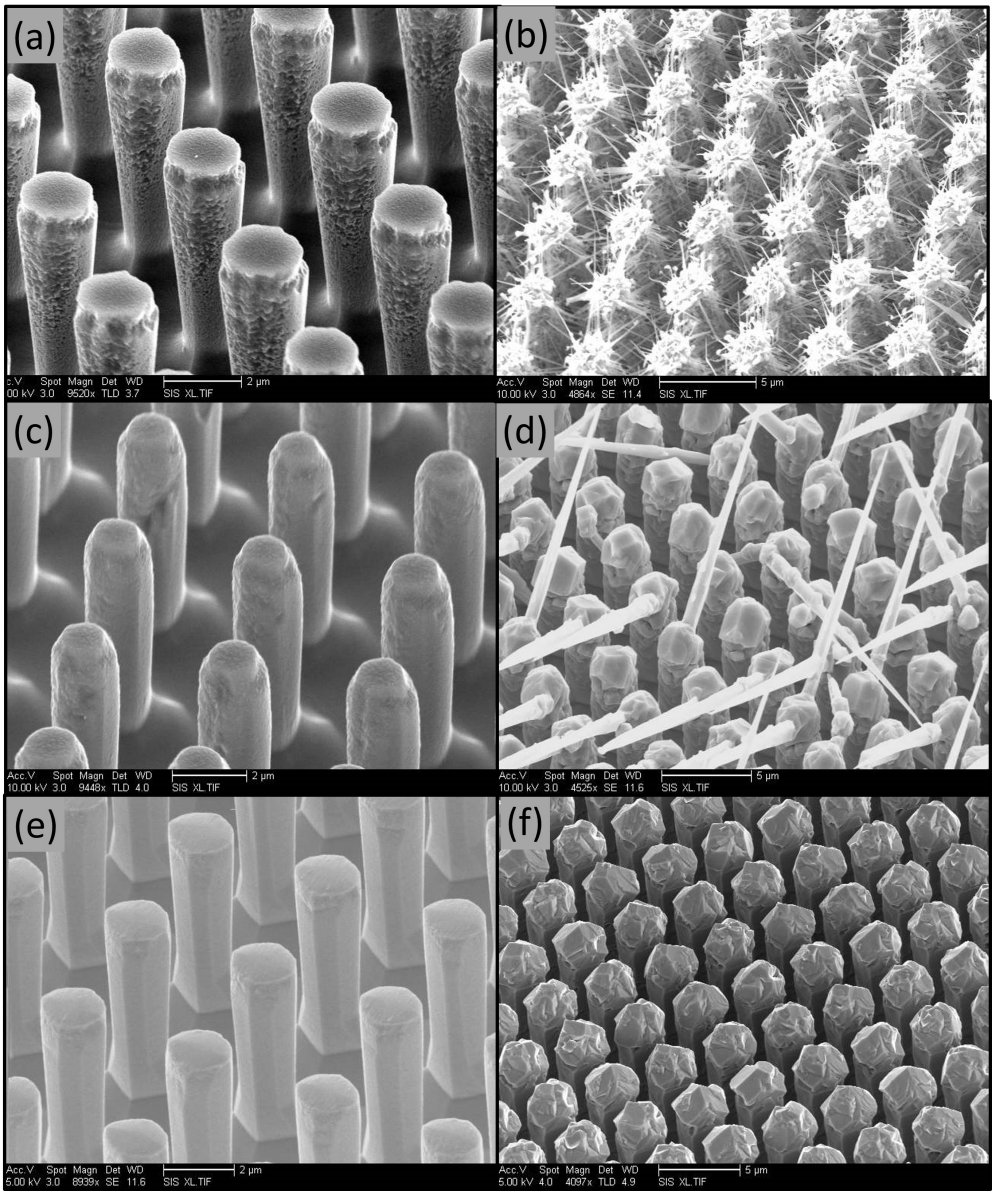


**Figure 6.6**: The 45° SEM images of microwire after wet etch process for (a) 0 min, (c) 15 min, and (e) 25 min. Their corresponding morphology of shell layer are depicted in (b), (d), and (f), respectively.

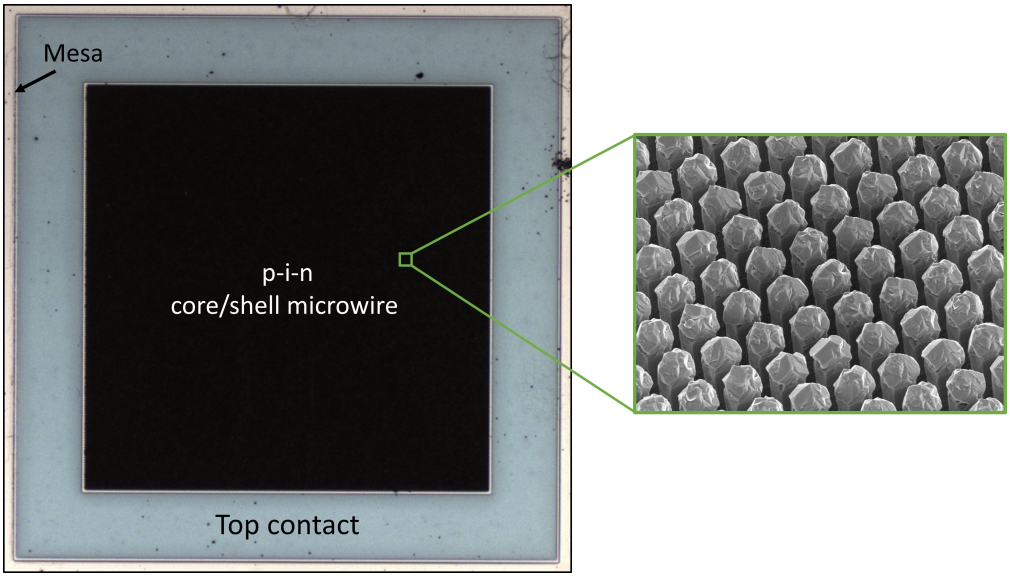


**Figure 6.7**: The optical images of our final device illustrating a top contact (blue) and a microwire array (black).

the sample surface. The $PH_3$ shutter is opened to inject $P_2$ into the chamber for the whole growth. The substrate temperature is then decreased to 570 °C, and the Ga and Be shutters are opened to grow a 200 nm p-GaP shell as a buffer layer with a doping concentration of $1.3 \times 10^{18}$ $cm^{-2}$, which is the same as the doping concentration of the substrate. Based on SEM observations of several shell growths, the growth rate of the shell roughly corresponds to half the growth rate on the thin film control sample, calibrated by Ga-induced RHEED intensity oscillation. Thus, a 200 nm thick shell corresponds to a grown buffer layer thickness of 400 nm on the thin film control sample. After completing the 200 nm p-GaP shell, the Be shutter is closed and the RF N plasma is ignited to grow a 500 nm i-GaNP shell layer. Upon completion of the 500 nm i-GaNP shell, the plasma is stopped, and then the Si shutter is opened to grow the n-GaP ($4 \times 10^{18}$ $cm^{-2}$) and $n^+$-GaP ($8 \times 10^{18}$ $cm^{-2}$) shell layer. During the growth, the V/III incorporation ratio is set approximately 2.5 and the substrate is rotated at 5 RPM to ensure uniformity.

With the GaP/GaNP core/shells fabricated, the next step is to fabricate the mi-

crowire sample into a solar cell device. The process to do so includes RTA, mesa etch, and metallization, all of which are described in Chapter 3. The final device is depicted in Figure 6.7.

# Chapter 7

# The Growth and Characterization of GaNP/GaNP core/shell Nanowire

## 7.1 Overview

In recent years, III-V semiconductor nanowires grown on Si substrate have been considered to be very promising nanoscale structures for various applications due to their combination of the superior properties of III-V materials and the low cost of Si.[71–74] With respect to solar cells, a core/shell nanowire configuration provides several advantages, which are similar to those of microwires, over traditional thin films: (1) greater light absorption,[75,76] and (2) decoupled the requirements for light absorption and carrier extraction resulting in enhancing carrier collection.[52] A further advantage of nanowires is that the core is sufficiently thin to accommodate the strain caused by lattice mismatch enabling epitaxial growth between III-V semiconductor and Si substrate.[77,78] Nanowires also open up the market for light-weight, portable, and flexible solar cells.[79,80]

Our nanowires studies focus on dilute nitride GaNP/GaNP core/shell nanowires with different N concentration within the core and shell. The GaNP/GaNP structure

exhibits a type-II band alignment, which can assist electron-hole pair radial separation across the heterojunction. In addition, N can be incorporated into GaP up to 16% allowing the GaNP bandgap to be tunable from 1.22 eV to 2.15 eV, covering a wide range of the solar spectrum.[81] To obtain the optimal solar efficiency of this promising material, a solar cell simulation software EtaOpt is employed. EtaOpt uses the detailed balance limit of efficiency to evaluate the potential power output of solar cells and then compare the performance among various bandgap structures. An ideal condition is assumed in the EtaOpt simulation: (1) all photons with E>Eg are absorbed and (2) each absorbed photon creates an electron-hole pair. In our simulation, the AM 1.5G spectrum is set to illuminate the dual junction of various bandgap structures at 300 K. The variation of the bandgaps are limited to the GaNP tunable range. The result shows that the optimal efficiency of GaNP/GaNP core/shell nanowires is $\sim$44%, with 9% [N] cores and 1% [N] shells.

This Chapter is devoted to the study of self-catalyzed GaP, GaNP, and GaNP/-GaNP nanowires grown on Si (111) substrate. Growth windows, structural properties, and optical properties are reported. The structural properties are characterized using scanning electron microscopy (SEM) and transmission electron microscopy (TEM). The optical properties are characterized using photoluminescence (PL) measurements on both the nanowire array and a single nanowire.

## 7.2 GaP nanowires

### 7.2.1 Growth

The GaP nanowire growth is a first step towards the growth of GaNP/GaNP core/shell structure. Prior to all growth, the Si (111) substrate is dipped in an HF solution at room temperature for 10 seconds to remove the intrinsic oxide, and then it is rinsed

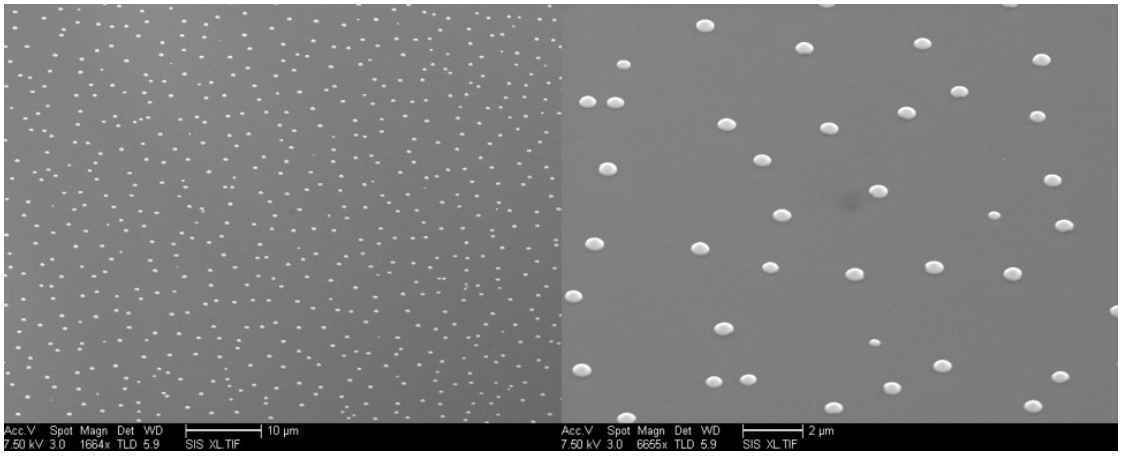


**Figure 7.1**: Ga droplets as catalysts on Si (111).

with deionized (DI) water. The substrate is then treated in 30% KOH at 80 °C for 20 seconds to expose a fresh Si surface, and then it is rinsed with methanol. The substrate is again dipped in an HF solution for 10 seconds and then rinsed with DI water. The substrate is finally blow dried with a $N_2$ gun, and then it is immediately loaded into the MBE load-lock chamber. In the growth chamber, the substrate is heated to ∼710 °C for 15 minutes for thermal cleaning, and then substrate temperature ($T_{sub}$) is decreased to the growth temperature.

The GaP growth is initiated by depositing Ga atoms as catalysts on the Si (111) surface at an amount needed to grow 16 monolayers (MLs) of GaP thin film. The film is then annealed for 30 seconds to form Ga droplets, as shown in Figure 7.1. $PH_3$ is subsequently injected into the growth chamber through a hydride injector together with Ga flux. During growth, the Ga flux is set to 0.63 ML/s, calibrated by Ga-induced reflection high energy electron diffraction (RHEED) intensity oscillation for the planar growth of GaP under the same $T_{sub}$. GaP nanowire growth lasts 15 minutes under a V/III incorporation ratio of 2.5 and a substrate rotation speed of 8 RPM..

To study the growth windows and the temperature-dependent structural characteristics of GaP nanowires, the growth runs are performed at several $T_{sub}$: 515 °C, 585

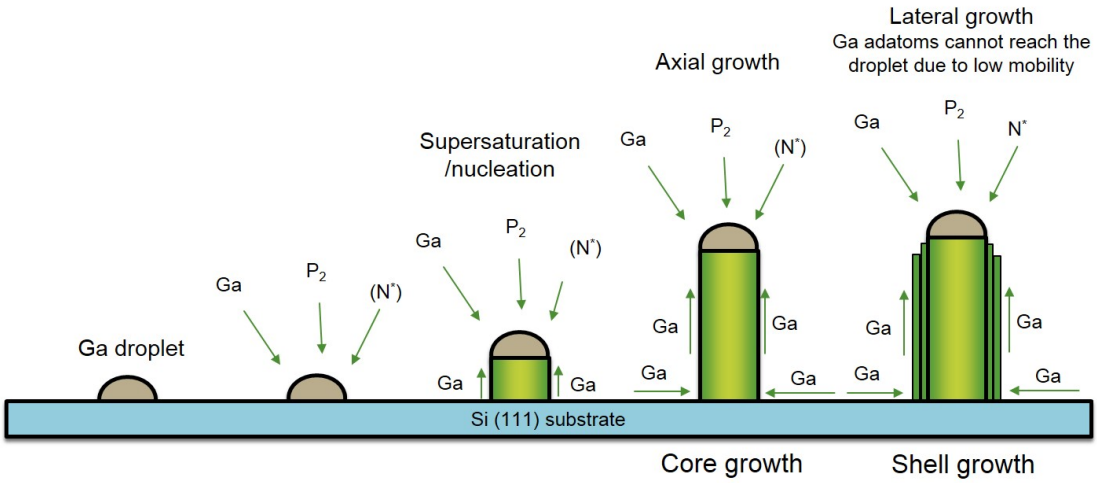


**Figure 7.2**: The schematic showing the VLS growth of Ga(N)P/GaNP core/shell nanowires.

°C, 600 °C, 615 °C, and 630 °C, which correspond to GaP-515, GaP-585, GaP-600, GaP-615, and GaP-630, respectively.

### 7.2.2 Structural properties and discussion

The vapor-liquid-solid (VLS) growth mechanism, suggested by Wagner in 1964, has been widely used to explain the growth of nanowires,[82] as shown in Figure 7.2. In this mechanism, the nanowires are assumed to be grown by the adsorption of vapor atoms on the catalyst nanoparticles (Ga droplets) and their transfer to the crystal phase due to the solidification of liquid alloy under the droplets. Consequently, the diameters of the subsequently grown nanowires depend on the size of the droplets. Thermodynamically,[83] the minimum radius of a liquid droplet is defined as

$$R_{min} = \frac{2\sigma_{VL}V_L}{RT_{sub}ln\sigma} \tag{7.1}$$

where $\sigma_{VL}$ is the liquid-vapor surface free energy, $V_L$ is the molar volume, and $\sigma$ is the vapor phase supersaturation. According to Equation 7.1, using high $T_{sub}$ results in small

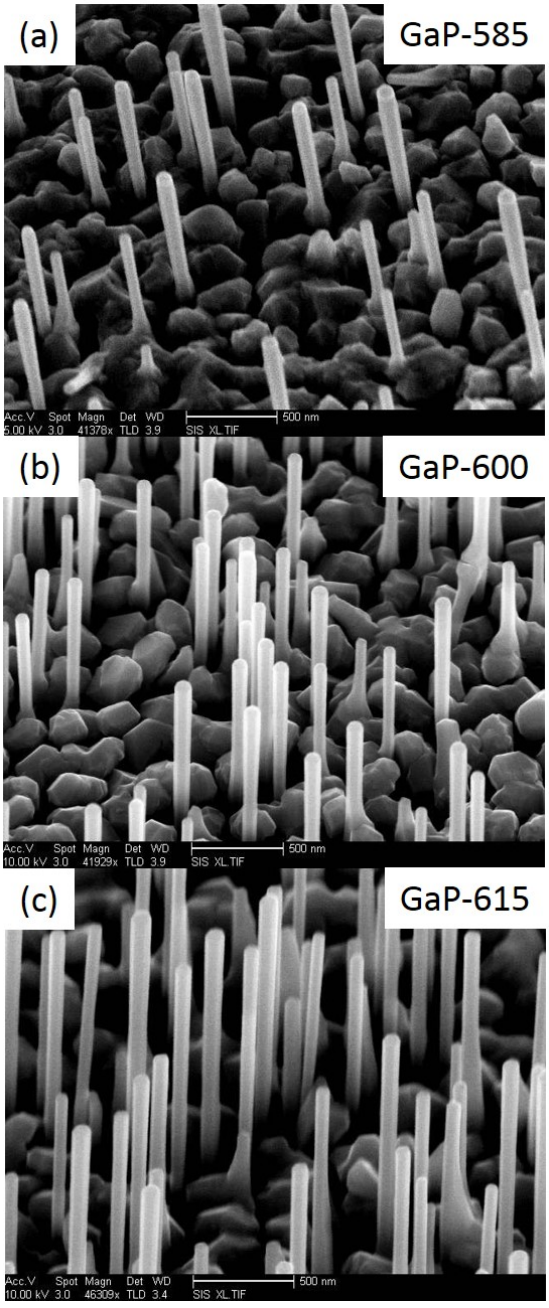


**Figure 7.3**: SEM images of GaP nanowires on Si (111): (a) GaP-585, (b) GaP-600, and (c) GaP-615.

**Table 7.1**: The average diameters and lengths of nanowires grown at different temperatures

| $T_{sub}$ (°C) | Diameter (nm) | Length ($\mu$m) |
|---|---|---|
| GaP-515 | - | - |
| GaP-585 | 89±9 | 0.84±0.06 |
| GaP-600 | 83±4 | 0.93±0.02 |
| GaP-615 | 76±8 | 1.35±0.13 |
| GaP-630 | - | - |

droplets that, in turn, yield nanowires with a small diameter.

In our growth experiment, vertical GaP nanowires are successfully grown on the Si (111) substrate under $T_{sub}$ from 585 °C to 615 °C. These growths are depicted in Figure 7.3 and are referred to as GaP-585, GaP-600, and GaP-615, respectively. Their corresponding average diameters and lengths, depicted in Table 7.1, are 89±9 nm, 83±4 nm, and 76±8 nm, respectively. At higher $T_{sub}$, the average diameter of our grown nanowires becomes smaller, which is in line with Equation 7.1. Moreover, at high $T_{sub}$, Ga adatoms contribute to axial growth, in the [111] direction, rather than lateral growth because the surface mobility is higher such that Ga adatoms diffuse to the Ga droplets on nanowire tips and grow preferentially in the [111] direction.[84]

The higher growth rate of nanowires via the VLS mechanism depends on several factors such as a higher rate of chemical reaction, better adsorption on the droplet, and a faster nucleation of crystal phase. This implies that thick nanowires with large droplets grow faster than thin nanowires. On the other hand, the nanowire growth rate from MBE, in contrast to chemical vapor deposition (CVD), is also by diffusion-induced mode,[85] increased by the contribution of adatoms diffusing from the substrate and the sidewall up to the catalyst. From theoretical calculations, the diffusion-induced contribution has a larger effect on smaller nanowires. This could be because a larger amount of adatoms

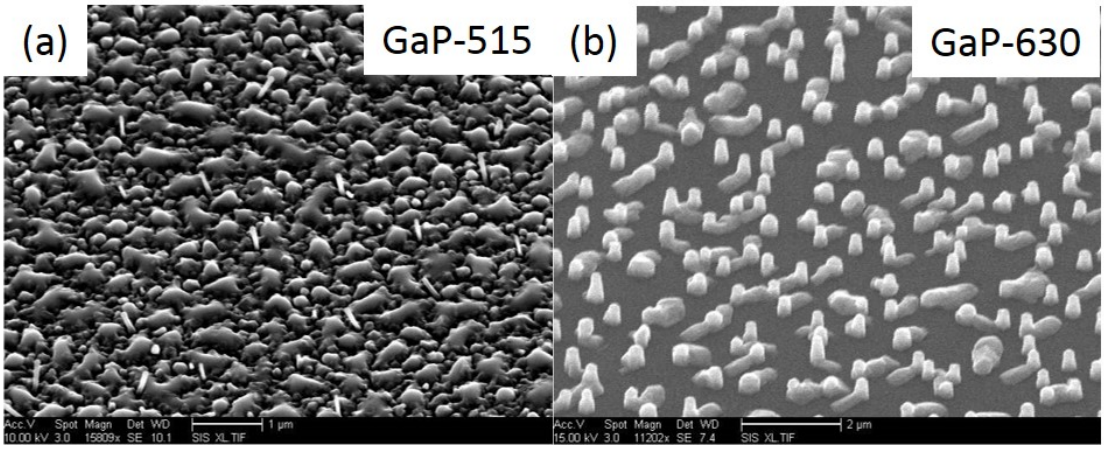


**Figure 7.4**: SEM images showing the GaP nanowires grown outside the growth temperature window: (a) GaP-515, and (b) GaP-630.

diffuses from the substrate surface to the tip of the nanowire as the diameter of the nanowire increases. This is attributed to the larger area, $\pi dL$, of the side surface of the nanowire, where d is nanowire diameter, and L is nanowire length. On the contrary, as the diameter increases, the required amount of adatoms for grown nanowire increases as $\pi d^2 L$.

Table 7.1 shows that greater nanowire length is achieved at higher growth temperatures or at smaller nanowire diameters. The observed lengths are 840±60 nm, 930±20 nm, and 1350±130 nm for GaP-585, GaP-600, and GaP-615, respectively. In other words, smaller diameter nanowires have higher axial growth rate. In MBE, the nanowire growth rate is the combination of the VLS-controlled and diffusion-induced modes. Our growth, regardless $T_{sub}$, shows the diffusion-induced mode is dominant. Raising $T_{sub}$ also increases the effect of diffusion-induced mode. At high $T_{sub}$, Ga adatom mobility on the surface is increased. Consequently, more Ga adatoms can diffuse to the Ga droplets on nanowire tips, which contribute to the nanowire axial growth.

At temperatures outside the range of 585 °C to 615 °C, GaP nanowires could not be grown. Growth results outside this range are shown in Figure 7.4. At low $T_{sub}$ (GaP-515), the short diffusion length of Ga adatoms on the surface due to the low Ga

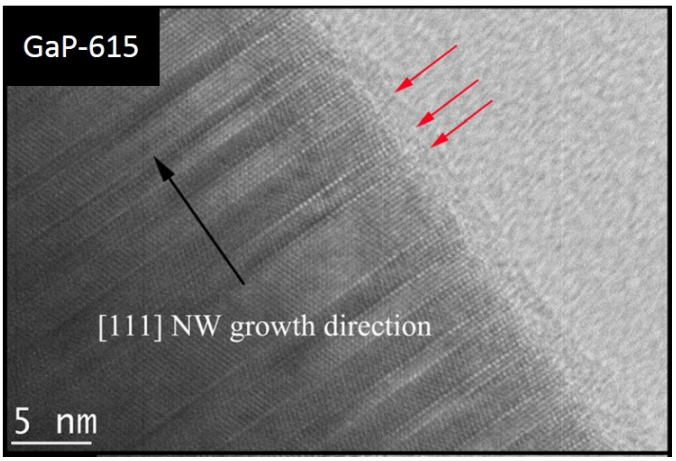


**Figure 7.5**: TEM image of GaP-615 showing the twinning planes (red solid arrow) along [111] nanowire growth direction.

adatom mobility impedes the diffusion-induced growth mode. Thus, only the adatom flux directing to the droplets, which is low compared to the total flux, can contribute to the nanowire growth. On the other hand, due to the Gibbs-Thompson effect, the chemical potential difference of the components in the alloy droplet increases as the size of the droplet decreases.[86] Hence, it becomes more difficult for the vapor component to dissolve into a small size of liquid alloy. At high $T_{sub}$ (GaP-630), it is possible that only a small amount of vapor can dissolve into Ga droplets due to the small size of the droplets, as shown in Equation 7.1. Consequently, the liquid alloys do not reach the supersaturation state thereby preventing them from contributing to the growth of nanowires.

For further structural analyses, TEM experiments are performed on GaP-615 using an FEI-Tecnai microscope operating at 300 keV. The TEM image, shown in Figure 7.5, shows that the crystal structure of the GaP nanowires is a mixture of cubic zincblend (ZB) phase and hexagonal wurtzite (WZ) phase, resulting in random twinning planes between these phases along the [111] NW growth direction. These twinning planes are commonly observed for III-V semiconductor nanowires with moderate ionicity values, including GaP, due to the small energy difference between ZB and WZ.[87]

## 7.3 GaNP nanowires

### 7.3.1 Growth

After GaP nanowires are successfully grown vertically on Si (111), GaNP nanowires were grown on Si (111) with the similar growth conditions but injecting N plasma in the growth. However, we found that GaNP nanowires could not be grown under RF-plasma-activated N ambient.[88] One possible reason is that the activated N ambient increases the nucleation rate at the substrate surface such that it is comparable to the nucleation rate at the droplet/Si interface, resulting in planar formation of GaNP instead of nanowires. Consequently, we modified the growth conditions by initiating growth of short GaP nanowires first and then activated N plasma to grow GaNP nanowires.

Prior the growth, the Si (111) substrate is prepared the same way as the GaP growth, described in Section 7.2.1. Then, in the growth chamber, Ga atoms are deposited as catalysts on the Si (111) substrate for 30 seconds with a Ga flux of $\sim$0.7 ML/s, and is annealed for 30 seconds to form Ga seed droplets. Growth started by opening the Ga shutter and injecting $PH_3$ into the growth chamber to initiate growth of GaP nanowires. After 90 seconds of growth, RF N plasma is then ignited, and the GaNP nanowires are grown for 15 minutes with a V/III incorporation ratio of $\sim$2.5. To ensure uniformity, the substrate is rotated at 5 RPM during growth.

To study the growth window of GaNP nanowires, $T_{sub}$ is set to 515 °C, 585 °C, 600 °C, 615 °C, and 630 °C, henceforth referred to as GaNP-515, GaNP-585, GaNP-600, GaNP-615 and GaNP-630, respectively.

### 7.3.2 Structural properties and discussion

By first growing the GaP nanowire seeding roots, GaNP can be successfuly grown, as shown in Figure 7.6, for $T_{sub}$ from 585 °C to 615 °C, which are comparable to the

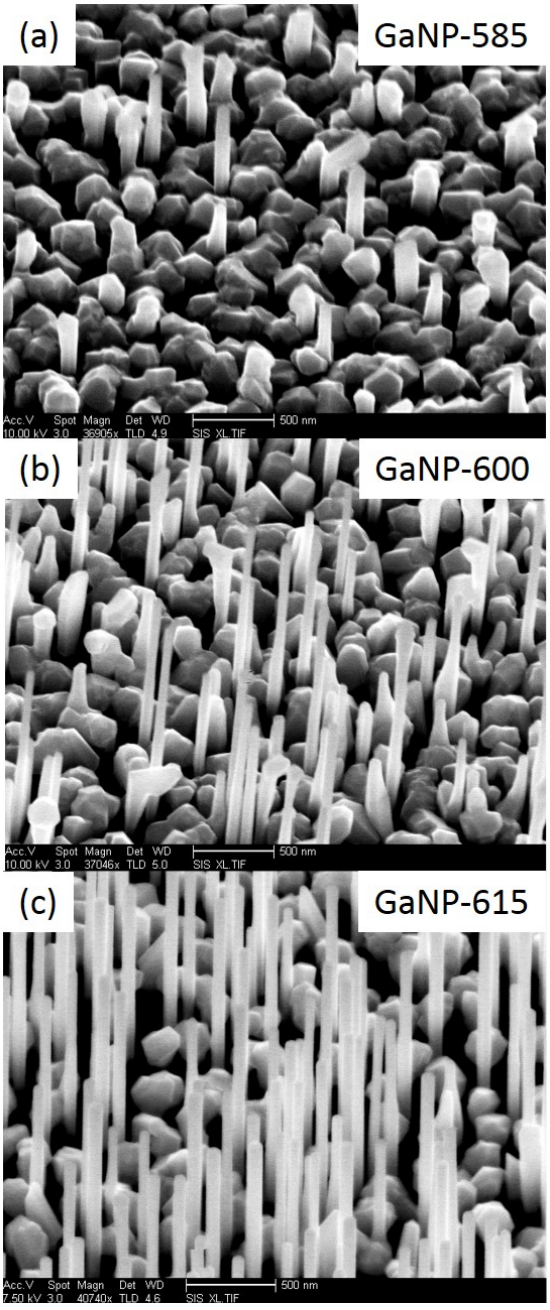


**Figure 7.6**: SEM images of GaNP nanowires on Si (111): (a) GaNP-585, (b) GaNP-600, and (c) GaNP-615.

**Table 7.2**: The average diameters and lengths of GaNP nanowires grown at different temperatures

| $T_{sub}$ (°C) | Diameter (nm) | Length ($\mu$m) |
|---|---|---|
| GaNP-515 | - | - |
| GaNP-585 | 92±13 | 0.4±0.1 |
| GaNP-600 | 67±5 | 0.7±0.1 |
| GaNP-615 | 65±9 | 2.2±0.1 |
| GaNP-630 | - | - |

growth window of GaP nanowires. Within the growth window, as $T_{sub}$ increases, the average diameter of nanowires decreases, while the average length increases, as shown in Table 7.2. This trend is in line with the explanation detailed in Section 7.2.2. Below the growth window (GaNP-515), the short Ga adatom diffusion length on the surface impedes VLS growth. Conversely, above the growth window (GaNP-630), only a small amount of vapor can dissolve into Ga droplets and contribute to VLS growth.

For further analyses, TEM experiments are performed on GaNP-615. The crystal structure of GaNP-615 features random twins and stacking faults between cubic ZB and hexagonal WZ phases along the [111] nanowire growth direction as illustrated in Figure 7.7. This mixture of the two structures are also observed in GaP nanowires, as shown in Figure 7.5. Based on our examination, the majority phase of GaNP nanowires is still ZB, which is also favored by GaNP thin films. Figure 7.7(d) shows the high resolution electron microscopy image of the boxed region of Figure 7.7(a). This clearly presents both structures exist - the upper and lower halves are associated with WZ and ZB phases, respectively, as clarified by the fast Fourier transformation images.

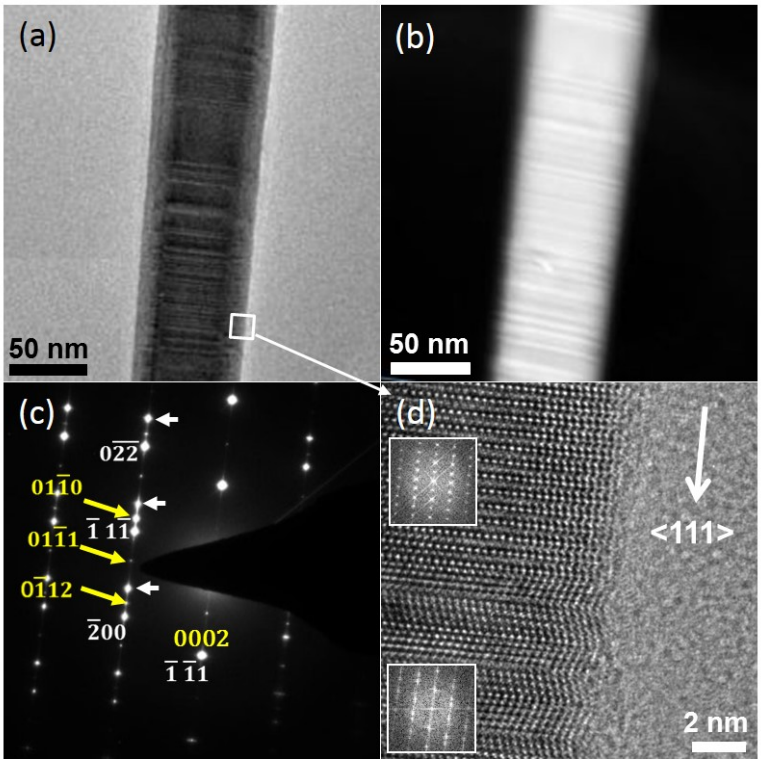


**Figure 7.7**: TEM images of GaNP nanowires (GaP-615). (a),(b) ZB and WZ phases are formed in parallel in individual nanowires. (c) In transmission electron diffraction (TED) pattern, twin spots are indicated by white arrows, and ZB and WZ spots are indexed in white and yellow, respectively. (d) High resolution TEM image showing ZB and WZ structure with corresponding fast Fourier transformation images.

## 7.4 GaNP/GaNP core/shell nanowires

### 7.4.1 Growth

Among our GaNP nanowire samples, GaNP-615 has the highest density ranging from $\sim 4 \times 10^8$ cm$^{-2}$ to $\sim 1.2 \times 10^9$ cm$^{-2}$ across the substrate with an axial growth rate of $\sim$150 nm/minute. Consequently, the growth conditions of GaNP-615 are employed to grow the core of GaNP/GaNP core/shell nanowires (S-GaNP/GaNP). For S-GaNP/GaNP, the GaNP cores are grown at 615 °C, subsequently, $T_{sub}$ is decreased to 450 °C and the V/III incorporation ratio is increased to 3.5 by increasing the $PH_3$ flow rate and the shells are grown for 15 minutes. Decreasing $T_{sub}$ and increasing the V/III incorporation ratio

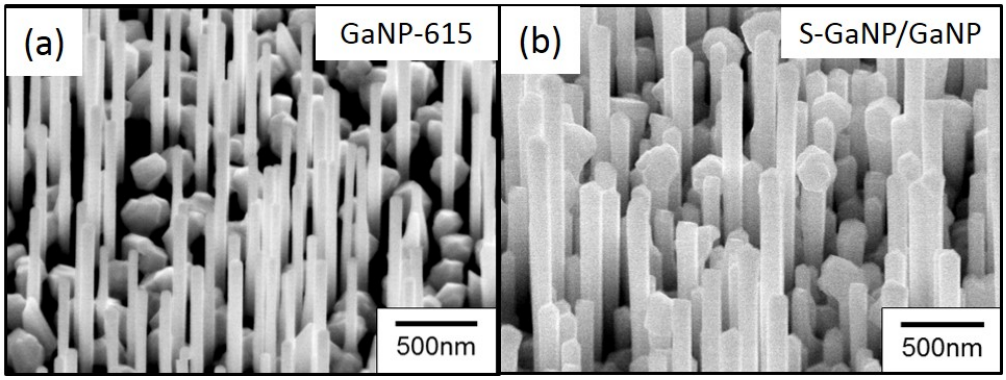


**Figure 7.8**: SEM images showing (a) GaNP-615 (the cores of S-GaNP/GaNP) and (b) S-GaNP/GaNP.

reduce Ga adatom mobility on the growing surface. This decreased mobility suppresses the VLS mechanism, which decreases axial growth rate, and, instead, promotes the radial growth rate through step-mediated growth mode as shown in Figure 7.2. Lowering the $T_{sub}$ facilitates N incorporation; hence, a higher N composition is expected in the shell.

### 7.4.2 Structural properties and discussion

Figure 7.8 shows the SEM images of GaNP-615 (the cores of S-GaNP/GaNP) and S-GaNP/GaNP. For S-GaNP/GaNP, the average diameter and length of the nanowires are 115$\pm$4 nm and 2.3$\pm$0.2 m, respectively. After the shell is grown, the average diameter increased by $\sim$80% with no significant increase in length. This confirms that lowering $T_{sub}$ and increasing the V/III incorporation ratio suppress the axial growth, instead, promote the radial growth.

### 7.4.3 Optical properties and discussion

PL measurements are carried out for optical studies. Figure 7.9 illustrates the results of PL measurements at 300 K, performed on GaNP-615, and S-GaNP/GaNP. The PL emission shows single PL peaks for GaNP-615 and S-GaNP/GaNP. The single PL

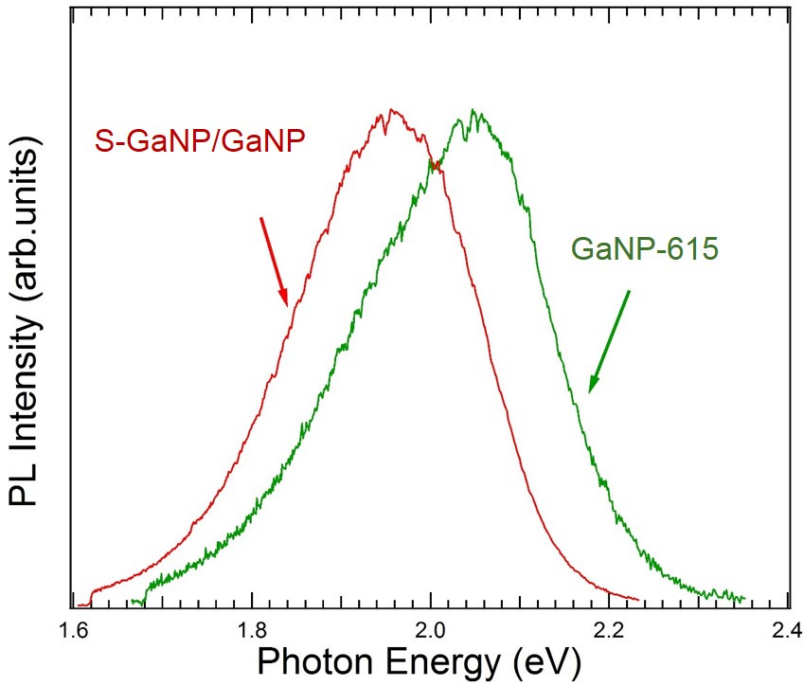


**Figure 7.9**: PL emission from arrays of GaNP-615 and S-GaNP/GaNP performed at 300 K.

peaks of S-GaNP/GaNP is believed to come from their shells, as a result of fast diffusion of photo-excited electrons from the core to the shell with lower conduction band edge for S-GaNP/GaNP. With regard to GaNP-615, the higher energy PL peak is attributed to lower N incorporation in the core ([N]$\sim$1%) relative to the shell ([N]$\sim$2%) based on studies of PL emission vs. N, in which an increase in [N] causes a red-shift of the PL emission.

In addition, PL signals from an ensemble nanowires and a single nanowire are compared. For an ensemble nanowire study, the nanowires are dry transferred to another Si substrate and then are characterized by PL measurement at room temperature. The individual nanowire was characterized by Prof. Buyanova's lab using their micro PL ($\mu$PL) employing a Horiba Jobin Yvon HR800 spectrometer with a 325 nm He-Cd laser. These experiments are carried on GaP/GaNP core/shell nanowires (S-GaP/GaNP), for

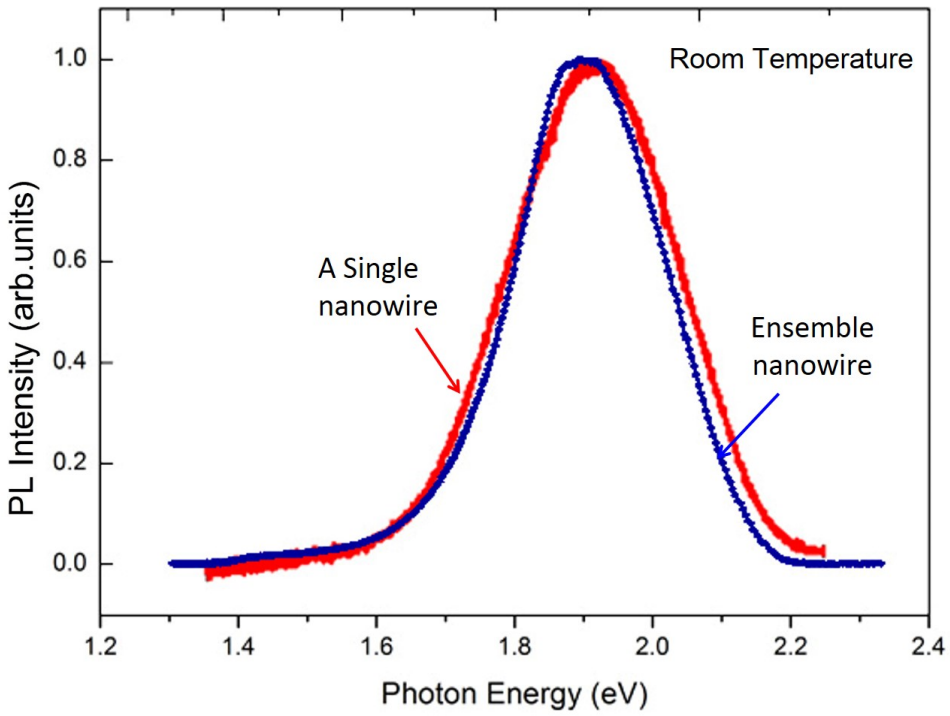


**Figure 7.10**: PL emissions from an ensemble (blue) and a single (red) S-GaP/GaNP.

which the shell was grown using the same conditions as the shell of S-GaNP/GaNP. Since GaP has indirect bandgap, the PL signals result from only GaNP shells.

According to PL between an ensemble S-GaP/GaNP and a single S-GaP/GaNP, it is notable that the width of the PL spectra from the ensemble and single nanowires are nearly identical, with a full width at half maximum (FWHM) of ∼0.3 eV. This suggests that the width of the signal is not due to the variation of N content among different nanowires, but the mechanism for light emission of nanowires. This supports the explanation that the radiative recombination originates from the excitons trapped at various N-related localized states of GaNP.

## 7.5 Conclusions

In summary, vertical self-catalyzed GaP, GaNP, and GaNP/GaNP core/shell nanowires are successfully grown on Si (111) using GSMBE. The growth window of GaP nanowires is from ∼585 °C to ∼615 °C, which are comparable to the growth window of GaNP nanowires. The shells are grown by decreasing $T_{sub}$ and increasing the V/III incorporation ratio to reduce adatom mobility and increase N incorporation. According to TEM measurements, the crystal structures of GaP and GaNP nanowires are mixtures of cubic ZB phase and hexagonal WZ phase along the [111] growth direction. With regard to optical properties, photo-excited electrons in the core exhibit fast diffusion to the shell, which has lower conduction band edge. The nearly identical PL line shape of an ensemble of GaP/GaNP core/shell nanowires and a single nanowire indicates that the broad PL width of an ensemble nanowires does not result from the variation of N composition among nanowires, but from the mechanism of light emission.

## 7.6 Acknowledgments

This Chapter was partially published in **S. Sukrittanon**, Y. J. Kuang, C. W. Tu, "Growth and characterization of GaP/GaNP core/shell nanowires", *J. Vac. Sci, Technol. B*, 31, 03C110 (2013) and **S. Sukrittanon**, Y. J. Kuang, A. Dobrovolsky, W. M. Kang, J. S. Jang, B. J. Kim, W. M. Chen, I. A. Buyanova, C. W. Tu, "Growth and characterization of dilute nitride $GaN_xP_{1-x}$ nanowires and $GaN_xP_{1-x}$/$GaN_yP_{1-y}$ core/shell nanowires on Si (111) by gas source molecular beam epitaxy", *Appl. Phys. Lett.*, 105, 072107 (2014). Financial support of the work was provided by the National Science Foundation under Grant Nos. DMR-0907652, DMR-1106369 and the Royal Government of Thailand Scholarship (DPST). The photoluminescence experiments were supported by the Swedish Research Council (Grant No. 621-2010-3815). The TEM

experiments were supported by the National Science Foundation of Korea (NRF) and the Korea government (2013R1A1A1007978), and the Ministry of Trade, Industry and Energy (MTIE) through the industrial infrastructure program under Grant No. 10033630.

# Chapter 8

# Future work

## 8.1 Thin film solar cells

Our best GaNP thin film solar cell with anti-reflection (AR) coating achieves an efficiency of 7.9% with short circuit current ($J_{sc}$) of 8.53 mA/cm$^2$, open circuit voltage ($V_{oc}$) of 1.33 V, and fill factor (FF) of 0.69. According to its external quantum efficiency (EQE) in Figure 4.9(b), greater efficiency can be achieved by improving the EQE performance in the short-wavelength (<425 nm) and long-wavelength (>550 nm) regions.

Based on our analysis, short wavelength EQE can be improved in a number of ways: (1) increasing the diffusion length in the emitter region (e.g., optimizing growth conditions, lowering doping concentration), (2) optimizing the emitter thickness, and (3) reducing the front surface recombination velocity (e.g., passivation, window layer). A promising window layer for our GaNP solar cell that we recommend for further study is AlGaP. This material features a higher bandgap than GaP resulting in reduced photon absorption in the passivation layer. It possesses a small lattice mismatch with GaP, and it has already been demonstrated that it can reduce the surface recombination velocity of

GaP from $1 \times 10^6$ cm/s to $1 \times 10^4$ cm/s.[20,89]

Long wavelength EQE can be improved by increasing the thickness of the GaNP i-layer of the solar cell. The maximum i-layer thickness of 2 *mu* studied in this work was not found to be a limiting factor in solar efficiency. Thus, we conclude increasing the thickness of the i-layer should further increase solar efficiency until the gain in greater light absorption is outweighed by the recombination current in the depletion region.

In addition to optimizing EQE, future work should also focus on incorporating additional N and/or As as a means to decrease the bandgap of GaNP to the optimal value of $\sim$1.7 eV for dual-junction configurations in which the bottom cell is composed of Si. Finally, detailed investigations into the integration of GaNP(As) solar cells onto Si substrates need to be performed.

## 8.2 Microwire solar cells

Our best core/shell GaP/GaNP microwire solar cell with AR coating (microwire length = 6 $\mu$m, array period = 6 $\mu$m) achieves an efficiency of 3.2%. The short-wavelength EQE and long-wavelength EQE of the microwire solar cells can be optimized using techniques similar to those described for our thin film solar cells in Section 8.1. Additionally, efficiency can be further increased by optimizing the structure's geometry (e.g., microwire length, microwire diameter, array period, array pattern). However, MBE shadow effect must be accounted for. A more focused examination of the microwire sidewall roughness should also be undertaken as our analysis indicates surface roughness is strongly related to solar efficiency. Regarding to the fabrication process, smoother sidewalls resulted in fewer defects and, consequently, higher efficiency so further investigation into wet etch optimization (e.g., adjusting wet etch solution ratio, reducing bubble formation using a magnetic stirrer) is recommended. Finally, minimization of defects and

threading dislocations by optimizing the shell growth process (e.g., adjusting the growth temperature and growth rate[89]) and the solar cell structure (e.g., adding superlattices[90–92]) should be performed.

# Appendix A

# MATLAB scripts for a p-i-n GaP/GaNP solar cell

## A.1 The effect of the i-GaNP layer

The following MATLAB script is used to calculate the effect of the i-GaNP width on short circuit current ($J_{sc}$) and external quantum efficiency (EQE) of a p-GaP/i-GaNP/n-GaP solar cell in Section 2.4.2. A modified version of this MATLAB script that sweeps across different variables is also used in Sections 2.4.3 and 2.4.4.

```
clc
clear
%Constant definitions
%spectrum irradiance (W*m-2*nm-1)
bs0 = [3.3569E-03
6.5654E-02
2.0579E-01
4.0688E-01
```

4.5418E-01

5.1862E-01

5.4231E-01

6.6788E-01

1.0847E+00

6.7673E-01

9.3964E-01

1.1668E+00

1.2235E+00

1.1376E+00

1.3480E+00

1.4987E+00

1.5611E+00

1.5562E+00

1.5976E+00

1.5198E+00

1.5490E+00

1.5578E+00

1.4952E+00

1.5348E+00

1.5353E+00

1.5427E+00

1.5153E+00

1.4932E+00

1.5042E+00

1.4497E+00

1.4657E+00

1.4715E+00

1.4423E+00

1.4107E+00

1.4470E+00

```
1.4014E+00
1.3570E+00
1.4139E+00
1.3933E+00
1.2180E+00
1.2919E+00
];

%Wavelength (nm)
lam = [3.0000E+02
3.1000E+02
3.2000E+02
3.3000E+02
3.4000E+02
3.5000E+02
3.6000E+02
3.7000E+02
3.8000E+02
3.9000E+02
4.0000E+02
4.1000E+02
4.2000E+02
4.3000E+02
4.4000E+02
4.5000E+02
4.6000E+02
4.7000E+02
4.8000E+02
4.9000E+02
5.0000E+02
5.1000E+02
```

```
5.2000E+02
5.3000E+02
5.4000E+02
5.5000E+02
5.6000E+02
5.7000E+02
5.8000E+02
5.9000E+02
6.0000E+02
6.1000E+02
6.2000E+02
6.3000E+02
6.4000E+02
6.5000E+02
6.6000E+02
6.7000E+02
6.8000E+02
6.9000E+02
7.0000E+02
];

%Reflectance of GaP
R = [0.335389271
0.338317678
0.358920463
0.387429202
0.46732241
0.462001638
0.425036008
0.410300539
0.397651128
```

0.386522899

0.376718617

0.368397468

0.361528971

0.355637645

0.355637645

0.349013391

0.34002413

0.34002413

0.34002413

0.323432229

0.31695021

0.31695021

0.311190855

0.311190855

0.305920486

0.301336477

0.301336477

0.297115935

0.297115935

0.293208024

0.293208024

0.289535326

0.289535326

0.286013677

0.286013677

0.286013677

0.286013677

0.286013677

0.282968709

0.282968709

```
0.280219865
];

%absorption coefficient of GaP
alpha = [436332
440026
455180
493335
249576
145283
97857
80000
71244
54643
43207
34054
30000
26896
16744
11000
3694
2500
1450
1000
760
600
487
350
233
0
0
```

```
0
0
0
0
0
0
0
0
0
0
0
0
0
];

%absorption coefficient of GaNP
alphaN =[436332
440026
455180
493335
249576
145283
97857
80000
71244
54643
43207
34054
30000
26896
```

```
24000
24000
24000
24000
24000
21000
21000
21000
21000
19777.34352
18140.75909
15074.87478
12736.7502
10047.57244
6987.87609
3876.71375
1677.71656
527.5873
204.7378
5.74542
0.19919
0
0
0
0
0
0
];

%parameters of p-GaP/i-GaNP/n-GaP
Eg = 2.26; %eV
```

```
n = 1; % ideality factor
q = 1.6e-19;
Nc = 1.8e19;
Nv = 1.9e19;

De = 1.68;
Ne = 4e18;
Le = 0.19e-4;
Se = 1e6;
We = 0.1e-4;
te= 1e-6;

Db = 1.53;
Nb = 6.5e17;
Lb = 4.1e-4;
Sb = 1e6;
Wb = 300e-4;
tb = 0.1e-6;

Wi = 800e-7;

%photon flux
bs = bs0./q.*lam./1240;

i = 1;
for Wi = [0 2e-5 5e-5 1e-4 5e-4 1e-3]

%minority carrier current density from the emitter
Jln1 = q.*bs.*(1-R).*alpha.*Le./((alpha.*Le).^2-1);
Jln2 = (Se.*Le./De+alpha.*Le)-exp(-alpha.*We)
.*(Se.*Le./De.*cosh(We./Le)+sinh(We./Le));
```

```
Jln3 = Se.*Le./De.*sinh(We./Le)+cosh(We./Le);
Jln4 = alpha.*Le.*exp(-alpha.*We);
Jln  = Jln1.*(Jln2./Jln3-Jln4);

%minority carrier current density from the base region
Jlp1 = (q.*bs.*(1-R).*alpha.*Lb./((alpha.*Lb).^2-1))
.*exp(-alpha.*We).*exp(-alphaN.*Wi);
Jlp2 = Sb.*Lb./Db.*(cosh(Wb./Lb)-exp(-alpha.*Wb));
Jlp3 = sinh (Wb./Lb)+alpha.*Lb.*exp(-alpha.*Wb);
Jlp4 = Sb.*Lb./Db*sinh(Wb./Lb)+cosh(Wb./Lb);
Jlp5 = alpha.*Lb;
Jlp = Jlp1.*(Jlp5-(Jlp2+ Jlp3)./Jlp4);

%current density generated in the i-region
Jgen = q.*bs.*(1-R).*exp(-alpha.*We).*(1-exp(-alphaN.*Wi));

%total current density
J  = Jln+Jlp+Jgen;

%short current current density
Jsc (i,:) = 0.1*trapz(lam,J);

%EQE
QE1 (:,i)= J./q./bs;
i = i+1;

plot(lam, QE1,'r')
hold on
end
```

## A.2 The effect of carrier lifetime in the i-GaNP layer

The following MATLAB script is used in Section 2.4.5 to calculate open circuit voltage ($V_{oc}$) and solar cell efficiency ($\eta$) of a p-GaP/i-GaNP/n-GaP solar cell under various carrier lifetimes within the i-GaNP layer.

```
clc
clear
%Constant definitions
Eg = 2.26; %bandgap of GaP
EgN = 2.05; %bandgap of GaNP
n = 1; % ideality factor
q = 1.6e-19;
Nc = 1.8e19;
Nv = 1.9e19;

De = 1.68;
Ne = 4e18;
Le = 0.19e-4;
Se = 1e6;
We = 0.1e-4;
te= 1;

Db = 1.53;
Nb = 6.5e17;
Lb = 4.1e-4;
Sb = 1e6;
Wb = 300e-4;
tb = 1;
```

```
Wi = 1e-4;

i = 1;
for te = [1000000000 100000000 10000000 1000000 100000 10000
1000 100 10 1 0.1 0.01 0.001 0.0001];

%diffusion current
Jn = q.*De.*Nc.*Nv./Le./Ne.*((Se.*cosh(We/Le)+De./Le.*sinh(We./Le))
./(De./Le.*cosh(We./Le)+Se.*sinh(We./Le)));
Jp = q.*Db.*Nc.*Nv./Lb./Nb.*((Sb.*cosh(Wb./Lb)+Db./Lb.*sinh(Wb./Lb))
./(Db./Lb.*cosh(Wb./Lb)+Sb.*sinh(Wb./Lb)));
J0 = (Jn+Jp).*exp(-Eg./0.0259);

%recombination current at depletion region
Jscr = q*((Nc*Nv/te/te)^(1/2))*Wi;% assume that te = tb
Jscr1 = Jscr*exp(-EgN./2./0.0259);

%total dark current
Jt (i,1)= J0 + Jscr1;
Jsc = 6.93306039929750; % from Section A.1

%open circuit voltage
Voc (i,1) = 0.0259.*log(Jsc./Jt(i,1)+1)

%fill factor
Voc1(i,1) = Voc(i,1)/0.0259;
FF (i,1)= (Voc1(i,1)-log(Voc1(i,1)+0.72))./(Voc1(i,1)+1)

%efficiency
eff (i,1)= Jsc.*Voc(i,1).*FF(i,1)
```

```
i = i+1;
end
```

# Bibliography


[1] Solar cell efficiency. *https://en.wikipedia.org/wiki/Solarcellefficiency*, (accessed November, 2015).

[2] GTM Research PV Pulse. 2015.

[3] Martin A. Green, Keith Emery, Yoshihiro Hishikawa, Wilhelm Warta, and Ewan D. Dunlop. Solar cell efficiency tables (version 46). *Progress in Photovoltaics: Research and Applications*, 23(7):805–812, 2015.

[4] Martin A. Green, Keith Emery, Klaus Bcher, David L. King, and Sanekazu Igari. Solar cell efficiency tables (version 14). *Progress in Photovoltaics: Research and Applications*, 7(4):321–326, 1999.

[5] T. J. Grassman, J. A. Carlin, C. Ratcliff, D. J. Chmielewski, and S. A. Ringel. Epitaxially-grown metamorphic GaAsP/Si dual-junction solar cells. In *Photovoltaic Specialists Conference (PVSC), 2013 IEEE 39th*, pages 0149–0153, June 2013.

[6] Sarah R. Kurtz, P. Faine, and J. M. Olson. Modeling of two-junction, series-connected tandem solar cells using top-cell thickness as an adjustable parameter. *Journal of Applied Physics*, 68(4), 1990.

[7] J. F. Geisz and D. J. Friedman. III-N-V semiconductors for solar photovoltaic applications. *Semiconductor Science and Technology*, 17(8):769, 2002.

[8] S.M. Vernon, V.E. Haven, S.P. Tobin, and R.G. Wolfson. Metalorganic chemical vapor deposition of GaAs on Si for solar cell applications. *Journal of Crystal Growth*, 77(1-3):530 – 538, 1986.

[9] S. M. Vernon, S. P. Tobin, V. E. Haven, C. Bajgar, T. M. Dixon, M. M. Al-Jassim, R. K. Ahrenkiel, and K. A. Emery. Efficiency improvements in GaAs-on-Si solar cells. In *Photovoltaic Specialists Conference, 1988., Conference Record of the Twentieth IEEE*, pages 481–485 vol.1, Sept 1988.

[10] Yukiko Shimizu and Yoshitaka Okada. Growth of high-quality GaAs/Si films for use in solar cell applications. *Journal of Crystal Growth*, 265(1-2):99 – 106, 2004.

[11] N. A. El-Masry, J. C. Tarn, and N. H. Karam. Interactions of dislocations in GaAs grown on Si substrates with InGaAs-GaAsP strained layered superlattices. *Journal of Applied Physics*, 64(7), 1988.

[12] T. J. Grassman, J. A. Carlin, B. Galiana, F. Yang, M. J. Mills, and S. A. Ringel. MOCVD-grown GaP/Si subcells for integrated III-V/Si multijunction photovoltaics. *IEEE Journal of Photovoltaics*, 4(3):972–980, May 2014.

[13] T. J. Grassman, D. J. Chmielewski, S. D. Carnevale, J. A. Carlin, and S. A. Ringel. $GaAs_{0.75}P_{0.25}$/Si dual-junction solar cells grown by MBE and MOCVD. *IEEE Journal of Photovoltaics*, (99):1–6, 2015.

[14] C. L. Andre, John A. Carlin, John J. Boeckl, D. M. Wilt, M. A. Smith, A. J. Pitera, M. L. Lee, E. A. Fitzgerald, and S. A. Ringel. Investigations of high-performance GaAs solar cells grown on Ge-SiGe-Si substrates. *IEEE Transactions on Electron Devices*, 52(6):1055–1060, June 2005.

[15] C. L. Andre, D. M. Wilt, A. J. Pitera, M. L. Lee, E. A. Fitzgerald, and S. A. Ringel. Impact of dislocation densities on $n^+p$ and $p^+n$ junction GaAs diodes and solar cells on SiGe virtual substrates. *Journal of Applied Physics*, 98(1), 2005.

[16] J. A. Carlin, S. A. Ringel, E. A. Fitzgerald, M. Bulsara, and B. M. Keyes. Impact of GaAs buffer thickness on electronic quality of GaAs grown on graded Ge/GeSi/Si substrates. *Applied Physics Letters*, 76(14), 2000.

[17] M. Diaz, Li Wang, A. Gerger, A. Lochtefeld, C. Ebert, R. Opila, I. Perez-Wurfl, and A. Barnett. Dual-junction GaAsP/SiGe on silicon tandem solar cells. In *Photovoltaic Specialist Conference (PVSC), 2014 IEEE 40th*, pages 0827–0830, June 2014.

[18] T. J. Grassman, M. R. Brenner, S. Rajagopalan, R. Unocic, R. Dehoff, M. Mills, H. Fraser, and S. A. Ringel. Control and elimination of nucleation-related defects in GaP/Si (001) heteroepitaxy. *Applied Physics Letters*, 94(23), 2009.

[19] T. J. Grassman, J. A. Carlin, B. Galiana, L. M. Yang, F. Yang, M. J. Mills, and S. A. Ringel. Nucleation-related defect-free GaP/Si (100) heteroepitaxy via metal-organic chemical vapor deposition. *Applied Physics Letters*, 102(14), 2013.

[20] Xuesong Lu, Ruiying Hao, M. Diaz, R. L. Opila, and A. Barnett. Improving GaP solar cell performance by passivating the surface using $Al_xGa_{1-x}P$ epi-layer. *IEEE Journal of the Electron Devices Society*, 1(5):111–116, May 2013.

[21] Xuesong Lu, S. Huang, M.B. Diaz, N. Kotulak, Ruiying Hao, R. Opila, and A. Barnett. Wide band gap gallium phosphide solar cells. *IEEE Journal of Photovoltaics*, 2(2):214–220, April 2012.

[22] C. R. Allen, J. M. Woodall, and J. H. Jeon. Results of a gallium phosphide photovoltaic junction with an AR coating under concentration of natural sunlight. *Solar Energy Materials and Solar Cells*, 95(9):2655 – 2658, 2011.

[23] W. Shan, W. Walukiewicz, K. M. Yu, J. Wu, J. W. Ager, E. E. Haller, H. P. Xin, and C. W. Tu. Nature of the fundamental band gap in GaNP alloys. *Applied Physics Letters*, 76(22), 2000.

[24] P. R. C. Kent and Alex Zunger. Theory of electronic structure evolution in GaAsN and GaPN alloys. *Phys. Rev. B*, 64:115208, Aug 2001.

[25] J. Wu, W. Shan, and W. Walukiewicz. Band anticrossing in highly mismatched III-V semiconductor alloys. *Semiconductor Science and Technology*, 17:860–869, 2002.

[26] H. P. Xin, C. W. Tu, Yong Zhang, and A. Mascarenhas. Effects of nitrogen on the band structure of GaNP alloys. *Applied Physics Letters*, 76(10), 2000.

[27] I. A. Buyanova, G. Pozina, J. P. Bergman, W. M. Chen, H. P. Xin, and C. W. Tu. Time-resolved studies of photoluminescence in GaNP alloys: Evidence for indirect-direct band gap crossover. *Applied Physics Letters*, 81(1), 2002.

[28] G. Yu. Rudko, I. A. Buyanova, W. M. Chen, H. P. Xin, and C. W. Tu. Temperature behavior of the GaNP band gap energy. *Solid-State Electronics*, 47(3):493 – 496, 2003.

[29] V. K. Subashiev and G. A. Chalikyan. The absorption spectrum of gallium phosphide between 2 and 3 eV. *Physica Status Solidi (b)*, 13(2):K91–K96, 1966.

[30] Roy F. Potter. Chapter 2 - Basic parameters for measuring optical properties. In Edward D. Palik, editor, *Handbook of Optical Constants of Solids*, pages 11 – 34. Academic Press, Burlington, 1997.

[31] O. Breitenstein, J. P. Rakotoniaina, M. H. Al Rifai, and M. Werner. Shunt types in crystalline silicon solar cells. *Progress in Photovoltaics: Research and Applications*, 12(7):529–538, 2004.

[32] Martin A. Green. Solar cell fill factors: General graph and empirical expressions. *Solid-State Electronics*, 24(8):788 – 789, 1981.

[33] Martin A. Green. Accuracy of analytical expressions for solar cell fill factors. *Solar Cells*, 7(3):337 – 340, 1982.

[34] R. R. King, D. Bhusari, A. Boca, D. Larrabee, X.-Q. Liu, W. Hong, C. M. Fetzer, D. C. Law, and N. H. Karam. Band gap-voltage offset and energy production in next-generation multijunction solar cells. *Progress in Photovoltaics: Research and Applications*, 19(7):797–812, 2011.

[35] Jenny Nelson. *The physics of solar cells*. Imperial College Press, 2013.

[36] Band structure and carrier concentration of GaP. *http://www.ioffe.ru/SVA/NSM/Semicond/GaP/bandstr.html*, (accessed November, 2015).

[37] M. L. Young and D. R. Wight. Concentration dependence of the minority carrier diffusion length and lifetime in GaP. *Journal of Physics D: Applied Physics*, 7(13):1824, 1974.

[38] M. Gershenzon and R. M. Mikulyak. Radiative pair recombination and surface recombination in GaP photoluminescence. *Applied Physics Letters*, 8(10), 1966.

[39] M. A. Herman and H. Sitter. *Molecular beam epitaxy*. Springer-Verlag, 1989.

[40] M. B. Panish and H. Temkin. *Gas source molecular beam epitaxy*. Springer-Verlag, 1993.

[41] M. Izadifard, I. A. Buyanova, J. P. Bergman, W. M. Chen, A. Utsumi, Y. Furukawa, A. Wakahara, and H. Yonezu. Effects of rapid thermal annealing on optical quality of GaNP alloys. *IEEE Proceedings Optoelectronics*, 151(5):335–337, Oct 2004.

[42] D. Dagnelund, I. A. Buyanova, X. J. Wang, W. M. Chen, A. Utsumi, Y. Furukawa, A. Wakahara, and H. Yonezu. Formation of grown-in defects in molecular beam epitaxial Ga(In)NP: Effects of growth conditions and postgrowth treatments. *Journal of Applied Physics*, 103(6), 2008.

[43] Yan-Jin Kuang, San-Wen Chen, Hua Li, Sunil K. Sinha, and Charles Wuching Tu. Growth of GaNAsP alloys on GaP(100) by gas-source molecular beam epitaxy. *Journal of Vacuum Science & Technology B*, 30(2), 2012.

[44] M. Da Silva, S. Almosni, C. Cornet, A. Ltoublon, C. Levallois, P. Rale, L. Lombez, J. F. Guillemoles, and O. Durand. GaAsPN-based pin solar cells MBE-grown on GaP substrates: toward the III-V/Si tandem solar cell, 2015.

[45] S. L. Tan, C. J. Hunter, S. Zhang, L. J. J. Tan, Y. L. Goh, J. S. Ng, I. P. Marko, S. J. Sweeney, A. R. Adams, J. Allam, and J. P. R. David. Improved optoelectronic properties of rapid thermally annealed dilute nitride GaInNAs photodetectors. *Journal of Electronic Materials*, 41(12):3393–3401, 2012.

[46] S. Kurtz, A. Ptak, S. Johnston, C. Kramer, M. Young, D. Friedman, J. Geisz, W. McMahon, A. Kibbler, J. Olson, and et al. Understanding the potential and limitations of dilute nitride alloys for solar cells. *http://www.osti.gov/scitech/servlets/purl/882820*, Nov 2005.

[47] Bruce A. Joyce. Materials fundamentals of molecular beam epitaxy. *Advanced Materials*, 5(10):773–773, 1993.

[48] S. Tomasulo, K. Nay Yaung, J. Faucher, M. Vaisman, and M. L. Lee. Metamorphic 2.1-2.2 eV InGaP solar cells on GaP substrates. *Applied Physics Letters*, 104(17), 2014.

[49] S. Tomasulo, K. Nay Yaung, J. Simon, and M. L. Lee. GaAsP solar cells on GaP substrates by molecular beam epitaxy. *Applied Physics Letters*, 101(3), 2012.

[50] Jinkyoung Yoo, Binh-Minh Nguyen, Ian H. Campbell, Shadi A. Dayeh, Paul Schuele, David Evans, and S. Tom Picraux. Si radial p-i-n junction photovoltaic arrays with built-in light concentrators. *ACS Nano*, 9(5):5154–5163, 2015.

[51] Giacomo Mariani, Zhengliu Zhou, Adam Scofield, and Diana L. Huffaker. Direct-bandgap epitaxial core-multishell nanopillar photovoltaics featuring subwavelength optical concentrators. *Nano Letters*, 13(4):1632–1637, 2013.

[52] Brendan M. Kayes, Harry A. Atwater, and Nathan S. Lewis. Comparison of the device physics principles of planar and radial p-n junction nanorod solar cells. *Journal of Applied Physics*, 97(11), 2005.

[53] Kwang-Tae Park, Zhongyi Guo, Han-Don Um, Jin-Young Jung, Jun Mo Yang, Sung Kyu Lim, Young Su Kim, and Jung-Ho Lee. Optical properties of Si microwires combined with nanoneedles for flexible thin film photovoltaics. *Opt. Express*, 19(S1):A41–A50, Jan 2011.

[54] Ning Han, Zai xing Yang, Fengyun Wang, Guofa Dong, SenPo Yip, Xiaoguang Liang, Tak Fu Hung, Yunfa Chen, and Johnny C. Ho. High-performance GaAs nanowire solar cells for flexible and transparent photovoltaics. *ACS Applied Materials & Interfaces*, 7(36):20454–20459, 2015.

[55] Han-Don Um, Inchan Hwang, Namwoo Kim, Young J. Yu, Munib Wober, Ka-Hyun Kim, and Kwanyong Seo. Microgrid electrode for Si microwire solar cells with a fill factor of over 80%. *Advanced Materials Interfaces*, 2(16), 2015.

[56] Jain Nikhil and Mantu K. Hudait. III-V multijunction solar cell integration with silicon: Present status, challenges and future outlook. energy harvesting and systems. *Energy Harvesting and Systems*, 1(3-4):121–145, 2015.

[57] James P. Connolly, Denis Mencaraglia, Charles Renard, and Daniel Bouchier. Designing III-V multijunction solar cells on silicon. *Progress in Photovoltaics: Research and Applications*, 22(7):810–820, 2014.

[58] Adele C. Tamboli, Manav Malhotra, Gregory M. Kimball, Daniel B. Turner-Evans, and Harry A. Atwater. Conformal GaP layers on Si wire arrays for solar energy applications. *Applied Physics Letters*, 97(22), 2010.

[59] Daniel B. Turner-Evans, Christopher T. Chen, Hal Emmer, William E. McMahon, and Harry A. Atwater. Optoelectronic analysis of multijunction wire array solar cells. *Journal of Applied Physics*, 114(1), 2013.

[60] Nicholas C. Strandwitz, Daniel B. Turner-Evans, Adele C. Tamboli, Christopher T. Chen, Harry A. Atwater, and Nathan S. Lewis. Photoelectrochemical behavior of planar and microwire-array Si/GaP electrodes. *Advanced Energy Materials*, 2(9):1109–1116, 2012.

[61] C. T. Chen, D. B. Turner-Evans, H. Emmer, S. Aloni, and H. A. Atwater. Design and growth of III-V on Si microwire array tandem solar cells. In *Photovoltaic Specialists Conference (PVSC), 2013 IEEE 39th*, pages 3397–3401, June 2013.

[62] P. Caroff, K. A. Dick, J. Johansson, M. E. Messing, K. Deppert, and L. Samuelson. Controlled polytypic and twin-plane superlattices in III-V nanowires. *Nat Nano*, 4(1):50–55, January 2009.

[63] Tim Burgess, Steffen Breuer, Philippe Caroff, Jennifer Wong-Leung, Qiang Gao, Hark Hoe Tan, and Chennupati Jagadish. Twinning superlattice formation in GaAs nanowires. *ACS Nano*, 7(9):8105–8114, 2013.

[64] Rienk E. Algra, Marcel A. Verheijen, Magnus T. Borgstrom, Lou-Fe Feiner, George Immink, Willem J. P. van Enckevort, Elias Vlieg, and Erik P. A. M. Bakkers. Twinning superlattices in indium phosphide nanowires. *Nature*, 456(7220):369–372, November 2008.

[65] Anjia Gu, Yijie Huo, Shu Hu, T. Sarmiento, E. Pickett, Dong Liang, Shuang Li, A. Lin, S. Thombare, Zongfu Yu, Shanhui Fan, P. McIntyre, Yi Cui, and J. Harris. Design and growth of III-V nanowire solar cell arrays on low cost substrates. In *Photovoltaic Specialists Conference (PVSC), 2010 35th IEEE*, pages 002034–002037, June 2010.

[66] S. H. Yang and P. R. Bandaru. An experimental study of the reactive ion etching (RIE) of GaP using $BCl_3$ plasma processing. *Materials Science and Engineering: B*, 143(1-3):27 – 30, 2007.

[67] A. E. Dulkin, V. Z. Pyataev, N. O. Sokolova, S. A. Moshkalyov, A. S. Smirnov, and K. S. Frolov. The study of GaAs reactive ion etching in $Cl_2$/Ar. *Vacuum*, 44(9):913 – 917, 1993. Special Issue Proceedings of the 10th All-Union Conference on the Interaction of Ions with Surfaces.

[68] Albert G. Baca and Carol I. H. Ashby. *Fabrication of GaAs Devices*. Institution of Engineering and Technology, 2005.

[69] Gerhard Franz, Wolfgang Hsler, and Rolf Treichler. Sidewall passivation of GaAs in $BCl_3$-containing atmospheres. *Journal of Vacuum Science & Technology B*, 19(2), 2001.

[70] A. R. Clawson. Guide to references on III-V semiconductor chemical etching. *Materials Science and Engineering: R: Reports*, 31(1-6):1 – 438, 2001.

[71] Maoqing Yao, Sen Cong, Shermin Arab, Ningfeng Huang, Michelle L. Povinelli, Stephen B. Cronin, P. Daniel Dapkus, and Chongwu Zhou. Tandem solar cells using GaAs nanowires on Si: Design, fabrication, and observation of voltage addition. *Nano Letters*, 15(11):7217, 2015.

[72] Andreas Brenneis, Jan Overbeck, Julian Treu, Simon Hertenberger, Stefanie Morktter, Markus Dblinger, Jonathan J. Finley, Gerhard Abstreiter, Gregor Koblmller, and Alexander W. Holleitner. Photocurrents in a single InAs nanowire/silicon heterojunction. *ACS Nano*, 9(10):9849–9858, 2015.

[73] Mattias Borg, Heinz Schmid, Kirsten E. Moselund, Giorgio Signorello, Lynne Gignac, John Bruley, Chris Breslin, Pratyush Das Kanungo, Peter Werner, and Heike Riel. Vertical III-V nanowire device integration on Si(100). *Nano Letters*, 14(4):1914–1920, 2014.

[74] Jesper Wallentin, Nicklas Anttu, Damir Asoli, Maria Huffman, Ingvar berg, Martin H. Magnusson, Gerald Siefer, Peter Fuss-Kailuweit, Frank Dimroth, Bernd Witzigmann, H. Q. Xu, Lars Samuelson, Knut Deppert, and Magnus T. Borgstrm. InP nanowire array solar cells achieving 13.8% efficiency by exceeding the ray optics limit. *Science*, 339(6123):1057–1060, 2013.

[75] Chenxi Lin and Michelle L. Povinelli. Optical absorption enhancement in silicon nanowire arrays with a large lattice constant for photovoltaic applications. *Opt. Express*, 17(22):19371–19381, Oct 2009.

[76] Jia Zhu, Zongfu Yu, George F. Burkhard, Ching-Mei Hsu, Stephen T. Connor, Yueqin Xu, Qi Wang, Michael McGehee, Shanhui Fan, and Yi Cui. Optical absorption enhancement in amorphous silicon nanowire and nanocone arrays. *Nano Letters*, 9(1):279–282, 2009.

[77] Yue Liang, William D. Nix, Peter B. Griffin, and James D. Plummer. Critical thickness enhancement of epitaxial SiGe films grown on small structures. *Journal of Applied Physics*, 97(4):043519, 2005.

[78] Shadi A. Dayeh, Wei Tang, Francesca Boioli, Karen L. Kavanagh, He Zheng, Jian Wang, Nathan H. Mack, Greg Swadener, Jian Yu Huang, Leo Miglio, King-Ning Tu, and S. Tom Picraux. Direct measurement of coherency limits for strain relaxation in heteroepitaxial core/shell nanowires. *Nano Letters*, 13(5):1869–1876, 2013.

[79] Ke Sun, A. Kargar, Namsoek Park, K. N. Madsen, P. W. Naughton, T. Bright, Yi Jing, and Deli Wang. Compound semiconductor nanowire solar cells. *IEEE Journal of Selected Topics in Quantum Electronics*, 17(4):1033–1049, July 2011.

[80] Joshua M. Spurgeon, Shannon W. Boettcher, Michael D. Kelzenberg, Bruce S. Brunschwig, Harry A. Atwater, and Nathan S. Lewis. Flexible, polymer-supported, Si wire array photoelectrodes. *Advanced Materials*, 22(30):3277–3281, 2010.

[81] W. G. Bi and C. W. Tu. N incorporation in GaP and band gap bowing of GaNP. *Applied Physics Letters*, 69(24), 1996.

[82] R. S. Wagner and W. C. Ellis. Vapor-liquid-solid mechanism of single crystal growth. *Applied Physics Letters*, 4(5), 1964.

[83] Jiangtao Hu, Teri Wang Odom, , and Charles M. Lieber. Chemistry and physics in one dimension: synthesis and properties of nanowires and nanotubes. *Accounts of Chemical Research*, 32(5):435–445, 1999.

[84] Katsuhiro Tomioka, Junichi Motohisa, Shinjiroh Hara, and Takashi Fukui. Control of InAs nanowire growth directions on Si. *Nano Letters*, 8(10):3475–3480, 2008.

[85] V. G. Dubrovskii, G. E. Cirlin, I. P. Soshnikov, A. A. Tonkikh, N. V. Sibirev, Yu. B. Samsonenko, and V. M. Ustinov. Diffusion-induced growth of GaAs nanowhiskers during molecular beam epitaxy: Theory and experiment. *Phys. Rev. B*, 71:205325, May 2005.

[86] Shadi A. Dayeh and S. T. Picraux. Direct observation of nanoscale size effects in Ge semiconductor nanowire growth. *Nano Letters*, 10(10):4032–4039, 2010.

[87] Philippe Caroff, Jessica Bolinsson, and J. Johansson. Crystal phases in III-V nanowires: From random toward engineered polytypism. *IEEE Journal of Selected Topics in Quantum Electronics*, 17(4):829–846, July 2011.

[88] Y. J. Kuang, S. Sukrittanon, H. Li, and C. W. Tu. Growth and photoluminescence of self-catalyzed GaP/GaNP core/shell nanowires on Si (111) by gas source molecular beam epitaxy. *Applied Physics Letters*, 100(5):053108, 2012.

[89] M. Vaisman, S. Tomasulo, T. Masuda, J. R. Lang, J. Faucher, and M. L. Lee. Effects of growth temperature and device structure on gap solar cells grown by molecular beam epitaxy. *Applied Physics Letters*, 106(6), 2015.

[90] Hong-Mei Wang, Jian-Ping Zhang, Chang-Qing Chen, Q. Fareed, Jin-Wei Yang, and M. Asif Khan. AlN/AlGaN superlattices as dislocation filter for low-threading-dislocation thick AlGaN layers on sapphire. *Applied Physics Letters*, 81(4), 2002.

[91] S. Sharan, J. Narayan, and J.C.C. Fan. Dislocation density reduction in GaAs epilayers on Si using strained layer superlattices. *Journal of Electronic Materials*, 20(7):779–784, 1991.

[92] Zhenwu Shi, Lu Wang, Yanxiang Cui, Honggang Liu, Haitao Tian, Wenxin Wang, and Hong Chen. Suppressing the spread length of threading dislocations in AlSb/GaSb superlattice grown on (001) InP substrate. *Applied Physics A*, 115(4):1239–1243, 2014.